Molecular-Based Optical Diagnostics for Hypersonic Nonequilibrium Flows

Paul M. Danehy* and Brett F. Bathel*
NASA Langley Research Center, Hampton, Virginia, 23681-2199, USA

Craig T. Johansen†
University of Calgary, Calgary, AB, T2N 1N4, Canada

Michael Winter‡
University of Kentucky, Lexington, KY 40506-0503, USA

Sean O'Byrne§
University of New South Wales Canberra, Canberra, ACT 2600 Australia

Andrew D. Cutler**
The George Washington University, Newport News, VA 23602, USA

1. Introduction

Departure from thermal and chemical equilibrium occurs frequently in hypersonic flow. When a fluid element travels through a flowfield it will stay in equilibrium with its surroundings if the molecular collision rate is sufficiently high. On the other hand, if the fluid element experiences sudden changes in conditions and the collision rate is relatively low, then departure from thermodynamic equilibrium, or *nonequilibrium*, occurs. In hypersonic flight nonequilibrium can occur, for example, as gas passes through shock waves, suddenly expands, or undergoes combustion. The resulting nonequilibrium can affect the population of molecules in translational, rotational, and vibrational internal energy modes as well as the chemical composition. Such nonequilibrium phenomena, if ignored, can lead to erroneous predictions of lift, drag, aeroheating, and engine performance.

In a gas in thermal equilibrium the distribution of population among its various thermal energy levels (translational, rotational, and vibrational) is governed by the Boltzmann distribution law, which is expressed in terms of a temperature. If the gas is not in thermal equilibrium, then no unique temperature can be assigned. In moderate density (non-rarified) hypersonic flows it is often useful to define separate vibrational and translational-rotational temperatures (where translation and rotational modes are assumed to be in equilibrium among themselves and with each other). For example, the translational-rotational temperature will rise abruptly across a shock wave, but the distribution of energy in the vibrational levels will take some time (distance) before it comes into equilibrium. It has been shown that under certain

* Research Scientist, Advanced Sensing and Optical Measurement Branch, MS 493.
† Assistant Professor, Mechanical and Manufacturing Engineering.
‡ Assistant Professor, Mechanical Engineering Department
§ Senior Lecturer in the UNSW Canberra School of Engineering and Information Technology
** Professor, Mechanical and Aerospace Engineering Department, 1 Old Oyster Point Road, Suite 200.

conditions an intermediate vibrational temperature may be defined (i.e., a Boltzmann distribution of population among the vibrational levels) at various times in the relaxation.[1] In rarefied hypersonic flows, the rotational and translation temperatures can be unequal; furthermore they can have non-Boltzmann distributions.[2]

Computation of fluid dynamical flowfields is greatly complicated when nonequilibrium must be considered. Instead of computing chemical equilibrium, finite rate chemistry must be included, resulting in the calculation of tens to thousands of equations instead of just a few. Similarly, thermal nonequilibrium conditions require bookkeeping of different temperatures for different energy modes such as translational, rotational and vibrational temperatures, T_{trans}, T_{rot} and T_{vib}, respectively, assuming that each of those energy modes can be described by a Boltzmann distribution. Further complicating matters, different species in the same flow can have different vibrational temperatures, or may even have nonequilibrium distributions that cannot be described by a temperature. For example, the products of some exothermic chemical reactions are formed with a non-Boltzmann distribution of vibrational energy.[1]

While thermodynamic and chemical nonequilibrium occur in many different fields of chemistry, physics and engineering, hypersonic flows are particularly susceptible to these complicating effects. Hypersonic vehicles (for example, entry vehicles or hypersonic cruise vehicles) typically fly at high altitude where the pressure is low. Because of the high speed, kinetic energy from the vehicle is converted to thermal energy in the gas flowing over the vehicle. Thus hypersonic gas flow typically encounters low pressure, P, and high temperature, T, conditions. Since gaseous collision rates scale as $P/\sqrt{T}$, low-pressure high-temperature flows can have relatively low collision rates. These low collision rates, coupled with flow phenomena like shock waves, expansions and boundary layers which have steep gradients, cause sudden changes in flow conditions, resulting in nonequilibrium.

The different thermal and chemical phenomena mentioned above require different numbers of collisions to maintain equilibrium. Translational and rotational modes of a molecule can be brought into equilibrium with 10 or fewer collisions, occurring in less than 1 ns at P = 1 atm and T = 273 K.[3] For comparison, it takes about 20,000 collisions to vibrationally excite an O_2 molecule.[4] Chemical changes can occur even more slowly. Dissociation of the O_2 molecule by collisions requires on the order of 200,000 collisions.4 Thus vibrational and chemical changes in a gas occur much more slowly than translational and rotational changes. Consequently, vibrational and chemical nonequilibrium are more commonly observed in hypersonic flow than translational and rotational nonequilibrium, and measurements of these phenomena will be emphasized in this chapter. The complexity of modeling these nonequilibrium phenomena, and the strong effect that they can have on the heating of aerospace vehicles, makes it essential to develop experimental techniques capable of quantifying the degree of nonequilibrium in the flowfield without interfering with the distributions that they are measuring. The non-intrusive and quantum-state-specific characteristics of spectroscopic techniques make them uniquely suitable for this purpose. Spectroscopy, then, can provide direct experimental evidence of these

equilibrium or nonequilibrium thermal distributions and chemical compositions. Nonintrusive spectroscopic techniques can be used in ground-based flow simulation facilities and sometimes even in flight to probe individual atomic and molecular states, thereby measuring population distributions, translational, rotational and vibrational temperatures, chemical compositions, and other data that can help modelers compute these challenging flowfields.

A variety of different molecular-based optical measurement techniques will be detailed in this chapter. Optical emission spectroscopy (OES) is the only technique detailed herein that does not require a light source (e.g. a laser). OES instead disperses naturally emitted light to provide quantitative flow field information. However OES can only be used to study luminous environments. Also it is difficult to determine spatially-specific information using OES since the collection optics average all the light along its optical path. These limitations can be overcome by using a light source such as a lamp or a laser. If a light source is incident upon a gaseous medium the incident photons can either be absorbed, scattered, or can transmit through the medium. These different possible light paths present opportunities for different methods to probe and measure the gas. Absorption spectroscopy uses the transmitted light to diagnose the sample: the method compares the transmitted intensity with a sample present to a reference thereby determining the sample's absorption integrated along the optical path. Rayleigh scattering, Raman scattering and laser induced fluorescence (LIF) collect scattered light at an angle to the incoming light. This localizes the measurement point at the intersection between the incoming light and the optical path of the detection optics. Measurements can be made at a single spatial location or, using a camera, measurements can be made along a line or in an image plane. Whereas Rayleigh scattering is an elastic scattering process, Raman scattering is inelastic, with a small amount of energy either gained from or lost to the surrounding medium. LIF is a two-step process wherein a photon from the incident beam is absorbed and then is subsequently emitted. These scattering processes emit light approximately isotropically in three dimensions (into 4π steradians) so that the intensity of the light drops off as one over the distance from the measurement point squared (*inverse square law*). Consequently, using conventional lenses, only a small fraction (typically ~1%) of the scattered light can be collected.[5] The abovementioned scattering techniques do not require the coherence property of a laser and are known as *incoherent* measurement techniques.

Coherent measurement approaches involve the use of multiple laser beams which are directed into and interact with the flowfield. These techniques make use of the coherence of laser light to perform nonlinear wave-mixing which generates coherent signal beams. The resulting laser-like beam does not follow the inverse square law. Instead, it can propagate long distances without loss. It can also be spatially filtered to reject flow luminosity (which does follow the inverse square law) without losing signal intensity. For coherent measurement techniques, the measurement volume is determined by the location of the crossing of the laser beams. Unfortunately, these coherent techniques are much more complicated to set up and harder to keep aligned than incoherent techniques. Also, these methods are nonlinear and are

therefore generally more difficult to analyze and interpret than incoherent techniques. However, coherent techniques, such as coherent anti-Stokes Raman spectroscopy (CARS), provide high signal-to-noise ratio data in applications with limited optical access and/or flow luminosity.

This chapter mainly focuses on spectroscopic measurement techniques for studying gaseous hypersonic nonequilibrium flow. In particular, we will focus on techniques that have either been used to study hypersonic nonequilibrium flowfields or techniques that show promise for studying these flows. Several classes of measurement techniques that are, or could be, used to study hypersonic nonequilibrium flows are *not* described herein. For example, surface measurement techniques such as pressure and temperature sensitive paint, phosphor thermography, skin friction measurements and photogrammetry (for model attitude and deformation measurement) are excluded to limit the scope of the chapter. Physical probes such as pitot probes, static pressure probes, heat flux gauges, total temperature probes, and others are excluded to limit scope. We further exclude measurement techniques that require particle seeding because of practical difficulties in seeding particles into hypersonic nonequilibrium flow facilities and because the particles may not faithfully follow the flow through steep gradients[6] often associated with hypersonic nonequilibrium flow. However, particle based methods may still be useful in certain hypersonic nonequilibrium flow applications. The chapter emphasizes quantitative techniques, so excluded are techniques that typically provide only flow visualization, such as schlieren.

Hypersonic facilities present many challenges to the implementation of optical measurement techniques. Facilities capable of producing high-enthalpy flow often have hazards that must be accommodated in order to make measurements. Such hazards include those associated with high pressure, explosives, high voltage, high acoustic noise and toxic gas generated by the facility and the measurement system. Consequently, in many facilities the operator cannot be near the facility during operation so the equipment must be operated remotely or must operate autonomously. To reduce costs and increase test section size and operating pressure range many hypersonic facilities operate for very short duration, for example 100 msec or less. These are known as *impulse* facilities. For laser systems operating at 10 Hz only one measurement can be acquired in these facilities per tunnel run. Since some impulse facilities can operate only once per day it is difficult to obtain a statistically significant number of measurements with some measurement techniques. In such facilities higher-speed measurement systems that can obtain data at kHz or MHz rates are desirable. Large impulse facilities can move a few centimeters during operation, complicating measurement technique alignment. The flow through longer-run-duration facilities induces vibrations that can misalign optical measurement systems and changes in the model position may occur via thermal expansion of the support system. Furthermore, many large hypersonic facilities have poor or no optical access; if there is optical access the window material may not be suitable for the desired measurement technique. Hypersonic facilities are often located in dirty operating environments and for practical considerations the lasers often are placed far from the test section requiring long path lengths resulting in

misalignment and reduced laser energy delivered to the test section. Finally, some hypersonic facilities produce very luminous flow, making difficult the detection of weak light signals. In such flowfields, coherent optical measurement techniques are desirable.

In some instances, it is desired to study nonequilibrium effects. However, nonequilibrium also frequently occurs as a byproduct of heating and accelerating the test gas in hypersonic facilities. For example, in order to achieve the required high flow enthalpy and Mach number, gas is often heated to thousands of Kelvin and then expanded through a nozzle. Energy can be added to the flow using electricity (via convection over a heating element or by an electric arc), by driving shockwaves through the gas, or by combustion.[7,8] Upstream of the nozzle, the gas can be vibrationally excited and may reach chemical equilibrium in which minor species such as NO, O, and N are present for the case of air. When the gas expands through the nozzle, the collision rate is not sufficient to keep the chemical composition in equilibrium and the chemical composition effectively freezes at an intermediate composition. Similarly, vibrational energy modes do not stay in equilibrium with rotational and translational modes, which can result in $T_{vib} > T_{rot} \approx T_{trans}$. This test gas in a state of chemical and/or thermal nonequilibrium, expanded to the desired Mach number, then passes over the test article being studied. An accurate understanding of the nozzle exit, or *freestream* conditions, is required to properly characterize the test stream, calibrate the facility, interpret the test results and to scale the test results to flight. For a detailed description of the different types of hypersonic test facilities see the chapter titled "*High Enthalpy Facilities and Plasma Wind Tunnels for Aerothermodynamics Ground Testing*" in this manuscript.

The next section of this chapter reviews some of the equipment commonly used to perform the different measurement techniques. The following sections introduce and develop the theory behind some of the most important measurement techniques used to study hypersonic nonequilibrium flows. Theoretical developments are limited to introductory material with references provided for more detailed analysis. Then, selected measurement examples are described. These examples do not provide an exhaustive review but are meant to illustrate typical applications. When possible, applications to hypersonic nonequilibrium flows are shown. However, examples of other flowfields are provided if the measurements demonstrate the potential for application to hypersonic nonequilibrium flows.

2. Equipment Used for Molecular-Based Optical Measurement

There are similarities in the hardware used in most optical spectroscopic measurement systems. Some of the more common lasers and detection systems will be summarized here. References for commercially available equipment described are not cited to avoid preferential treatment to certain vendors. It is difficult to capture all possible types of lasers and optical detection systems in a few paragraphs. This section is intended to provide an introduction and overview to the uninitiated and is not a comprehensive discussion. The various specifications described are approximate and are presented only to provide rough orders of magnitude.

Laser systems can be classified as continuous wave or pulsed, though hybrid systems also exist. Continuous wave (*CW*) lasers operate continuously and are specified by their operating power in Watts. CW lasers can be made to operate with very narrow spectral resolution suitable for high-resolution spectroscopy where the spectral width of the laser is negligible compared to the spectrum being measured. Inexpensive, low powered diode lasers having power on the order of 1 mW are used for absorption measurements. Higher powered CW lasers on the order of 10 W are used for Rayleigh scattering measurements. These higher powered CW lasers are generally not broadly tunable, so for resonant techniques like laser induced fluorescence only coincidental spectral overlaps between available laser frequencies and atomic or molecular transitions can be exploited. To perform spectroscopic measurements at arbitrary wavelengths, high-powered CW lasers can be converted to tunable light using dye lasers and/or other energy conversion systems such as doubling or mixing crystals, sometimes in combination with other CW lasers. Currently, high-resolution (i.e. laser linewidth much narrower than the typical absorption linewidths) CW lasers are available commercially from the ultraviolet (UV) to the infrared (IR). The main limitations of CW lasers are their relatively low power output which may require long integration times to acquire data with sufficient signal-to-noise ratio in some applications. Whereas absorption spectroscopy, which detects the full laser beam, can be performed at hundreds of kHz, scattering approaches like the Rayleigh, Raman and LIF that use CW lasers typically acquire data several orders of magnitude slower because of low signal levels. For comparison, a typical hypersonic flow with a gas velocity of 2000 m/s, a 1 mm resolution would require 500 ns time resolution, corresponding to 2 MHz data acquisition rate.

Diode lasers provide CW light in most wavelength ranges of spectroscopic interest from the ultraviolet to the far infrared. Wavelengths can be varied over a limited range by modulating the temperature or injection current of the diode, at up to MHz scan rates,[9] providing extremely high time resolution for wavelength-scanning measurements. Because the lasers and detectors are small, have no moving parts, and the lasers are often coupled to optical fibers, these devices can be used to produce relatively robust measurement systems that are particularly well suited to the often harsh environments associated with nonequilibrium hypersonic flows. These characteristics have made diode laser absorption spectroscopy a particularly desirable technology for hypersonic flight testing programs.[10]

Pulsed lasers typically producing much higher power (on the order of 10^8 Watts) for short durations, typically over a few nanoseconds, have been commercially available for about three decades. Such powers are usually required to perform nonlinear spectroscopic measurement techniques like CARS. These lasers are usually specified in terms of the energy per pulse. For example, frequency doubled Nd:YAG laser systems can produce 1 J per pulse at 532 nm. Again, this type of laser is not broadly tunable but it can be used to pump a dye laser or optical parametric amplifier and together with other conversion devices (doubling and/or mixing crystals) can produce high-energy tunable output from the UV to the IR. Ten ns duration pulsed lasers allow measurements to be made with time resolution that “freezes” the flow (prevents

blurring). Raman, Rayleigh, PLIF and CARS systems based on Nd:YAG lasers typically integrate signals over 10 to 500 ns time durations. Unfortunately, commercially available high energy pulsed laser systems typically operate at repetition rates of 10 to 100 Hz, which according to the calculations above, are too slow to resolve unsteady flow fluctuations. Therefore, individual measurements can be considered instantaneous, but successive measurements are not correlated in time. The linewidth of pulsed lasers is typically broader than high resolution narrowband lasers because of a number of factors. A consequence of the Heisenberg uncertainty principle is that the shorter the duration of a laser pulse the spectrally more broad the laser pulse will be. Consequently, the spectrally narrowest 10 ns pulses typically have line widths equal to 0.004 cm^{-1}. These pulses are routinely obtained by injection seeding pulsed Nd:YAG lasers so that only a single longitudinal mode is amplified. These injection-seeded pulses are much broader than commercially available CW Nd:YAG lasers. Without seeding, the same Nd:YAG laser would have an even larger linewidth of about 1 cm^{-1}. Nd:YAG-pumped narrowband dye lasers typically have line widths within the range of 0.03 to 0.5 cm^{-1}, though modifications such as injection seeding or intercavity etalons can be used to reduce the linewidth of a pulsed dye laser. Conversely, spectrally selective elements can be removed to create a broadband (red) dye laser with a linewidth of 20 nm (~ 500 cm^{-1}) or more.[11]

There are several new laser technologies that have been developed in the past decade with high output power and fast repetition rates. This allows for flow freezing, temporally resolved measurements to be obtained with good signal-to-noise levels. *Pulse burst laser* technology uses Nd:YAG lasers that have been optimized to be pulsed 25-100's of times in succession at frequencies up to 1 MHz. Pulse burst laser technology is not yet widely commercially available although it is being brought to market. Another relatively new technology that produces high power and high repetition rates is known as *ultrafast* or *femtosecond* lasers. As the name implies, the duration of the laser pulses can be nearly a million times shorter than a typical nanosecond laser. While the energy per pulse (typically less than 10 mJ, for commercially available systems) is much lower than ns-based systems, the output power can be on the order of 10^{10} Watts, opening up new opportunities for coherent measurement approaches. Such high powers can be efficiently converted using optical parametric amplifiers and doubling or mixing crystals to extend the tuning range of femtosecond lasers to the UV and IR. Femtosecond lasers are commercially available at repetition rates up to 10 kHz - still two orders of magnitude too slow to time-resolve unsteady hypersonic flows. Even though the resulting measurements would not be time correlated, such high data rates are especially useful for acquiring statistics in short duration or expensive-to-operate test facilities. The higher data rate allowed by femtosecond lasers would be beneficial in most experiments. Picosecond-duration lasers are also available for spectroscopic measurement applications though picosecond lasers have neither the high energy per pulse of nanosecond lasers nor the high peak power of femtosecond lasers. The linewidth of a femtosecond laser is closely related to the duration of the pulse. Typical off-the-shelf femtosecond lasers with pulse duration on the order of 100 fs have linewidths of ~10 nanometers. While this relatively large linewidth prevents conventional high-resolution spectral-

domain spectroscopy, the time domain can instead be used to obtain detailed spectral information.

Most measurement techniques use some type of spectrally selective optic or optical system to collect or process signal. The simplest spectrally selective optic consists of filters that are placed in front of detectors or cameras. Absorptive and reflective filters are commercially available (or can be custom manufactured at a reasonable cost) at many wavelengths, for example to block the laser's wavelength and collect the signal in another wavelength. In some applications, the narrower the spectral filter the better, since the signal is often very close to the laser's wavelength such as in Rayleigh and rotational Raman scattering. Spectral filters blocking a 10-20 nm full width half maximum (FWHM) wide band near the laser's wavelength with greater than 6 orders of magnitude of attenuation while transmitting >95% of the Raman shifted signal can be purchased. However, such filters do not provide sufficient resolution to observe Doppler broadening and Doppler shifts required for gas temperature and velocity measurement from Rayleigh scattering, for example. Gaseous filters, such as I_2 vapor contained in a heated cell, can provide spectrally narrow (0.0015 nm or 0.05 cm^{-1} FWHM) and high (6 or more orders of magnitude) absorption which is useful in many applications.[12] Etalons are spectrally dispersive optics or optical systems that are made of a pair of partially reflective mirrors. An etalon's resolution depends on its flatness and reflectivity; the resolution can be high enough (0.01 cm^{-1}) to resolve the Doppler broadening (0.05 - 0.5 cm^{-1}) in typical hypersonic flow experiments and have an advantage over gas filters in that they can operate at any wavelength. Spectrometers, containing a dispersive optic such as a prism or grating, are typically used to disperse a signal beam into a spectrum that can be acquired by a detector or camera. Small (100 mm focal length), easy-to-use fiber-optic coupled spectrometers are commercially available for applications in which spectral resolution on the order of 0.02 nm (5 cm^{-1}) is acceptable. Larger spectrometers (for example with 1 meter or longer focal length) provide higher resolution spectra – the resolution generally increasing linearly with the focal length. Coupled with a CCD camera, such spectrometers can typically achieve resolutions of 0.15 cm^{-1}/pixel.[13] Resolution can sometimes be improved by using a camera with smaller pixels or by using a telescope at the exit of the spectrometer to enlarge the spectrum.[14]

For spectroscopic measurement techniques, light is detected with a variety of different single point, line, or imaging devices. Among single point detectors, photodiodes are typically used in applications where the intensity of the collected light is high, for example in absorption spectroscopy. Photodiodes are used because they are linear over a wide range of light intensities, have fast time response, require relatively simple electronics and are inexpensive to produce. Photomultiplier tubes (PMTs) are usually single-point detectors but they allow variable gain useful for amplifying light at low signal levels, while also providing fast (sub-ns) time response. While photodiodes and PMTs are both available as linear and even two-dimensional arrays, other camera technologies are usually used in spectroscopic applications where high resolution spatial or spectral information is required. Charge coupled device (CCD) cameras provide the linear

response (less than 1% nonlinearity), high dynamic range (12-16 bits) and high sensitivity required by many spectroscopic imaging or spectral applications. For applications requiring short exposures, for example to freeze the flow or to reject unwanted luminosity while capturing a transient signal, CCD cameras can be fitted with an image intensifier allowing exposure times down to hundreds of picoseconds. CCD cameras having 1 million pixels or more typically frame at tens of Hz consistent with high-powered YAG laser systems. CCD camera technology has been extended to much higher speeds (up to MHz rates) albeit with lower spatial resolution (for example 160x160 pixels). Recently, CMOS camera technology has allowed megapixel cameras to frame at tens of thousands of Hz allowing new opportunities for optical measurement techniques.

3. Optical Emission Spectroscopy

Optical emission spectroscopy (OES) is one of the oldest diagnostic techniques and has been applied to various fields of research. Traditionally, astronomy was one of the first fields to apply this passive method. Due to the large distances to even the nearest stars, emission spectroscopy continues to be one of the main techniques for understanding the stars. Despite its disadvantages, OES presents an often simple experimental method to access the thermochemical state of emitting gases. The experimental set-ups are relatively simple (not requiring a laser, for example) and the underlying optical principles well understood. However, the scope of this chapter does not allow for a complete description of emission spectroscopy methods applied to plasma diagnostics, even if restricted to nonequilibrium applications. Instead, selected examples of successful applications to nonequilibrium environments will be shown to demonstrate fundamental approaches to access these complicated problems.

In general, emission spectroscopy (if properly calibrated) can provide absolute, quantitative information on excited states (electronic, vibrational, or rotational). However, even in strongly radiating environments, the majority of particles will be in the ground state or in weakly excited levels. Therefore, an extrapolation of the measured quantities to the low lying states is necessary to obtain information about the gas chemistry. In *Thermodynamic Equilibrium*, the upper state population distributions are linked to the ground state through known relations, given by Boltzmann distributions. Even if temporal or spatial changes occur in a medium, an equilibrium assumption may be justified if the variations are slow enough that, for any point, one can assume thermodynamic equilibrium in some neighborhood about that point. This condition is widely called *Local Thermodynamic Equilibrium (LTE)*. When nonequilibrium processes are involved, these relations may no longer hold. Hence, a combination with other methods (LIF, CARS, absorption spectroscopy, etc.), which can access the ground and exited states not covered by emission spectroscopy, may better describe the thermodynamic state of the plasma. However, even without knowledge of the relation to the total particle density of the species under consideration or under nonequilibrium conditions, basic information may be extracted from spectral features. In particular, the line shape of individual lines carries important information on

translational temperature which often can be determined from Doppler broadening or the electron density can be inferred from the line's Stark broadening. Line *ratios* may be used to determine rotational, vibrational, or electronic excitation temperatures as opposed to the absolute intensity of the detected emission. Ratios between lines from inert elements (e.g. argon) and reacting components such as oxygen may carry information on chemical processes, even in nonequilibrium situations, without the need to compute total species densities.

One major difficulty of emission spectroscopy measurements is that each measurement provides integrated intensities along the entire line of sight. Furthermore, absorption along this line cannot be separated from single measurements. In case of an optically-thin medium, local distributions can be obtained through tomographic methods or through deconvolution of vertical profiles (e.g. through Abel-inversion or related methods if rotational symmetry of the emitting volume can be assumed). In the general case of an absorbing medium, only indirect methods made through a comparison with computed radiation based on numerical simulation are feasible.

Emission spectroscopy is typically performed in atmospheric entry wind tunnel tests for at least two different reasons: 1) to determine radiation as a load factor for design purposes (typical examples are given by recent testing in the NASA Ames EAST facility),[15] and 2) to use radiation as a tool for diagnostic purposes, e.g. for facility characterization[16] or to gather information for comparisons to numerical simulation (e.g. material response). One further important application of emission spectroscopy is flight measurements which can provide validation data for theoretical simulation and extrapolation to flight of ground test data, either by flight experiments[17, 18] or by airborne or ground based observation.[19, 20, 21] In industrial plasma applications (e.g. coating or edging), OES may be used for process control through empirical correlations or even to provide information on the underlying physics.

The more recent development of off-the-shelf miniaturized spectrometers and the availability of fiber-coupled instrumentation have simplified emission instruments. The hardware requirements can be roughly grouped into systems with 1) low resolution for survey and overview applications, 2) more sophisticated instruments (usually with larger focal length) for higher spectral resolutions of specific spectral features such as molecular band structures, and 3) high resolution systems (e.g. Fabry-Perot interferometers) for detailed investigation of single spectral lines in particular for the investigation of line shapes and broadening mechanisms.

The following sections will give a short introduction to basic physics for emission of radiation of atoms and molecules followed by examples for plasma diagnostics to determine temperatures, velocities or even particle densities. A description of some simulation codes with particular respect to hypersonic flows and examples for successful simulation of equilibrium plasmas with these codes will also be given. In a second part, the effect of nonequilibrium on plasma radiation will be discussed with examples showing emission spectroscopy applied under nonequilibrium conditions.

3.1 Basic Physics Describing the Emission of Atoms and Molecules

Unlike the emission of thermal radiation of solid bodies, which yields continuum radiation following Planck's formula, the emission of flames and plasmas usually consists of discrete emission lines. If measured in lower spectral resolution these lines appear as bands. These lines and bands originate from bound-bound transitions (i.e. in both upper and lower states of the transition, the participating electron is bound to an atom or molecule). These line spectra may overlap with continuum radiation produced through free-free or bound-free radiation generated through interaction of electrons with each other or heavy-particles (non-electrons) which, in the latter case, involves ionization and recombination processes. In general, the prediction of single emission lines can be divided into three problems:

a) determination of the spectral position of the line using empirical or quantum mechanical information on the governing energy difference,
b) determination of the line strength using thermodynamic information about the plasma state (i.e. the upper state population), and
c) determination of the spectral shape of the line determined by broadening processes, again from the thermodynamic state (e.g. the gas temperature for Doppler broadening and pressure/species information for pressure or/and Stark broadening).

For bound-bound emission processes, each emission line will be produced through a radiative transition from an upper energetic state E_2 to an energetically lower state E_1. The resulting photon will carry the energy difference $\Delta E=E_2-E_1$ which determines its frequency

$$\nu=\Delta E/h \tag{3.1}$$

with Planck's constant h. This frequency is equivalent to the speed of light divided by the wavelength of the emitted radiation, in a vacuum:

$$\nu=c_0/\lambda \tag{3.2}$$

Often, the energy is used and tabulated normalized by the product of $(h\,c_0)$, given in the unit [cm^{-1}]. Consequently, the spectral position of an emission line might be characterized by its wavenumber, $\bar{\nu}$, which is the inverse of its wavelength, again often given in [cm^{-1}].

The energy emitted by one emission line, often called the volumetric emission coefficient, can be written as the energy of one photon $(h\nu)$ times the number of atoms which undergo this transition per unit time, defined as a probability (Einstein coefficient of spontaneous emission, A_{21}) times the population density in the upper energy state, emitted into full space of 4π:

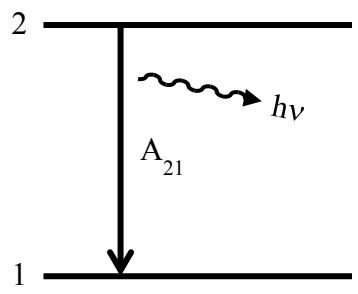

Figure 3.1. Energy level diagram for spontaneous emission.

$$\varepsilon_{21}=\frac{h\nu}{4\pi}A_{21}n_2 \tag{3.3}$$

We recognize that the emitted power depends on the product of the transition probability A_{21}, which only depends on the quantum mechanical characteristics of the energy level E_2, and the upper state particle density n_2 which depends on the thermodynamic state of the emitting medium. For a computation of the emitted power, we therefore have to determine the quantum mechanical relations for the species and the energy level of concern and the thermodynamic state of the emitting gas.

First, let us consider the emission of atoms, which then will be extended to molecule emission. For atoms, the only degree of freedom for excited states is given by electronically excited levels. These excited levels are not arbitrary but characteristic for each species. In the simplest case of a hydrogen atom with only one electron, the energy levels can be calculated through the Rydberg formula, resulting in a series of spectral lines emitting at wavelengths, λ:

$$\frac{1}{\lambda}=R_H\left(\frac{1}{n_1^2}-\frac{1}{n_2^2}\right), \tag{3.4}$$

where R_H is the Rydberg empirical constant. The energy levels can also be expressed in terms of the angular momentum of the electrons (by Planck) as:

$$\Delta E=\frac{k^2e^4m}{2}\left(\frac{1}{L_1^2}-\frac{1}{L_2^2}\right), \tag{3.5}$$

who also expressed R_H is given by universal constants:

$$R_H=\frac{2\pi^2k^2e^4m}{ch^3} \tag{3.6}$$

For more complex atoms with more electrons, such laws cannot be easily derived and laws for allowed radiative transitions between electronically excited states must be extracted from quantum mechanics. Detailed descriptions of the nomenclature and the basic governing processes are found for example in Refs. 22 and 23, tables for transition probabilities for the different atoms can be found in Ref. 24 or in online databases, for example published and maintained by the National Institute of Standards and Technology (NIST).[25] These transitions can be summarized in so called Grotrian diagrams.[26]

To determine the final emission coefficient, the number of particles in the upper excited state must be known. In general, this could be done by balancing all populating and depopulating processes, such as collisions (excitation and quenching), radiative transitions (absorption and emission), and chemical reactions. In thermodynamic equilibrium, the forward and backward

processes equal each other and the plasma will achieve a stationary state in which the populations of the excited states, n_2, are related to the total density of the species of concern, n_0, by a Boltzmann distribution:

$$n_2 = \frac{g_2}{Q(T_{ex})} n_0 \exp\left(-\frac{E_2}{kT_{ex}}\right) \tag{3.7}$$

with the excited state energy, E_2, the excitation temperature, T_{ex}, the multiplicity (sometimes called degeneracy) of the upper state, g_2, and the temperature dependent partition function, Q:

$$Q(T_{ex}) = \sum_i g_i \exp\left(-\frac{E_i}{kT_{ex}}\right) \quad . \tag{3.8}$$

Under nonequilibrium conditions, the population balance for each individual state has to be determined separately by considering all individual processes. Common approaches for such situations will be discussed in the second part of this chapter.

For molecular emission, the same principles used for atoms apply but additional degrees of freedom of rotation and vibration have to be considered. Internal energy now can be stored in all three degrees of freedom and a radiative transition may contain contributions of all three energies. Therefore, the relation for one photon becomes:

$$\Delta E = \Delta E_{el} + \Delta E_{vib} + \Delta E_{rot} = h\nu = \frac{hc}{\lambda} \quad . \tag{3.9}$$

The following considerations are restricted to diatomic molecules, which are relatively well understood and also are the major molecular constituents of high-temperature air (N_2, O_2 and NO). The governing processes for poly atomic molecules become rapidly too complicated to be considered in this work. Although simplified models for diatomic (considering the molecule as two point masses with a rigid massless connection (rigid rotator) or as two point masses connected by a perfectly elastic massless spring (harmonic oscillator)) are sometimes used in computational fluid dynamics to account for the internal energies, these models are not sufficient for spectroscopic considerations, in particular at high temperatures. The molecular potential are usually described by an anharmonic oscillator where the energy approaches infinity as the nuclear distance decreases and approaches the dissociation energy with increasing internuclear distance. The solutions of the Schrodinger equation yield discrete energy levels, characterized by the vibrational and rotational quantum numbers V and J. Figure 3.2 illustrates a molecular transition.

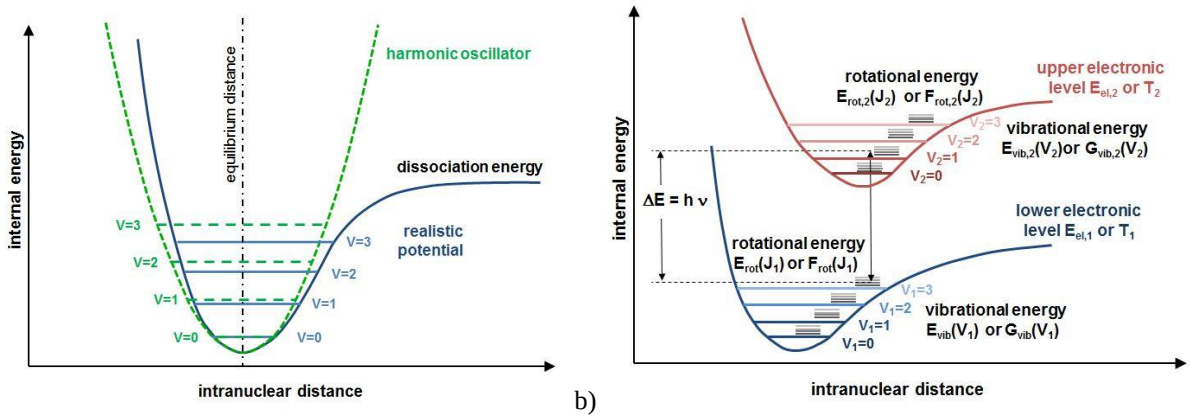

Figure 3.2. Illustrations of a) vibrational potentials of a harmonic oscillator and a realistic molecular potential, and b) a ro-vibrational transition between two electronic levels.

Recently, ab-initio computations for molecular potentials were performed using quantum chemistry.[27] However, these models require substantial computational effort both during the initial calculations and in post processing. More commonly, approximations as proposed by Dunham [28] are used where vibrational and rotational energies are approximated through polynomial series depending on the rotational and vibrational quantum numbers J and V. Usually, vibrational and rotational energies, respectively, are computed in the normalized form with the units [cm^{-1}] with the spectroscopic constants derived from empirical observation:[22]

$$G(V) = \omega_e\left(V+\frac{1}{2}\right) - \omega_e x_e\left(V+\frac{1}{2}\right)^2 + \omega_e y_e\left(V+\frac{1}{2}\right)^3 + \omega_e z_e\left(V+\frac{1}{2}\right)^4 + \ldots \tag{3.10}$$

$$F_V(V,J) = B_V J(J+1) - D_V J^2(J+1)^2 + \ldots \tag{3.11}$$

where the coupling constants B_V and D_V are given by:

$$B_V = B_e - \alpha_e\left(V+\frac{1}{2}\right) + \gamma_e\left(V+\frac{1}{2}\right)^2 + \ldots \tag{3.12}$$

$$D_V = D_e + \beta_e\left(V+\frac{1}{2}\right) + \delta_e\left(V+\frac{1}{2}\right)^2 + \ldots \tag{3.13}$$

The coefficients for these series can be found in the literature. Detailed computation of different molecules may take additional effects into account such as spin splitting, lambda doubling, etc. A rather complete description was given by Herzberg,[22] while more current molecular constants for air were published by Gilmore.[29]

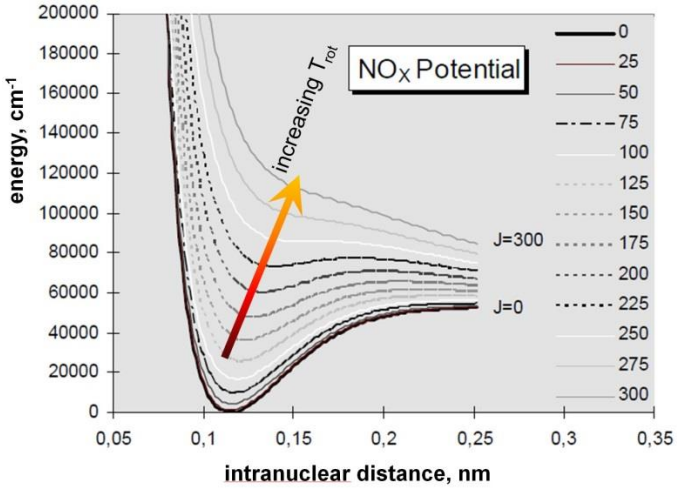

Figure 3.3. Deformation of the NO ground state potential with rotational quantum number.[30] Modified and reprinted with permission of the author.

The dependence of rotational energies on vibrational quantum numbers shown in Eq. (3.11) yields a deformation of the molecular potential with rotational excitation rather than just a vertical shift in energy as suggested by the illustration in Fig. 3.2.

The resulting potentials show a potential well above the dissociation limit (and therefore stable excited molecules with energies higher than the dissociation energy)[31] as shown in Fig. 3.3.

If a truncated Dunham series (3.10 and 3.11) after second-order terms is used, Morse showed that an exact solution for the Schrodinger equation representing the motions of the nuclei in a diatomic molecule can be found.[32] He proposed a molecular potential in the form:

$$U(x) = D_e\left(1 - e^{-\beta x}\right)^2 \tag{3.14}$$

With the well depth of the potential D_e, the difference x to the equilibrium distance r_e, and the parameter β that depends on the Eigen-frequency of the oscillator ω_0, the reduced mass of the molecule μ_A and D_e:[32]

$$\beta = 1.2177 \cdot 10^{-7}\ \omega_e \sqrt{\frac{\mu_A}{D_e}} \tag{3.15}$$

This representation, however, becomes inaccurate for high quantum numbers and more sophisticated potentials may be used, e.g. the three parameter Lippincott potential,[33] the five parameter Hulbert-Hirschfelder potential,[33] or Rydberg-Klein-Rees (RKR) potentials.[34]

For the computation of line strengths, the definition of the volumetric emission coefficient remains but the transition probability becomes a function of the relation between the upper and lower state rotational and vibrational configuration, the indices ‘ and ‘‘ indicating the upper and lower state, respectively:

$$\varepsilon_{2-1} = \frac{\Delta E}{4\pi} A_{2-1} n_2 = \frac{16\pi^3 c\,\bar{\nu}^4}{3} \underbrace{(R_e(\bar{r}_{v'v''}))^2 q_{v'v''}}_{(1)} \underbrace{\frac{S^{J'\Lambda'}_{J''\Lambda''}}{2J'+1}}_{(2)} n_2 \,. \tag{3.16}$$

J' is the rotational quantum number of the upper state, the electronic transition moment $(R_e(\bar{r}_{v'v''}))^2 q_{v'v''}$ describes the probability of a particular electronic transition depending on the inter-nuclear distance, the Honl-London factor $\frac{S_{J''\Lambda''}^{J'\Lambda'}}{2J'+1}$ indicates how the total intensity of a transition is distributed among the different branches (in the easiest case the P-, R-, and Q-branches defined by a change in rotational quantum number from the upper state to the lower state of -1, 1, or 0, respectively).

The electronic transition moment is based on the Franck-Condon principle which postulates that the internuclear distance does not change during the transition. Therefore, the wave functions of the upper and lower level will yield a higher transition probability when the overlap of the upper and lower molecular potentials is larger as illustrated in Fig. 3.4. The transitions indicated by solid lines are probable because of the overlap of wave functions. The hypothetical transition indicated by the dashed line on the right side of Fig. 3.4 is not possible because of non-overlap of the wave functions caused by the different internuclear spacing in ground and electronic states. Both the electronic transition moment and the Honl-London factor depend on the molecular species of concern.

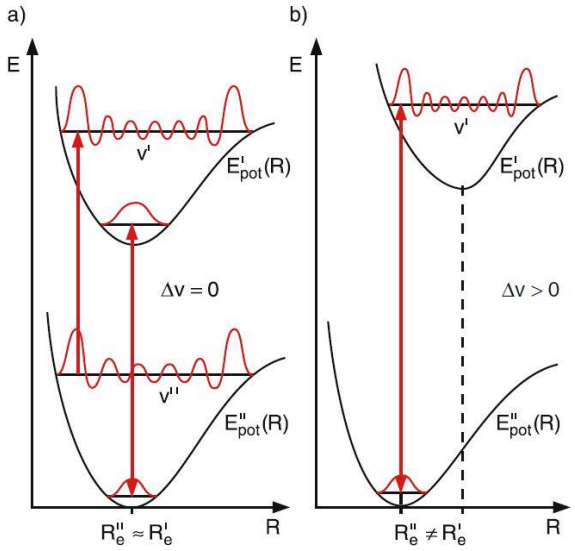

Figure 3.4. Illustration of the Franck-Condon principle. Reprinted from Ref. 61 with permission of Springer Science and Business Media.

In equilibrium, population of each energy level is distributed through a Boltzmann distribution. Although the definition of thermodynamic equilibrium postulates that only one temperature governs all distribution functions, separate temperatures for rotational, vibrational, and electronic excitation are already introduced at this point to be able to extend these considerations to different degrees of nonequilibrium. Therefore, the upper-state density now depends on three temperatures and can be described through a combination of three Boltzmann distributions of rotational, vibrational, and electronic energy:

$$N_2 = N_{tot} \frac{g_{e'}\left(2J'+1\right)}{Q\left(T_{el},T_{vib},T_{rot}\right)} \exp\left(-\frac{E_{el}^{e'}}{kT_{el}}\right) \exp\left(-\frac{E_{vib}^{e'V'}}{kT_{vib}}\right) \exp\left(-\frac{E_{rot}^{e'V'J'}}{kT_{rot}}\right) \tag{3.17}$$

with the partition function:

$$Q = \sum_{e'V'J'} Q_{el}^{e'}\, Q_{vib}^{e'V'}\, Q_{rot}^{e'V'J'} = \sum_{e'V'J'} g_{e'} \exp\left(-\frac{E_{el}^{e'}}{kT_{el}}\right) \exp\left(-\frac{E_{vib}^{e'V'}}{kT_{vib}}\right)(2J'+1)\exp\left(-\frac{E_{rot}^{e'V'J'}}{kT_{rot}}\right) \qquad (3.18)$$

electronic *vibrational* *rotational*

3.2 Line shape of emission lines and line broadening

So far, each emission line was considered to be emitted at one discrete wavelength determined by the energy difference of the upper and lower different states. However, emission and absorption lines can be broadened through different processes (some of which are detailed in the next section on Absorption Spectroscopy) such as:

- natural broadening due to the Heisenberg uncertainty principle (Lorentzian)
- Doppler broadening due to the thermal motion of the emitting particles (Gaussian)
- Collision broadening (Lorentzian)
  - Van-der-Waals due to collisions with neutrals
  - Resonance broadening due to collisions with the like species (perturber's state connected by an allowed transition to the upper or lower state of the transition)
  - Stark for interactions with ions or electrons, specific for each transition/line
- Zeeman effect due to interaction with magnetic fields (Lorentzian)

Each of these processes actually causes a line shift for each photon. The integration over many photons with different shifts produces a broadening by distributing the transition energy over a certain wavelength (or wavenumber) range. Depending on the physical effect, the final line shape will follow a Gaussian or a Lorentzian profile. Usually, the broadening is described by the linewidth at its half maximum (full width, FWHM, or half width, HWHM). Half widths of Lorentz profiles can be summed up linearly, half widths of Gaussian profiles can be summed in quadrature: $FWHM_{G,total} = \sqrt{FWHM_{G,1}^2 + FWHM_{G,2}^2}$. If several processes occur simultaneously, the resulting broadening may be described by a Voigt profile. Spectral lineshapes are detailed in Section 4 of this manuscript, which focuses on Absorption Spectroscopy.

3.3 Spatial resolution

One major disadvantage of emission spectroscopy (shared with absorption spectroscopy) is the integrating character of the measurements. Even if the set-up is focused on one particular point in the field of view (e.g. the center line of a flow field), the detected signal is not limited to that point. In a radiating volume, the measured signal will result from an integration along the line of sight with all cross sections along this line contributing with equal efficiency as long as the local cross section defined by the limiting rays does not exceed the volume dimensions. The measured integrated intensity *I(z)* is coupled to the local emission coefficient *ε(r)* by the Abel equation: [35]

$$I(z) = 2\int_{r=z}^{R} \frac{r}{\sqrt{r^2 - z^2}}\ \varepsilon(r)\ \ dr \qquad (3.19)$$

where R is the outer radius of the measured volume, z the off-axis position, and r the local radius. Solving for $\varepsilon(r)$ yields

$$\varepsilon(r) = -\frac{1}{\pi}\int_{z=r}^{\infty} \frac{\left(dI/dz\right)}{\sqrt{z^2 - r^2}}\, dz \quad . \tag{3.20}$$

In the special case of axi-symmetry and an optically thin volume radiator, local emission values can be determined by analyzing a series of off-axis lines of sight. For the example of a homogeneously emitting medium, an elliptic distribution of the measured emission versus off-axis position will be obtained. Local values may be obtained by applying a so-called Abel-inversion. However, an analytical solution can only be found if the measured profile versus off-axis position can be described by particular functions (such as a Gaussian distribution, a pair polynomial function, or elliptic functions). In the general case, i.e. if the measured profile $I(z)$ cannot be described by one of the above mentioned functions, approximate methods can be used. The most common one is the "onion peeling" method:

Each measurement is interpreted as an average over a ring with constant emission coefficient measured at an off-set value z_j. The emission along the lines of sight is then the sum of the individual emission coefficients e_i times the length $L_{j,i}$ with which the line of sight cuts each individual ring r_i ,yielding a rather simple system of linear equations. The geometric principle is illustrated in Fig. 3.5(a) for 4 measurement positions. The system for 4 lines of sight reads as:

$$\begin{aligned}
I_{3,int}(z_3) &= \varepsilon(r_3)\ L_3(r_3) \\
I_{2,int}(z_2) &= \varepsilon(r_3)\ L_2(r_3) + \varepsilon(r_2)\ L_2(r_2) \\
I_{1,int}(z_1) &= \varepsilon(r_3)\ L_1(r_3) + \varepsilon(r_2)\ L_1(r_2) + \varepsilon(r_1)\ L_1(r_1) \\
I_{0,int}(z_0) &= \varepsilon(r_3)\ L_0(r_3) + \varepsilon(r_2)\ L_0(r_2) + \varepsilon(r_1)\ L_0(r_1) + \varepsilon(r_0)\ L_0(r_0)
\end{aligned} \tag{3.21}$$

and can even be solved recursively for small numbers of off-axis positions or through matrix inversion for a larger set of measurements. For this method, the individual lines of sight do not have to be parallel to each other, e.g. if the variation of z is realized through tilting the optical axis rather than moving the set-up, as illustrated in Fig. 3.5(b). To reach higher accuracy, radial distributions over each ring element might be assumed and included in the set of equations.

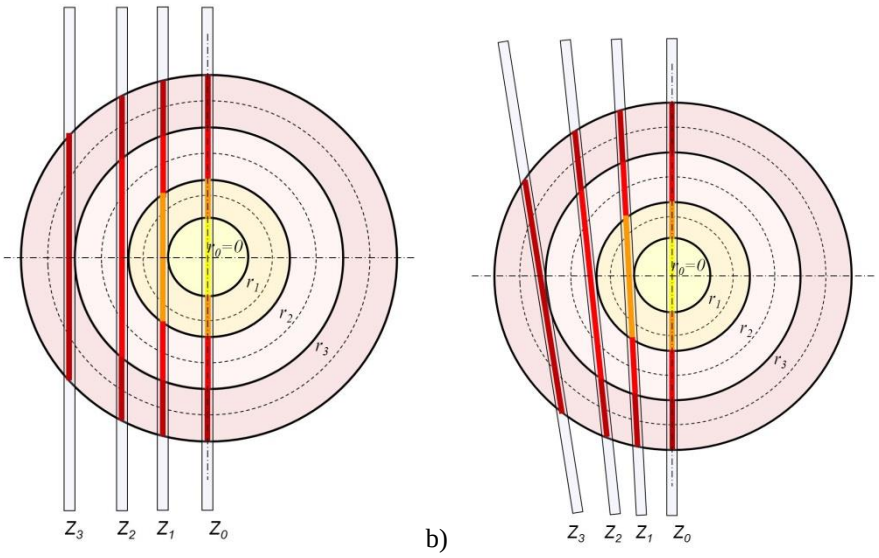

Figure 3.5. Illustration of the Abel-inversion principle for a set of off-axis measurements a) parallel to the rotational symmetric radiation field, and b) realized through tilting the detection set-up (from reference 36). Reprinted with permission of the authors.

3.4 Analysis of emission spectroscopy data:

The most traditional application (e.g. in astronomy, or process control in industrial applications) of emission spectroscopy is probably the identification of radiating species in the emitting medium. Even for an unknown thermodynamic state of the emitting medium, the simple occurrence of particular emission lines is proof for the existence of the element of concern. If a number of species contribute to the unknown spectrum, the occurrence of multiple lines of the same element can provide a conclusive identification. Since the emitted spectrum will change with temperature, some basic knowledge of the thermodynamic state might be required already at that stage of interpretation. For industrial applications, an engineering approach might be suitable where spectra are recorded at the desired condition, and only deviations from these spectra are used as indication for a possible failure of the process without even knowing the cause.

If quantitative measurements of the chemical composition are intended, however, the thermodynamic state of the emitting medium has to be known to a significant accuracy. All atomic emission lines (and most molecular spectra in the visible to near-infrared region) will originate from electronically excited states. Quantitative interpretation of these spectra requires detailed knowledge of the population of these excited states and their link to the ground state of the species of concern which, even at high temperatures, usually contains the highest density. Without detailed collisional models, quantitative interpretation usually requires the validity of Boltzmann distributions, and therefore an assumption of equilibrium. In general, equilibration will be reached through collisional energy exchange. As described in the introduction, the

various forms of internal energies (rotational, vibrational, and electronic excitation) require different numbers of collisions to equilibrate. While some 10s of collisions are needed to equilibrate rotational excitation, vibrational equilibration already requires some 100s of collisions, and electronic excitation may be reached after several 1000s of collisions during the life time of the excited states.[37] Therefore, equilibration of electronic excitation with the ground states is most likely achieved at high pressures.

3.4.1 Temperature determination methods

While number densities usually require quantitative knowledge of the absolute measured emission, temperatures can be obtained from the qualitative spectral appearance, e.g. from relative line ratios or line shapes. At low pressures, the dominant broadening mechanism of emission lines is the Doppler broadening which is related to the translational temperature through equation 3.21. If the emission lines are measured with sufficiently high spectral resolution, a Gaussian profile can be fitted to the measured line shape and the extracted half width can be evaluated with respect to the governing temperature. The basic assumption is only that the concept of temperature is defined which implies that the thermal velocities are distributed according to a Maxwell distribution. No information about the strength of the measured line is needed. Typical half widths for temperatures up to 10s of thousands of Kelvins are on the order of 10s of picometers (~0.5 cm) at maximum. Such spectral resolution is usually obtained through interferometers (e.g. Fabry-Perot interferometers) or Echelle spectrometers. The main influences on the measured data are usually the instrument broadening of the set-up used and line broadening caused by other physical effects that are potential error sources that need to be modeled and corrected for. The higher the pressure, the more dominant collisional broadening becomes but collision broadening typically decreases with $T^{0.5}$ while Doppler broadening increases with $T^{0.5}$ (from Eq. 3.11).[37] For the individual lines of carbon dioxide (CO_2) or water (H_2O), for example, the Doppler broadening will be dominant at 0.1 atm or below for temperatures higher than 1000 K, while at 1 atm Doppler and collisional broadening are on the same order of magnitude for temperatures of 3000 K (compare Fig. 10-7 in Ref. 37).

If a significant amount of ionization occurs (e.g. in electrically-heated plasmas), Stark broadening through interaction of excited electronic states with the electrons may contribute to the line broadening. This can potentially interfere with temperature measurements or alternately, allow electron number density measurements. However, Stark broadening factors are different for each individual transition,[38] so an appropriate choice of emission lines under investigation may provide useful temperature measurements, even at significant degrees of ionization. On the other hand, the broadening of selected lines (e.g. the hydrogen lines H_α or H_β) may provide measurement of electron density.[15, 39] If no hydrogen is available in the original plasma composition (e.g. for air plasmas) it has been shown that even intentional seeding with small amounts of hydrogen enables electron density measurements at hypersonic conditions while not significantly altering the plasma state.

If lines originating from the same atom or molecule but different excitation energies are measured simultaneously, governing temperatures can be determined from ratios of the total emission of the individual transitions. This data is obtained by integrating the measured spectrum over the line shape (in the following referred to as line emission). If a Boltzmann distribution of the excited states can be assumed, the ratio of different emission lines can be analyzed by evaluating the distribution function with respect to temperature. If the thermodynamic state of the emitting medium is not known to be in equilibrium it is appropriate to analyze more than two emission lines to determine the temperature and, at the same time, prove the validity of the Boltzmann distribution using a so called Boltzmann plot. If the equation for the electronic excitation of atoms is written as

$$\ln\left(\frac{I_{2-1}}{\nu A_{2-1} g_2}\right) + const = -\frac{E_2}{kT_{ex}} \tag{3.22}$$

with $I_{2\text{-}1}$ being measured line intensities for upper state excited energies E_2. A plot of the logarithmic terms vs. excitation energy follows a straight line if the upper state densities are Boltzmann distributed. The agreement with this straight line shows the validity of a Boltzmann distribution, the slope contains the desired excitation temperature (slope = $-1/(kT_{ex})$). The higher the difference in excitation energy, the better the accuracy of the measurement, a rule that will be discussed in more detail in the context of PLIF in section 4.5.

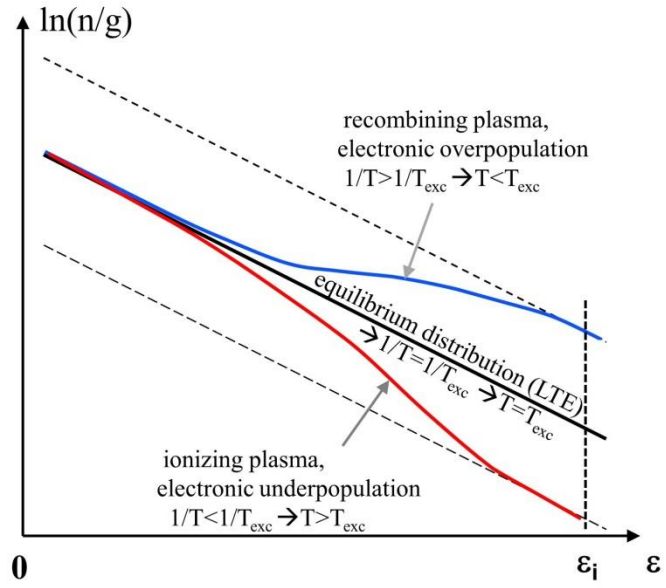

Figure 3.6. Effects of the plasma state on electronic excitation temperature in comparison to equilibrium temperature, based approximately on data in Ref. 40.

However, even if the Boltzmann plot indicates a Boltzmann distribution of the excited levels under consideration, the resulting temperature might not necessarily equal the equilibrium temperature. As illustrated in Fig. 3.6, in a recombining or ionizing plasma, the population of high electronic levels might be modified with respect to the equilibrium population through the chemical processes (overpopulation of highly excited levels in a recombining plasma, underpopulation in the ionizing case) yielding a Boltzmann-like distribution within the measurement accuracy with a governing temperature different from the equilibrium temperature.

If the same procedure as described above is applied to molecules, similar equations can be derived for rotational, vibrational, and electronic excitation. The individual temperatures can be determined by appropriate selection of evaluated emission lines (for T_{rot}, all lines under consideration should originate from the same upper and lower vibrational and electronic levels, etc.). Figure 3.7 gives an example of a Boltzmann plot to determine the rotational temperature of N_2^+ in an air plasma from different rotational lines of the 0-0 transition of the N_2^+ 1st Neg. System.

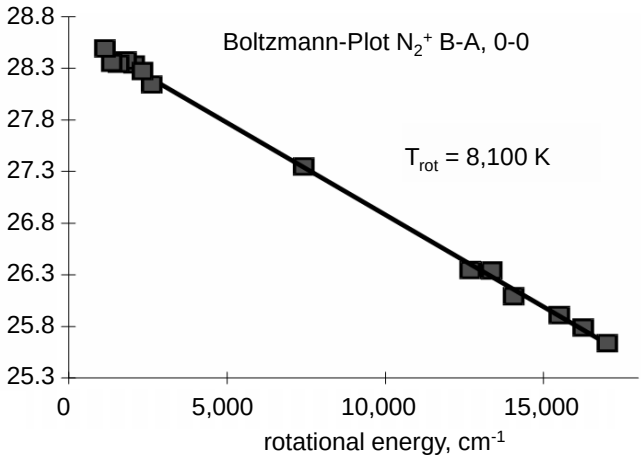

Figure 3.7. Boltzmann-Plot for the determination of rotational temperature from rotational lines of the 0-0 transition of the N_2^+ 1st Neg. system in an air plasma based on data from Ref. 30. Reprinted with permission of the American Institute of Aeronautics and Astronautics.

A more common approach in the last few decades, however, to determine vibrational or rotational temperatures is a comparison of a low resolution molecular spectrum with theoretical simulation. The band shapes are usually characteristic for the rotational temperature, band ratios of different upper vibrational excitation levels may be used to determine vibrational temperatures. Again, this method does not necessarily require intensities calibrated to absolute values since only band ratios are used. It is, however, mandatory to at least perform a relative calibration within the wavelength range of concern, even if this range is rather narrow.

3.4.2 Simulation Codes

Over the years, several codes for the simulation of plasma emission with particular respect to the application to hypersonic flows have been developed worldwide. In the following, only line-by-line approaches are summarized. In these codes, emission, absorption, and broadening properties for each individual transition of the species of concern are calculated, and a final spectrum is composed through a superposition of all lines under consideration. In comparison with other methods (smeared band, narrowband, or wideband models) that are usually faster, line by line models still yield the most accurate simulation and offer the advantage of covering all ranges of spectral resolution (e.g. through simulation in high spectral resolution, followed by a spectral integration). Typically, lines of sight through a radiating volume with known composition are constructed and the emission is propagated through this volume. Typical applications are found in rebuilding experimental conditions in ground experiments or flight for a comparison of measured data. Another task is to determine radiation loads in ground test facilities or, even more important, in flight situations to determine final loads and support the

design process. A list of some important codes is given in Table 3.1. Again, it is not possible to cover all existing codes, so the list was compiled with the intention of being representative but not comprehensive. Typically, these codes are under continuous development to account for recent simulation demands (e.g. adding radiating species for atmospheric entries into other celestial bodies' atmospheres, the most recent examples being Mars, Titan, or Venus) and new physics models being developed.

Table 3.1. Representative (but not comprehensive) list of codes for the simulation of plasma radiation.

Code (Organization, Country)	Simulated species	Radiation Transport capabilities	Restrictions/availability	Ref.
NEQAIR (NASA Ames, USA)	Air, H, H_2, C, CN, CO_2	Line of sight, spherical cap, infinite slab	EAR restricted	41
HARA (NASA Langley, USA)	Air, H, H_2, C, CN, CO_2, Ar	Line of sight, spherical cap, infinite slab	EAR restricted	42
SPRADIAN/*RADIPAC* (JAXA, Japan/South Korea)	Air, H, H_2, C, CN, CO_2, Ar	Line of sight, spherical cap, infinite slab	none, available through JAXA	43
PARADE (ESA, Europe)	Air, NH, C, CN, CH, C_2	Ray tracing through additional Fortran code (Herta)	none, available through ESA	44
SPECAIR (Ecole Centrale, France)	Air, H, H_2, C, CN, CO_2, Ar	None	reduced version available for download [45]	39
LIFBASE (SRI, USA)	OH, OD, NO, H, CN, CF, SiH, N_2^+	None	none, available for download [46]	47
SPARTAN (*ipfn*, Instituto de Plasmas e Fusão Nuclear, Portugal)	Air		freely distributed for academic and research	48
HYPERRAD, (NASA Ames, USA)	Air		EAR restricted	27
CNRS-RAD DATABASE, (Ecole Centrale, France)	Air, CN, CO, CO^+, C_2	None	Available as spectroscopic database	49,50

Note: "Air" is: N_2, O_2, NO, N, O, N_2^+

3.5 Application examples of emission spectroscopy

Below we present some typical examples of the application of emission spectroscopy to hypersonic flows in ground test facilities. There is a wide spectrum of facilities operational around the world which may be divided up into impulse and stationary facilities. Shock tubes belong to the first category. They typically recreate the hypersonic flight regime accurately but provide only short test times. Stationary facilities provide sufficient test time to yield a realistic material response for thermal protection system (TPS) qualification but only partially rebuild a true flight environment. Both types of facilities need plasma diagnostic methods to characterize the flow, emission spectroscopy being widely applied.

In impulse facilities, imaging set-ups have been used in recent years to take a snapshot of the flow propagating through the test section while gaining simultaneous spectral information from the entire shock and post-shock system.[15,51] Figure 3.8 shows such an image with extracted spectra and spatial intensity distributions across the shock and the post-shock region.

The purpose of recent work was to experimentally quantify radiation loads to spacecraft during atmospheric entry to reduce margins in the design process, mainly due to equilibrium radiation generated in the post-shock region. However, increased interest in the nonequilibrium radiation inside the shock and in the immediate relaxation region has been expressed recently.[52]

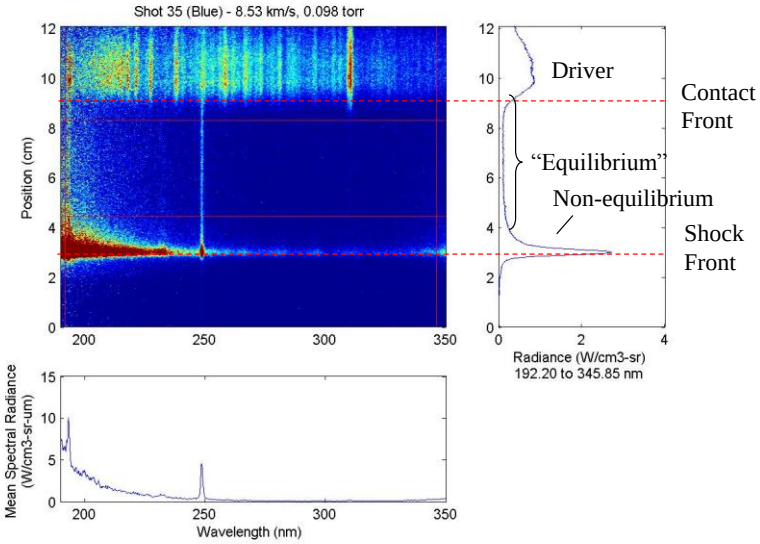

Figure 3.8. Example of data obtained from a single spectrograph in the EAST facility. Vertical and horizontal cross sections of the data shown depict the spatial and wavelength resolved data, respectively.[51] Reprinted with permission of the American Institute of Aeronautics and Astronautics.

A simple to interpret case of emission spectroscopy is plasma states in thermodynamic equilibrium. For most high-temperature air species, the simulation capabilities are sufficient to reproduce measured spectra. A good example is given by data taken at Stanford University in an atmospheric, inductively coupled plasma torch by *Laux et al.*[39] Figure 3.9 shows measured and simulated emission spectra in that equilibrium case that are in excellent agreement.

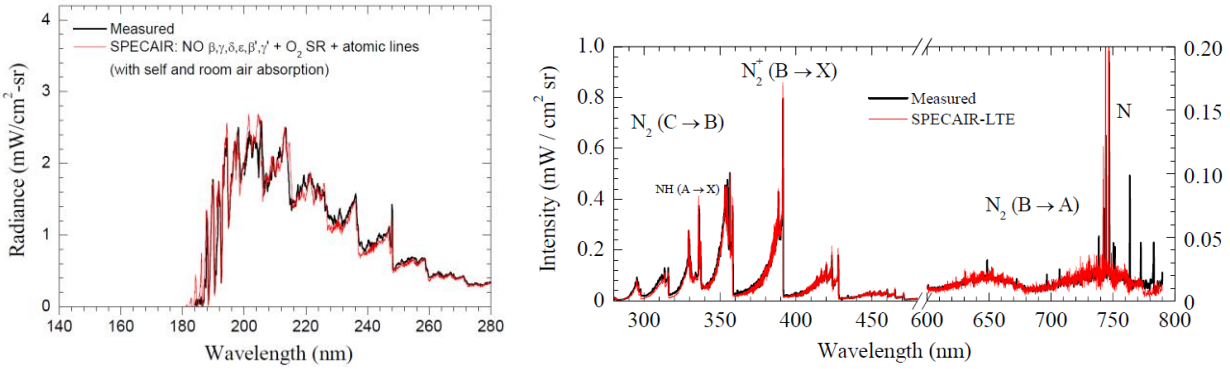

Figure 3.9. SPECAIR: NO β, γ, δ, ε, β', γ', O_2 SR and atomic lines, including self-absorption within plasma and absorption in 5 m of room air in the low UV (left), and measured and computed LTE spectra of the nitrogen/argon plasma at the generator nozzle exit from the near-UV to the near infrared.[39] Credentials to von Karman Institute for Fluid Dynamics, in Radiation and Nonequilibrium Collisional-Radiative Models by C.O. Laux, VKI LS 2002-07.

These measurements demonstrate the ability to make absolute concentration measurements using OES; in this case the absolute intensity of N_2 emission matches the predicted emission assuming equilibrium chemistry.

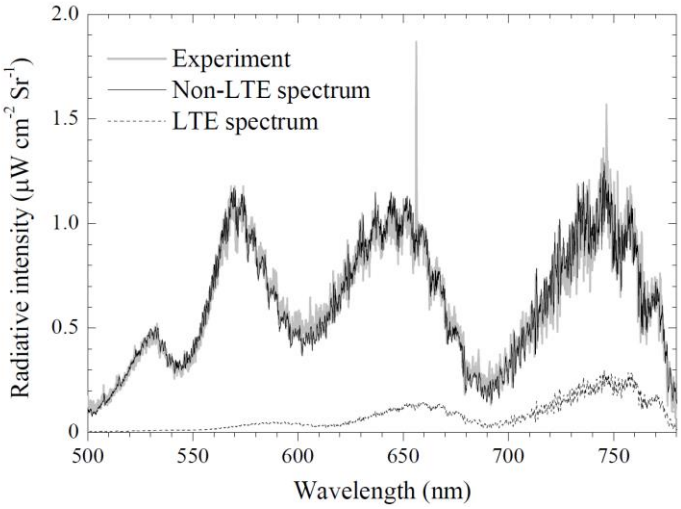

Figure 3.10. Measured spectra and computation assuming LTE and non-LTE simulation of a nitrogen/argon plasma after rapid cooling from an equilibrium state from Ref 39. Credentials to von Karman Institute for Fluid Dynamics, in Radiation and Nonequilibrium Collisional-Radiative Models by C.O. Laux, VKI LS 2002-07.

Sometimes changes in the gas dynamic state happen too fast for the plasma to reach equilibrium (both in the thermal and chemical sense). In this case, populations of the excited states may no longer follow well defined (Maxwellian) distribution functions. An analysis requires a detailed balance of population and depopulation for each excited state, yielding the necessity of collisional radiative models. The assumption of a quasi-steady-state, where the time change of the excited states is considered small against the population processes themselves, is often applied as described by *Park*[31] and may hold over a wide regime of conditions. However, additional population processes may become dominant, in particular those through chemical reactions, requiring knowledge of excited-state chemistry. Evidence of excited state chemistry was found during the space shuttle development in the so called "shuttle glow". This basic process was thoroughly described by *Golde and Thrush.*[53] Excited states are populated through chemical reactions that end up directly in these states without the need of collisional excitation from the ground state. The final radiating level might even be populated through overlapping potentials (usually of molecules) through level crossing processes.[54] An experimental realization was given by *Laux et al.* by rapidly cooling down an equilibrium plasma. The molecular emission of N_2 from the 1st Pos. System ($N_2\ B^3\Pi_g \rightarrow N_2\ A^3\Sigma_u^+$) was monitored and showed strong deviations from the simulation based on thermal excitation with significant overpopulations of high vibrational quantum numbers, as illustrated in Fig. 3.10.

Indeed, these overpopulations could be related to the aforementioned level crossing processes (also known as inverse pre-dissociation) and the spectrum was rebuilt applying collisional radiative models.[54] Recently, the same processes have been shown to be dominant for the emitted radiation of N_2 in highly expanding high-enthalpy flows used for TPS material testing at NASA by *Winter et al.*[36] as demonstrated in Fig. 3.11. The measured spectrum can only be rebuilt by introducing significant overpopulation factors for high upper vibrational quantum numbers (V_u=8 to V_u=13) of the emitting electronic state of N_2. It was shown that the molecular

radiation (at least of these high vibrational levels) is not produced by excitation of N_2 ground state molecules but by recombination of N atoms into electronically excited N_2 levels. This provides a potential method for measuring ground state atom concentrations in nonequilibrium flows without the need of much more complicated techniques such as two-photon laser-induced fluorescence (TALIF).

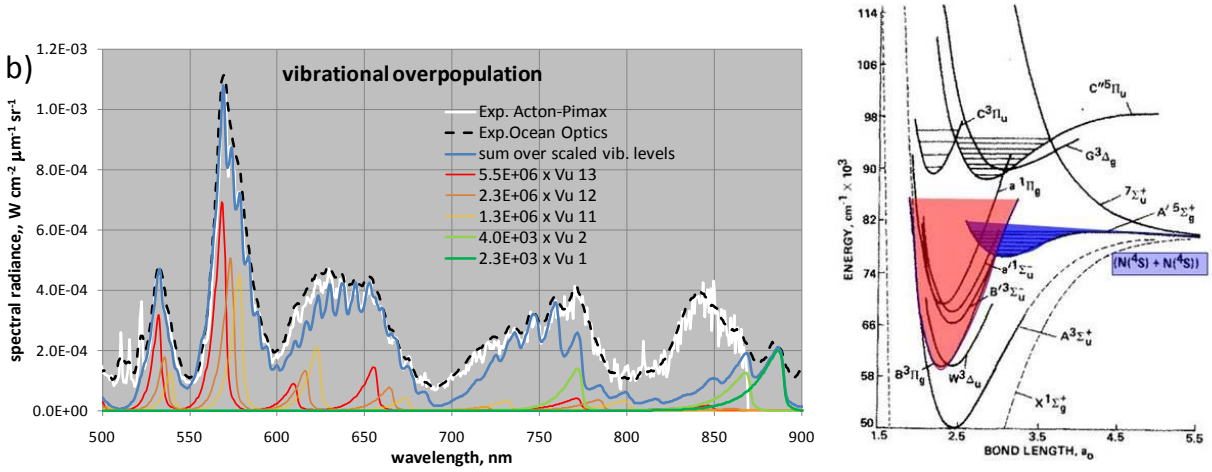

Figure 3.11. Measurements of the N_2 1st Pos System in the free stream of the IHF arc-jet facility in comparison to LTE simulation with NEQAIR and superposition of individually scaled spectra simulated separately for each upper vibrational level (left),[36] and potential crossing between the N_2 $A'^5\Sigma_g^+$, and N_2 $B^3\Pi_g$ states[54] (right), which is reproduced with permission from the authors. Right hand figure is Copyright 1988, AIP Publishing LLC.

4. Absorption Spectroscopy

Absorption spectroscopy has been used to study nonequilibrium flows since at least 1961.[55] In their textbook on Gas Dynamics, Vincenti and Kruger describe how Camac (1961) used the technique to measure vibrational relaxation times behind normal shock waves in oxygen-argon mixtures.[56] Camac used a xenon-filled microwave-excited resonance lamp, a hot cathode hydrogen discharge tube, and a high-voltage Lyman discharge lamp to produce the ultraviolet light needed for the absorption measurements. Absorption spectroscopy has been since used to extract other quantitative thermodynamic and fluid dynamic properties flows such as temperature, pressure, species concentration, and velocity.

4.1 Absorption Theory

Quantitative measurements are achieved with absorption through the analysis of the fluid's interaction with light. As light, with spectral irradiance I_ν [W/cm^2/cm^{-1}] propagates through an infinitesimal thickness dx [cm] of an absorbing medium of concentration C [molecules/cm^3] with a molar absorption coefficient ε [cm^2/molecule], its intensity decreases according to:[57]

$$-dI_\nu = I_\nu \varepsilon C dx \tag{4.1}$$

Using a spectral absorption coefficient k_ν [cm^{-1}], which is equivalent to the product of ε and C, Eq. 4.1 can also be written as:[58,59]

$$-dI_\nu = k_\nu I_\nu dx\,. \tag{4.2}$$

Integration of this equation gives the well-known Beer-Lambert law:

$$\frac{I_\nu}{I_0} = e^{-\int k_\nu dx}\,. \tag{4.3}$$

In this equation, I_0 is the incident irradiance prior to absorption. If the medium can be specified by a single temperature, velocity, and absorbing species concentration and the pressure is uniform and absorbs linearly over the path length L, the relationship can be simplified to:

$$\frac{I_\nu}{I_0} = e^{-k_\nu L}\,. \tag{4.4}$$

The parameter k_ν contains key information about the absorbing medium, including the population of potential absorbers and the probability of absorption. Strategies that exploit the relationship between this information and thermodynamic properties lead to various quantitative measurement techniques. Contributions to k_ν can be better explained with the aid of an energy diagram. Figure 4.1 shows incident light being absorbed, which causes molecules to transition from an energy ground state (E_1) to an energy excited state (E_2). The energy of the incident photon, which is the product of Planck's constant h and the frequency of the light ν, is transferred to the excited molecule.

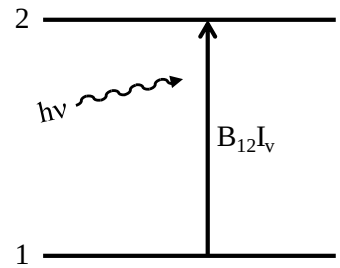

Figure 4.1. Two-level energy diagram of absorption process.

Not all potential absorbers in the ground state are excited. The rate of absorption is governed by the transition line-shape function Y_ν [cm] and the transition line-strength factor S_{12} [cm^{-2}]. These two components contribute to the spectral absorption coefficient:[60]

$$k_\nu = S_{12} Y_\nu\,. \tag{4.5}$$

If we assume that the population in the upper state is negligible, S_{12} is proportional to the population of absorbers in the ground state N_1, Einstein's coefficient of stimulated absorption B_{12} [s^{-1}(W/cm^2/cm^{-1})$^{-1}$] and the energy of the incident photon. Y_ν describes the shape of the transition, spectrally, and is related to the probability that molecules will absorb photons at various frequencies. By definition, the transition line-shape function is integrated to give:

$$\int Y_\nu d\nu = 1 \ . \tag{4.6}$$

Light sources typically have a discrete spectral width, which further complicates the process. The spectral irradiance of light can be calculated from:

$$I_\nu = IL_\nu \tag{4.7}$$

where I [W/cm^2] is irradiance and L_ν [cm] is the line-shape function of the light source. Similar to Y_ν, L_ν is defined as:

$$\int L_\nu d\nu = 1. \tag{4.8}$$

To account for these two different line-shape functions, the integrated absorption coefficient is used:

$$k_{\text{int}} = S_{12}G\,, \tag{4.9}$$

where G is the spectral overlap integral defined as:

$$G = \int Y_\nu L_\nu d\nu \tag{4.10}$$

The spectral overlap integral represents the amount of intersection between the light source line-shape and the transition line-shape. There are two extreme cases to consider.[59] The first case assumes a monochromatic light source and a relatively broad absorption transition. Here, G approaches the value of Y_ν at the light source's frequency. A spectral scan of a relatively broad transition using a narrow-band laser to determine the absorption line-shape is an example of this case. The second case assumes a monochromatic absorption transition and a broadband light source. Here, G approaches the value of L_ν at the absorption transition's frequency. Note that Eq. 4.10 can be used to calculate G for all cases. For single-mode diode lasers the approximation of a monochromatic laser is frequently used. This is because the laser line-width is of the order of 10s of MHz while transitions are of the order of a few GHz at standard atmospheric conditions. However, at low-density conditions, such as those appropriate to flight in the upper atmosphere, the monochromatic approximation may no longer be valid. In these cases, corrections such as Eq. 4.10 need to be used.

4.2 Broadening Mechanisms

The transition line-shape is influenced by broadening mechanisms, which have various thermodynamic dependencies. Typically, the spectral width and shape of the transition are affected by natural ($\Delta\nu_N$), collision ($\Delta\nu_c$), and Doppler-based ($\Delta\nu_D$) broadening mechanisms. Natural and collision broadening are homogenous where each absorber has the same transition energy and frequency. Natural broadening is related to the Heisenberg uncertainty principle, as

the frequency of the transition cannot be perfectly known. Natural broadening is usually small in comparison to the other broadening mechanisms.[61] Collision or pressure broadening occurs from physical collisions with other molecules. Not only do collisions increase the spectral width ($\Delta\nu_c$), they also cause a shift ($\Delta\nu_s$) in the center frequency and asymmetry in the line-shape. For a multi-component gas mixture, these values can be calculated from: [62]

$$\Delta\nu_c = P\sum_i \left(\chi_i 2\gamma_i\right) \tag{4.11}$$

$$\Delta\nu_s = P\sum_i \left(\chi_i \delta_i\right) \tag{4.12}$$

where P, χ_i, $2\gamma_i$, and δ_i are the pressure, mole fraction, collision width per unit pressure, and collision shift per unit pressure, respectively, of the absorbing molecules. The terms γ_i, and δ_i have temperature dependencies which, for many species of interest to absorption spectroscopy can be evaluated with the High Resolution Transmission (HITRAN) database.[63] As we shall see, the temperature can be determined through the area ratio of two transitions. Because the effects of pressure are the same for both transitions, these effects cancel in the integrated signal ratio allowing an unambiguous temperature measurement. If the temperature is known, then the analysis of the collision shift and/or collision broadening can be used to calculate the gas pressure. Homogeneous broadened transitions have a Lorentzian line-shape function:

$$g_H = \frac{\Delta\nu_H}{2\pi}\frac{1}{\left(\nu-\nu_0\right)^2+\left(\Delta\nu_H/2\right)^2} \tag{4.13}$$

where $\Delta\nu_H$ is the spectral width of a homogeneous broadened transition (full width half maximum).

Doppler broadening is inhomogenous, where each absorbing molecule has a transition frequency that is Doppler shifted according to its velocity component in the laser propagation direction. This is because of thermal motion, which induces Doppler shifts. Doppler broadened transitions have a Gaussian line-shape function:

$$g_D = \frac{2(\ln 2)^{1/2}}{\pi^{1/2}\Delta\nu_D} e^{\left[\frac{-4(\ln 2)(\nu-\nu_0)}{\Delta\nu_D^2}\right]} \tag{4.14}$$

where v_0 is the center frequency corresponding to a stationary absorber.

When both homogeneous and inhomogeneous broadening mechanisms contribute to the line-shape function, the Voigt function is used.[58] The Voigt function is a convolution of the Lorentzian and Gaussian profiles:[64]

$$V(a,x) = \frac{a}{\pi}\int_{-\infty}^{\infty} \frac{e^{-y^2}}{a^2 + (x-y)^2}\, dy \tag{4.15}$$

where

$$a = \sqrt{\ln 2}\,\frac{\Delta\nu_H}{\Delta\nu_D} \tag{4.16}$$

$$x = 2\sqrt{\ln 2}\,\frac{(\nu - \nu_0)}{\Delta\nu_D}. \tag{4.17}$$

Physically, the use of the Voigt profile can be justified by each collection of molecules or atoms in a particular Doppler subgroup being subject to the effects of collisional broadening, and this is expressed through the convolution operation. The Voigt function *V(a,x)* cannot be solved analytically but is usually calculated using numerical methods. Figure 4.2 illustrates the different line shapes computed using an approximation to Eq. 4.15.[65] Figure 4.3 shows the effect of Lorentzian and Gaussian broadening on the spectral shape of a line using the fraction of the total transition energy contained within a given frequency difference from the line center. With Gaussian broadening dominant, 99% of the transition strength is contained within two half widths at half maximum ($\Delta\nu_{HWHM}$), whereas for a Lorentzian profile, this value is not reached for ~50 half widths. In other words, a strong Lorentzian-broadened line might significantly influence distant spectral regions if Lorentz broadening is dominant.

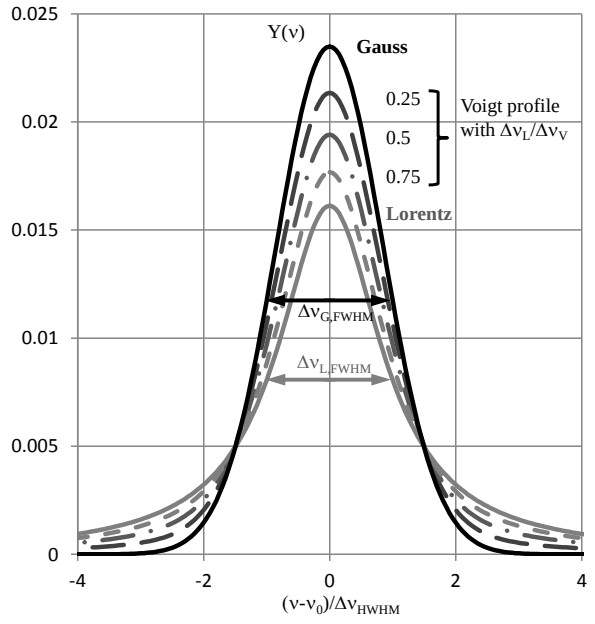

Figure 4.2. Spectral line shape for Lorentz (collision), Gaussian (Doppler) and Voigt broadening for equal transition strength and half-width.

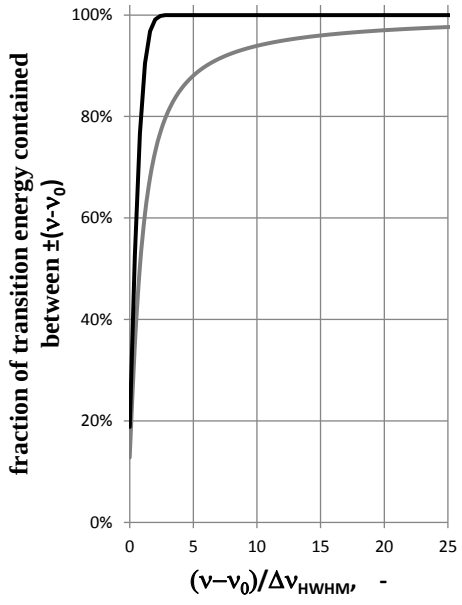

Figure 4.3 Fraction of transition energy contained between ($\nu-\nu_0$) for a Lorentzian (collision) and a Gaussian (Doppler) line profile.

4.3 Translational Temperature

If $\Delta\nu_D$ can be measured, then the translational temperature T_{trans} can be determined by the following relationship:[59]

$$\Delta\nu_D = 2\nu_0\sqrt{\frac{2kT_{\text{trans}}}{(\text{MW})c^2}\ln 2} \tag{4.18}$$

where k is Boltzmann's constant and MW is the molecular weight of the absorber. If other broadening mechanisms are small in comparison and a spectrally narrow light source is used to spectrally scan across the transition, then $\Delta\nu_D$ can be extracted with relative ease to determine the translational temperature. Even in flows with considerable homogeneous broadening the translational temperature can be determined from the Doppler component of the Voigt line-shape.[66] Using linewidth to determine translational temperature has the advantage of only requiring a single absorption line. This is particularly useful for absorption measurements of atomic species where there may only be one transition available within a laser's output range, or for lasers that have a very limited tuning range. It is also necessary for measurements in cases where there is nonequilibrium between rotational and translational energies. Measurements of translational temperature based upon transition width may have higher uncertainties compared to measurements of rotational or vibrational temperature based upon a Boltzmann plot.[67] This is because of the square-root dependence of the Doppler width on temperature and the additional challenge of separating the Doppler width from other broadening mechanisms, especially at high pressures, when measuring translational temperature.[68] For example, an uncertainty of 1.5% in the measurement of the Doppler width in *A*-band Doppler-broadened oxygen lines at 296 K leads to an uncertainty in temperature of 3%. Zhang *et al.*[69] measured the translational temperature in an arcjet facility using absorption of Argon at 811 nm. The Doppler width was measured with an uncertainty of 12% after the effects of homogeneous broadening, Stark broadening and noise were accounted for, leading to an uncertainty in the translational temperature of less than 30% over temperatures from 2000 K to 10,000 K. The difference in sensitivity between line-strength-based temperature measurements and Doppler width measurement depends strongly on the difference in ground-state energies between the available transitions.

Another example of a translational temperature measurement is described in the work of Parker *et al.*, where absorption experiments were performed in the Large Energy Shock Tunnel (LENS I) at the Calspan-University of Buffalo Research Center (CUBRC).[70] Quantum cascade lasers were used to obtain absorption measurements of NO deep into the infrared spectrum. Figure 4.4 shows a sample absorption spectra from that work near 5447 nm (1835.56 cm^{-1}), which corresponds to one of six fundamental NO rovibrational transitions used in that study. Using the Doppler width contribution based on the fitted Voigt line-shape, a translational temperature of 190 K was computed (Eq. 4.18). This temperature, measured in the test section,

corresponds to a lower enthalpy condition (5 MJ/kg) and using a helium driver gas. At high-enthalpy conditions, the LENS I facility produces free-stream flows that are characterized by chemical and thermal nonequilibrium. In the work, translational temperatures were compared to rotational temperatures and to CFD predictions at these conditions. Although the measurement uncertainty was not reported, the authors predict a temperature resolution of 50 K.

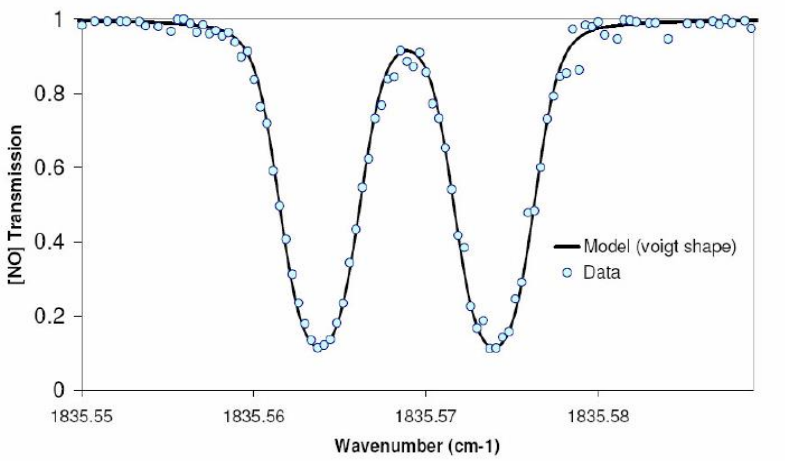

Figure 4.4. Absorption spectra measured in the CUBRC LENS I facility used to calculate translational temperature. Reproduced from Ref. [70] with permission of the authors.

4.4 Rotational Temperature

Rotational temperatures are typically measured by analyzing multiple absorption features that have line-strengths with different rotational temperature dependencies. Usually either multiple light sources are used to excite separate isolated transitions or a single light source is used to spectrally scan over adjacent absorption features. This technique is referred to as multi-line or ratio thermometry. The spectrally integrated absorbance that is measured experimentally is defined as:[71]

$$a_j = \int -\ln\left(\frac{I_\nu}{I_0}\right) d\nu \tag{4.19}$$

The subscript *j* refers to the absorption feature that is probed. Often a modified version of the spectral absorption coefficient is used:[72]

$$k_\nu = P\chi_i S Y_\nu \tag{4.20}$$

The subscript '12' in the line strength term *S* has been dropped for clarity. With this change, a modified version of the line-strength factor *S* [cm^{-2} atm^{-1}] is used:[73]

$$S(T_{rot}) = S(T_0)\frac{Q(T_0)}{Q(T_{rot})} e^{\frac{-hcE_{rot}}{k}\left(\frac{1}{T_0}-\frac{1}{T_{rot}}\right)} \left(\frac{1-e^{\frac{-hc\Delta E}{kT_{rot}}}}{1-e^{\frac{-hc\Delta E}{kT_0}}} \right) \tag{4.21}$$

where T_{rot}, T_0, Q, and E_{rot} are the rotational temperature, reference rotational temperature (296 K), the total internal partition function, and the total rotational energy of the molecular quantum state absorbing the light, respectively. ΔE is the difference in energy between the upper and lower states of the transition. It should be noted that the final term in the equation is due to stimulated emission, and is negligible at temperatures below approximately 2500 K and at wavelengths below 2.5 μm.[74]

If the light source is spectrally narrow, the integrated absorbance for each *j* transition can be simplified:

$$a_j = \int k_\nu L d\nu = \int P\chi_i L S_j Y_\nu d\nu = P\chi_i L S_j \int Y_\nu d\nu \tag{4.22}$$

If the entire transition can be resolved using a scanning technique, then the integrated absorbance becomes:

$$a_j = P\chi_i L S_j \ . \tag{4.23}$$

The ratio of two separate absorption features, denoted by subscripts *j*=1 and *j*=2, with different rotational energies, becomes:

$$\frac{a_1}{a_2} = \frac{S_1}{S_2} = \frac{S_1(T_0)}{S_2(T_0)} e^{-\frac{hc\Delta E_{rot}}{k}\left(\frac{1}{T_{rot}}-\frac{1}{T_0}\right)} \tag{4.24}$$

where ΔE_{rot} is the change in lower state rotational energy between the two absorption lines. Because many terms are cancelled in this ratio, it is possible to extract T_{rot}. Note that it is also possible to calculate this ratio based on peak absorbances instead of spectrally integrated values to extract temperature if the line-shape function is included. This assumes that the pressure shift and broadening coefficients are similar for both transitions.

Wehe *et al.*, performed rotational and translational temperature calculations from H_2O absorption measurements in the high-enthalpy (10 MJ/kg) Calspan 96-inch Hypersonic Shock Tunnel using a diode-laser sensor.[75] A probe, which housed the critical optical components, was placed directly into the core of the flow. In order to improve the signal-to-noise ratio, the hypersonic air flow was seeded with 6% water vapor. Absorption measurements, shown as solid data points in Figure 4.5, correspond to an H_2O absorption transition ($\nu_1+\nu_3$ band) near 1396 nm (λ_2) and 1400 nm (λ_1). A Gaussian fit, shown as a solid line in the figure, was applied to the experimental data to determine the spectrally integrated absorbances and Doppler broadening of

each transition. The ratio of the absorbances was used to compute the rotational temperature (Eq. 4.24)

The Doppler broadening was used to calculate the translational temperature (Eq. 4.18). The measurement uncertainty of the rotational temperature measurement was ± 13 K (± 2.3% of mean) whereas the measurement uncertainties of the translational temperatures based on the two absorption profiles (λ_1 and λ_2) were ± 15 K (± 2.7% of mean) and ± 35 K (± 6.4% of mean), respectively.

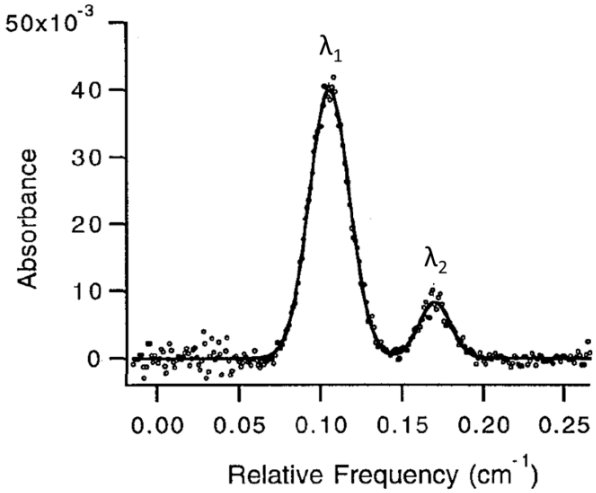

Figure 4.5. Absorption spectra and fit through H_2O transitions in Calspan 96-inch Hypersonic Shock Tunnel. Adapted from Ref. [75] with permission of the authors.

These high-resolution line-shapes were recorded every 125 μsec (8 kHz), allowing for time-resolved temperature measurements. Figure 4.6 shows the time-resolved rotational and translational temperatures extracted during the facility run time. Agreement indicates that the flow was in thermal equilibrium, which was expected based on equilibrium calculations reported in the work.

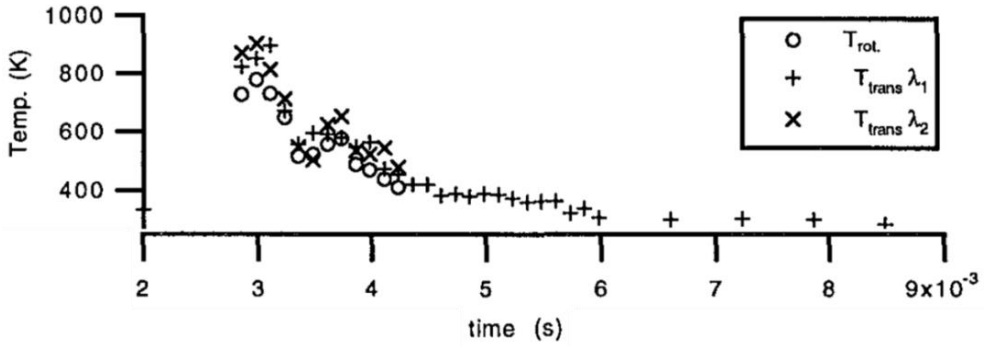

Figure 4.6. Translational and rotational temperature measurements in the Calspan 96-inch Hypersonic Shock Tunnel. Adapted from Ref. [75] with permission of the authors.

It can be difficult to accurately measure the line-strength due to problems in determining the zero absorbance intensity near the absorption feature wings, which is needed for baseline levels.[76] Using diode lasers, for example, the laser intensities can drift over time due to thermal, mechanical, and electronic effects. Liu *et al.* discuss how low signal levels, baseline-fitting errors, beam steering effects, and others can affect the estimation of the line-shapes.[76] To combat these problems, wavelength modulation spectroscopy (WMS) with second harmonic (2*f*) detection can be used. Detailed theory about WMS can be found in the literature.[77-80] Through the superposition of a modulation of frequency *f* onto the light source, the problem of excessive

DC noise that occurs at low absorbances can be greatly reduced. The absorbing medium converts some of the wavelength modulation into amplitude modulation of the laser intensity. The amplitude modulation occurs at the modulation frequency *f* and at its integral harmonics, *nf*. Then, by using phase-sensitive electronics, a selected harmonic can be isolated (e.g. $n = 2$). At sufficiently high frequencies *f*, excess noise from the light source (e.g. laser diode) can be reduced.

Goldstein *et al.* performed WMS-2*f* rotational temperature measurements using a tunable diode laser absorption sensor in the University of Virginia's supersonic combustion facility.[81] In this work, the facility was run with water injection to simulate vitiation effects and with hydrogen combustion (equivalence ratio of 0.33). Figure 4.7 shows sample experimental direct absorption (a) and WMS-2f/1f absorption (b) line-shapes of H_2O obtained at the combustor exit.

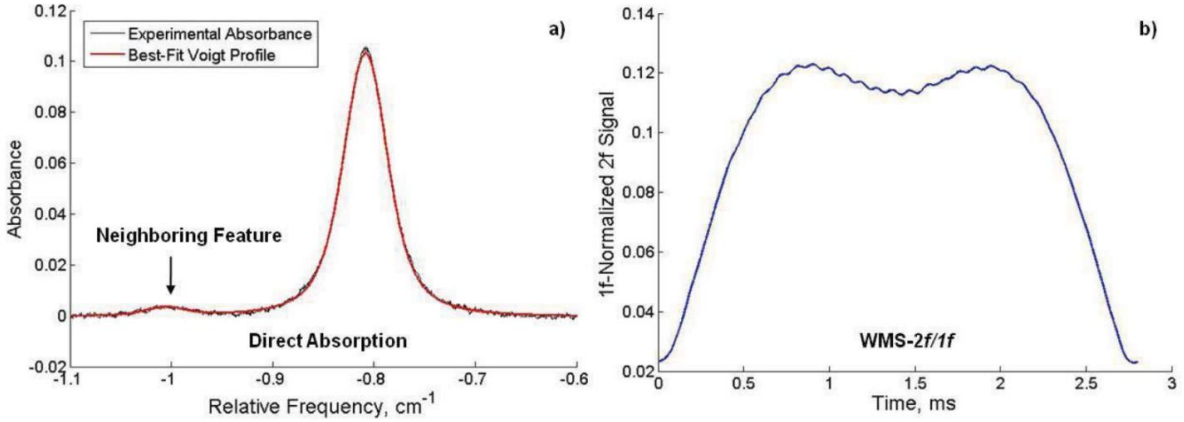

Figure 4.7. Direct absorption (a) vs WMS-2f/1f (b) in UVa supersonic combustion experiment. Reproduced from Ref. [81] with permission of the authors.

The two absorption features in Fig. 4.7(a) allow for the ratio thermometry technique to be used. However, the small magnitude of the neighboring feature results in a higher measurement uncertainty compared to the WMS-2*f* technique. Both techniques give temperatures that agree reasonably well with CFD predictions (Table 4.1). However, the direct absorption technique has consistently larger measurement uncertainties compared to the WMS technique. The authors discuss the discrepancy in temperatures observed in the H_2-air combustion case.

Table 4.1. Comparison of direct and WMS absorption calculations of rotational temperature. Reproduced from Ref. [81] with permission of the authors.

Operation Mode	Expected Value	DA	WMS
11% Steam (Combustor Entrance)	700-1000 K 11.4 ± 0.2 % H_2O	776 ± 10 K 10.9 ± 0.1% H_2O	742 ± 9 K 10.8 ± 0.1% H_2O
9% Steam (Exit Plane)	700-1000 K 9 ± 0.2 % H_2O	860 ± 30 K 9.1 ± 0.2% H_2O	831 ± 9 K 9.1 ± 0.1% H_2O
12% Steam (Exit Plane)	700-1000 K 12 ± 0.2 % H_2O	875 ± 50 K 12.1 ± 0.5% H_2O	850 ± 6 K 11.5 ± 0.1% H_2O
H_2-Air Combustion φ = 0.33 (Exit Plane)	1800-2200 K 13% H_2O	1802 ± 94 K 12.8 ± 0.5% H_2O	1765 ± 41 K 13.3 ± 0.3% H_2O

An alternative to wavelength modulation that has also been used with success in high-speed flows is ratiometric detection.[82,83] For this technique, the laser beam is split into a signal beam that propagates through the flowfield and a reference beam that does not. The photocurrents from the two beams are passed through a log-ratio amplifier, providing a direct measurement of the absorbance. If the photocurrents for the two beams are equal, the log-ratio detection removes the intensity modulation due to varying current on the beams, and the common-mode laser intensity noise, leaving only the absorption signal on the detector. The balanced variant of this technique includes an additional low-frequency feedback circuit that ensures that the photocurrents balance, zeroing the baseline of the measurement. This method, because it uses two beams rather than one, is optically more complex than wavelength modulation spectroscopy but electronically simpler, and provides similar absorbance detection limits. The output of the circuit is a signal that is directly proportional to the absorbance, making the analysis of the data straightforward.

Upschulte *et al.*[84] used the balanced ratiometric method to measure temperature, mole fraction and velocity in a supersonic combustion facility at the US Air Force Research Laboratory at Wright-Patterson Air Force base at Mach 2.1, using balanced ratiometric detection of water vapor near 1390 nm. The temperature and mole fraction measurements were made to within 100 K and around 0.3 % respectively, while beam steering adversely affected the velocity measurements. Griffiths and Houwing have also made measurements of water vapor temperature, mole fraction and velocity in a model scramjet engine at a flight Mach number of 10, in the Australian National University's T3 free-piston shock tunnel.[85] They used two time-multiplexed distributed feedback diode lasers and balanced ratiometric detection at scan rates of up to 20 kHz. Temperatures ranging from 600 K to 1800 K were measured in the turbulent, combusting environment of the scramjet engine.

4.5 Vibrational Temperature

Similar to multi-line thermometry for rotational temperature, vibrational temperatures can be measured by probing absorption features at different vibrational levels. Pan and Oka measured vibrational temperatures of ArH^+ ions in a glow discharge by separately measuring the integrated absorbance of transitions in two vibrational levels.[86] They compared the vibrational temperature

to the translational kinetic temperature measured using the Doppler width of the transition and quantified the thermal nonequilibrium in the plasma.

Brandt and Roth measured the absorption in the nonequilibrium flow behind a normal shock wave in a shock tube, in mixtures of CO and Ar, using a lead-salt IR diode tuned to absorption transitions lying between 2100 and 2200 cm^{-1}.[87] Once again, the vibrational temperature was compared with the translational temperature to determine the degree of nonequilibrium downstream of the shock wave. The measured translational and vibrational temperatures corresponded well to the values predicted by Landau-Teller theory.

4.6 Species Concentrations

Similar to the thermometry techniques, species concentrations can be determined through the analysis of the integrated absorbance. If the temperature can be determined from one of the thermometry techniques, then the concentration of absorbers C_i of species i can be determined from the integrated absorbance (Eq. 4.23) and ideal gas law:[88]

$$C_i = \frac{6.02\times10^{23} P\chi_i}{RT}\left(\frac{101325\cdot\mathrm{Pa}}{1\cdot\mathrm{atm}}\frac{1\cdot\mathrm{m}^3}{100^3\mathrm{cm}^3}\right) = \frac{6.1\times10^{22} a_j}{RTS_j L}\left[\frac{\mathrm{molecules}}{\mathrm{cm}^3}\right] \tag{4.25}$$

where R [$J\cdot mol^{-1}\cdot K^{-1}$] is the gas constant. Concentration can also be extracted from analysis of the broadening mechanisms, which have pressure and temperature dependencies, using a spectroscopic model that is fitted to the experimental data.[89]

Lin *et al.*, obtained CO concentration measurements using TDLAS in a Martian simulant gas (70% CO_2 and 30% N_2) that was accelerated in a shock tube.[88] The flow immediately behind the 6.31 km/s shock wave was in thermal nonequilibrium. Figure 4.8 shows a sample absorption spectra taken at 50 kHz near 2335.8 nm (4281.2 cm^{-1}) corresponding to the targeted CO transition. Even with excessive noise in the wings of the line-shape, a good Voigt fit was applied to the data, which is shown as the red solid line. The spectrally integrated absorbance was used to calculate the concentration. A room temperature cavity cell of CO was used to validate the technique. The authors report an average CO concentration of 7.46×10^{12} molecules/cm^3 behind the shock wave (Eq. 4.25). Errors in the Voigt fitting process resulted in a 1% uncertainty in the spectrally integrated absorbance values, which result in a 10% error in the CO concentration measurement.

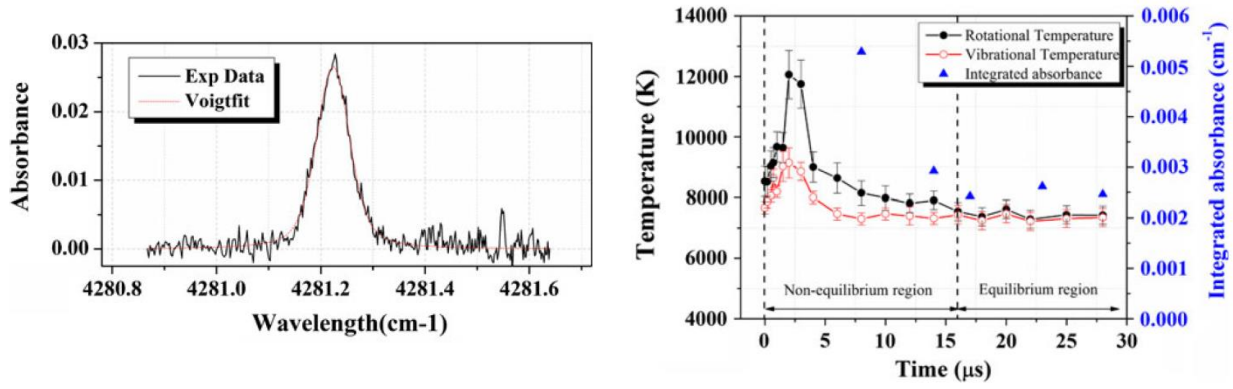

Figure 4.8. Sample absorption measurement with Voigt fit (left) and nonequilibrium temperature measurements (right). Reproduced from Ref. [88] with permission of the authors and Springer Science and Business Media.

4.7 Velocimetry

Doppler-shift based velocimetry is based on the analysis of the spectral shift that occurs in an absorption feature when gas molecules have a component of velocity that is in the same direction as the excitation source. From the absorbing molecule's frame of reference, the excitation source appears either red- or blue-shifted, depending on the molecule's velocity. As a result, the spectral frequency at which the light beam is absorbed is either blue- or red- shifted, respectively, from the laboratory frame of reference. If the Doppler shift can be measured experimentally, usually through a spectral scan, then the gas velocity can be calculated from the following relationship:

$$U = \frac{c\Delta\nu_{\text{DopplerShift}}}{\nu_{\text{LightSource}}} \tag{26}$$

The velocity can be determined by passing the laser beam through a duct at two different angles and measuring the absorption of a spectral feature for each of the two transmitted beams, as shown in Figure 4.9.[90] The Doppler shift in the peak of the absorption feature can be used to directly measure the velocity using Eq. 4.26.

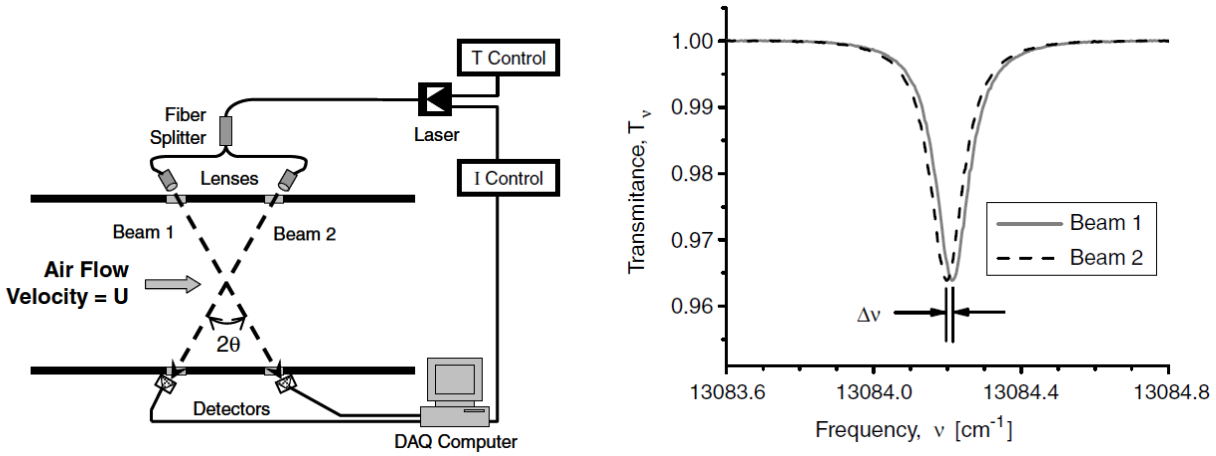

Figure 4.9. (a) Typical arrangement for diode laser absorption measurement, and (b) Doppler-shifted absorption features for the two beams. Reproduced from Ref. [33] with permission of the authors.

Infrared DLAS velocimetry measurements from CO, NO, and H_2O molecules were performed in the S4MA, F4, and DLR piston driven HEG facilities.[91] In that work, enthalpy conditions ranged from ~1 MJ/kg to 20 MJ/kg and test times ranged from 100 s to 1 ms. In addition to velocimetry, thermometry (translational), and concentration measurements were also performed. Figure 4.10 shows a sample NO absorption line-shape (R 3/2) near 5366 nm (1863.6 cm^{-1}) obtained in the DLR facility. The Doppler shift, which is used to calculate velocity (Eq. 4.26) is visible in the figure. The integrated absorbance and Doppler width used to calculate concentration and translational temperature are also shown in the figure.

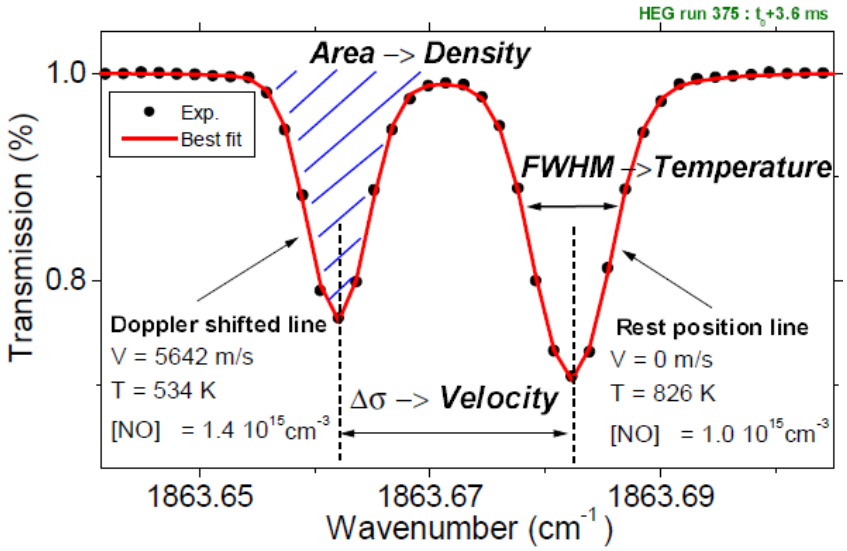

Figure 4.10. NO absorption line indicating how velocimetry, concentration, and translational temperature are calculated. Reproduced from Ref. [91] with permission of the authors.

Figure 4.11 shows DLAS velocimetry measurements in the F4 facility at an enthalpy condition of 15 MJ/kg. The velocimetry measurements are compared to CFD calculations using

both equilibrium and frozen assumptions. The velocimetry measurements show a closer agreement to the frozen calculations, indicating nonequilibrium.

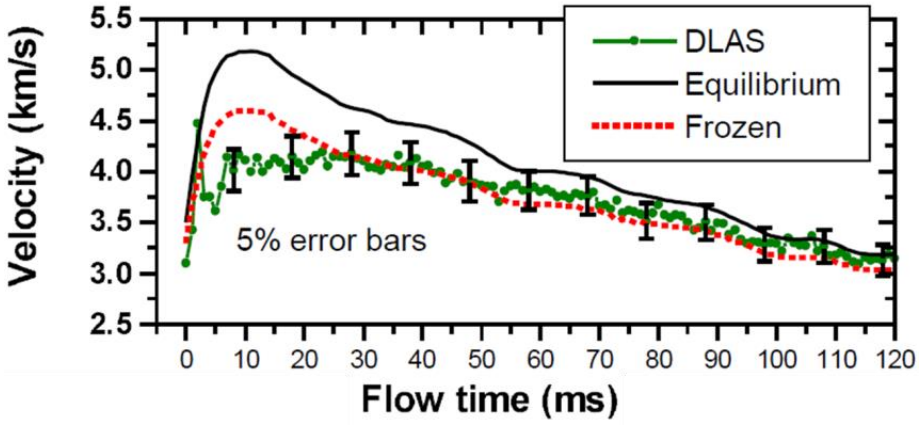

Figure 4.11. DLAS Doppler-shift based velocimetry measurements in the F4 facility (50 MPa; 15 MJ/kg). Reproduced from Ref. [91] with permission of the authors.

The first oxygen velocity measurement in a high-speed flow was made by Philippe and Hanson using wavelength modulation detection at scan rates of 10 kHz in the *A*-band of molecular oxygen.[92] Velocities were measured to within ±50 m/s, and agreed with theoretical estimates to within 5 %. More recently, velocity has been measured in a Mach 6 nozzle flow, using absorption in the same wavelength range, excited by a vertical cavity surface-emitting laser (VCSEL) emitting near 760 nm.[93] The laser was able to be current-scanned over four oxygen transitions. Velocities of around 950 m/s were measured with an uncertainty of ±40 m/s. These measurements were made by propagating the laser beam through two opposing retro-reflectors, imposing opposite Doppler shifts as the beam propagates in the two opposing directions. This method allows the velocity to be measured using a single laser beam.

4.8 Tomography

Absorption tomography involves using multiple absorption measurements, which are path averaged, to reconstruct a spatial distribution (e.g. two-dimensional) of the measured property. Hanson suggested that new low-power fiber-based absorption sensor arrays may bring tomographic imaging inside aeroengine and airframe models for hypersonic ground tests.[94] Tunable diode lasers have features that make them especially suitable for tomography. They can scan at very high rates, providing information at tens or hundreds of kHz, and the lasers are typically routed to and from the flowfield using optical fibers, simplifying the experimental setup. Technology from the telecommunications industry, such as fiber couplers and multiplexers, can be used to split the laser light into many channels and/or to combine many wavelengths into a single fiber, allowing multiple species to be probed with multiple colors along many paths through the flow. The light from the fibers is coupled into lenses, propagated across the flow and captured by lens-coupled multi-mode fibers, separated into wavelengths and

directed onto detectors. Thus, different species and spectral lines can be probed at different locations in a ducted flow, for example, allowing some spatially-resolved concentration and temperature information to be determined from the line-of-sight measurements.

Recent advancements in TDLAS tomography include systems that scan a single laser or multiple lasers spatially across the flow and from different directions to allow time averaged tomographic reconstruction of temperature and species concentrations in turbulent combusting flowfields[95] or a grid of fixed optical paths transmitting across the flow, allowing a low-resolution but time-resolved tomographic reconstruction of concentration and temperature.[96,97] Figure 4.12 (from Ref. 97) shows temperature and mole fraction maps obtained in a General Electric J85 gas turbine engine. Thirty individual laser beams—15 in the horizontal direction and 15 in the vertical direction, making a square mesh of 225 grid points—were used to probe the flow. The laser was rapidly scanned over multiple water vapor absorption lines near 1.35 μm with scans occurring at a rate of 50 kHz. While the smaller turbulent length (and time) scales of the flow are not resolved with this system, the large-scale spatial (and temporal) distribution of the temperature and mole fraction are resolved.

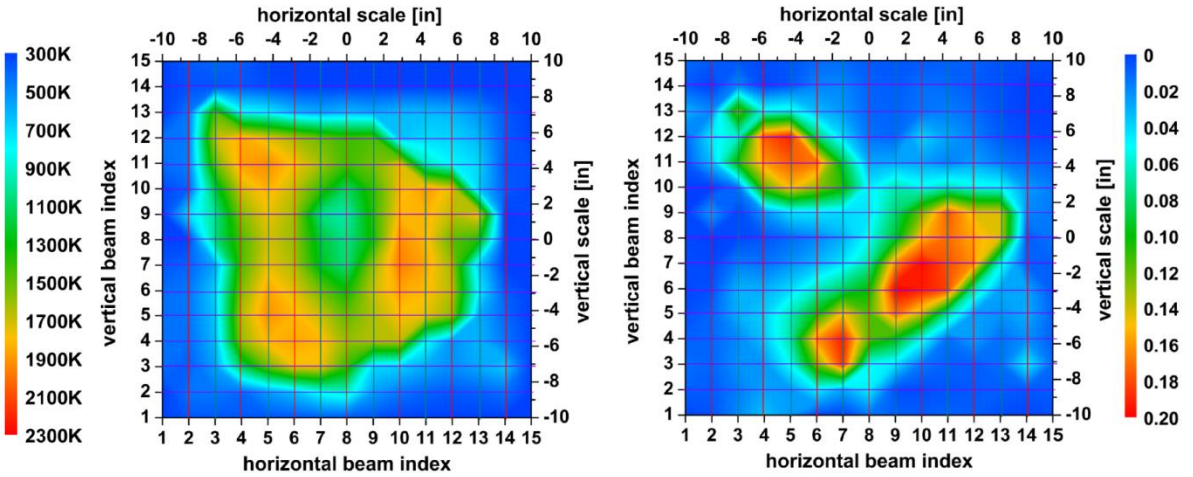

Figure 4.12. Temperature (left) and water vapor mole fraction (right) measured at the exit of a General Electric J85 engine, with 50 kHz diode laser tomography, adapted from Ref. [97]. The paper online has links to play animated movie clips of these data. Reprinted with permission of the authors and publisher.

4.9 Cavity Ring-down Spectroscopy (CRDS) and Other Cavity-enhanced Methods

Even when using sensitive detection techniques such as wavelength modulation or balanced ratiometric detection, it can be challenging to measure absorbances below 10^{-5}. As many nonequilibrium flows occur at low number densities, and many important absorbing species such as oxygen have only very weak accessible absorption features, it becomes necessary to investigate even more sensitive optical systems. CRDS is a highly sensitive technique that is based on increasing the amount of absorbance in a medium by increasing the effective path length (L) through the use of an optical system.[98] For example, if an absorbing medium is placed

between two highly reflective dielectric mirrors, then the energy of light resonating between the mirrors will decrease with each pass. A small amount of light passing through one of the mirrors is detected and monitored as a function of time. The "ring-down time" is the time it takes for the light to decrease to an intensity threshold. It is also equivalent to the mean time that any photon will survive between the two mirrors (i.e. within the cavity). Analysis of the absorption features using a CRDS setup can lead to quantitative measurements similar to those described for direct absorption (e.g. velocity, temperature, concentration). Though it is more sensitive than conventional absorption spectroscopy, it is more difficult to set up and to maintain alignment. Scherer *et al.* describes the history, development and application of CRDS to pulsed supersonic flows.[99] Similarly, Romanini *et al.*, performed CRDS measurements in NO_2 in a supersonic slit jet using a narrow line, continuous wave laser source.[100]

CRDS, due to its extreme sensitivity and the requirement of locking a laser to a cavity, can prove difficult to employ in the often-hostile environments where nonequilibrium aerospace measurements need to be made. Cavity-enhanced absorption (CEA) techniques have been developed that provide enhanced absorption using an optical cavity for enhancing the effective path length without requiring complex cavity-locking mechanisms. Two of the more commonly used CEA variants are cavity-enhanced absorption spectroscopy (CEAS)[101] and integrated cavity output spectroscopy (ICOS).[102,103] These methods measure the output signal of the cavity as the laser is scanned across a transition, rather than measuring the ring-down at a discrete set of frequencies. The noise immunity of CRDS is traded for a simpler and more robust arrangement, while still having enhanced sensitivity compared to TDLAS. All cavity-enhanced systems are sensitive to degradation of the quality of the cavity mirrors, which can be a consideration when used in harsh environments.

Most studies involving cavity-enhanced techniques in high-speed or nonequilibrium flows have concentrated on cold supersonic jets and plasmas. Bakowski *et al.*, have used CEAS to make measurements of translational and rotational temperatures of N_2 in an inductively coupled plasma, by exciting transitions from the $A^3\Sigma_u^+(v=0)$ band near 686 nm.[104] Fiedler *et al.*, have also expanded the CEAS method to the use of an incoherent broadband light source, and have performed measurements in a cold supersonic jet of azulene over a 40-nm wavelength range.[105]

4.10 Hardware Used for Absorption

The most common excitation sources used for absorption measurements in hypersonic nonequilibrium flows are semiconductor diode lasers that provide tunable light in the infrared.[106] Tunable diode lasers are relatively inexpensive compared to dye-pumped lasers and have narrow linewidths, which is necessary to resolve the absorption features in many common atoms and molecules. By adjusting the current through and the temperature of the diode, the wavelength can easily be controlled. Furthermore, the wavelength can be scanned at high frequencies (kHz), which is useful for some of the above-mentioned techniques. As a result of these advantages, the

diode laser is the preferred choice for absorption measurements although many other laser and non-laser sources are used.

4.11 Strengths and Weaknesses of Absorption Methods

There are many advantages of absorption methods over other optical diagnostics. In contrast to emission spectroscopy, absorption techniques can probe nonluminous flows, including both ground and excited states. Furthermore, optical setups for absorption experiments are simpler to set up and interpret compared to other techniques. Light sources, such as diode lasers, are relatively small and inexpensive compared to large pulsed laser systems needed for many techniques like PLIF and CARS. The frequency and scanning rate of diode lasers are also fast compared to Nd:YAG pumped dye lasers, allowing for high frequency temperature and concentration measurements to be obtained. Because of its simplicity, the absorption technique is also very robust. Also, unlike PLIF, there are no problems with quenching for absorption measurements, making them much simpler to analyze.

The main weaknesses of absorption spectroscopy are that measurements are path-averaged and are normally restricted to a point normal to the flow. Multiple absorption measurements in combination with tomographic reconstruction techniques can be used to invert the data and produce spatial distributions of the desired properties. In contrast, PLIF can easily obtain two-dimensional measurements along a thin sheet that interrogates the flow. If there is axial symmetry in the flow, then Abel transforms (described in the emission spectroscopy section) can be used to obtain radial distributions.

Because absorption is a path-averaged technique, uniform flow conditions across the path are desired for accurate measurements. Many practical flows have non-uniformities along the optical path, such as boundary layers, heat transfer at walls, and gas dynamic phenomena. These non-uniformities cause problems in the traditional signal analysis described above. In addition to the tomographic approaches described above, work reported in the literature describes methods to correct for these problems.[107,108] Sanders *et al.,* describes a method to deduce non-uniformity along the path by probing many absorption transitions.[71]

5. Laser-Induced Fluorescence (LIF)

Laser-induced fluorescence (LIF) uses a laser to probe individual species within the flowfield, providing information pertaining to both the thermodynamic (pressure, temperature, mole fraction) and fluid dynamic state (velocity) of the gas. The laser can be focused to a point for LIF measurements, formed into a thin sheet using a cylindrical and focusing lens in combination for planar LIF measurements (PLIF), or used to illuminate a volume for three-dimensional or stereoscopic imaging. Reviews of the laser-induced fluorescence measurement technique are available from Eckbreth[5] and others.[109,110] The measurement technique works by inducing a transition, usually of an electron, from a lower energy state (E_1) to an excited energy state (E_2) via stimulated absorption of one or more photons in the atomic or molecular species of

interest. In a two-level model assumption, the atom or molecule of interest in the E_2 state then returns to the E_1 state by transferring energy via spontaneous emission of a photon (fluorescence), or by transferring energy non-radiatively through a collision with another atom or molecule (collisional quenching).

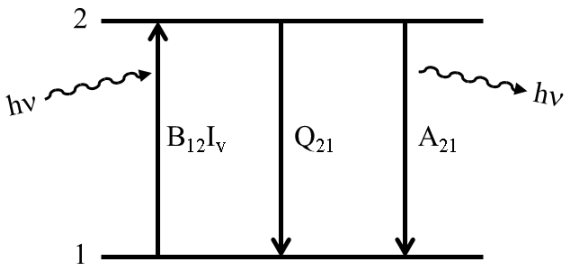

Figure 5.1. Two-level model of single-photon fluorescence.

For an atom, such as N or O, the energy required to induce an absorption transition of an electron to the E_2 state from the ground (E_1) state is equal to the energy difference between the atom with an electron occupying the excited electronic orbital and the atom's ground electronic orbital configuration, respectively. For molecules, such as N_2 and O_2, the energies of the E_2 and E_1 states include the energies associated with the vibrational and rotational motion of the molecule in addition to the energy associated with the molecule's electronic configuration. Figure 5.1 shows a generalized two-level model for fluorescence with the stimulated absorption transition induced by a single photon.

In Fig. 5.1, the rate at which the absorbing medium in the E_1 state transitions to the E_2 state is proportional to the product of the Einstein coefficient for stimulated absorption, B_{12}, and the laser's spectral irradiance (power per unit area per unit frequency), $I_\nu = IL_\nu$, where I is the irradiance (power per unit area) and L_ν is the laser spectral profile or laser line-shape (per unit of frequency).[5] The energy of the absorbed and emitted photons is the frequency, ν, multiplied by Planck's constant, h. The Einstein A_{21} and B_{12} coefficients describe the probabilities for emission and absorption,[111] respectively, while Q_{21} is the collisional quenching rate. For absorbing species, the line-shape function, Y_ν, describes the spectral width for a particular energy level.

As detailed in Section 4.2, the line-shape function combines effects from Gaussian-shaped Doppler broadening and Lorentzian-shaped homogeneous broadening mechanisms. The integral of the product of the absorption line-shape function, Y_ν, and the laser's spectral profile, L_ν, is defined by the overlap integral, $G = \int Y_\nu L_\nu d\nu$, and describes what portion of a particular absorption transition is affected by the incident laser radiation. The rate constant for stimulated absorption, W_{12}, which describes the rate at which species in E_1 transition to E_2 via absorption of a single photon[5,110] is then given by:

$$W_{12} = B_{12}IG \tag{5.1}$$

As the laser passes through a flowfield, it is absorbed at a rate corresponding to Eq. 5.1, inducing a transition between the E_1 and E_2 states. Consequently, as the laser continues to propagate through the flowfield, the irradiance is continually diminished as a result of the absorption process as described by the Beer-Lambert law (Eq. 4.3).

In certain circumstances, the energy separation between the E_1 and E_2 states for the species being examined with LIF is such that the frequency of a photon necessary to induce an absorption transition is far into the ultra-violet portion of the electro-magnetic spectrum. However, achieving frequencies far into the UV with conventional laser systems can be difficult.[111] Additionally, strong absorption of UV radiation by many materials and gases (including air) below approximately 200 nm limits the application of laser systems capable of producing such frequencies.[5] One solution is to use two-photon LIF techniques to probe species having absorption transitions in the deep UV. With a two-photon technique, the frequency (and therefore energy) of each photon is half that required by a single photon for the same transition. Figure 5.2 shows a generalized two-photon fluorescence energy model for two-photon LIF. For atomic species, such as N or O, spontaneous emission is often observed between E_2 and an intermediate energy state, E_3.

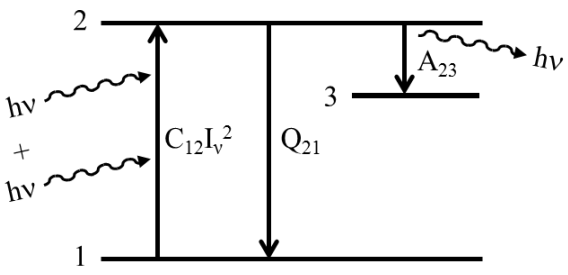

Figure 5.2. Three-level model of two-photon fluorescence.

For the two-photon LIF process in Fig. 5.2, the two-photon absorption cross-section results in a rate constant different from that in Eq. 5.1 and has the form:[5,111,112-115]

$$W_{12} = C_{12} I^2 G \tag{5.2}$$

where C_{12} relates to the two-photon absorption cross-section. Note that the dependence of the rate constant scales with the square of the incident laser irradiance, I. This behavior arises from the probability of observing the simultaneous arrival of two photons, which is the square of the probability for the arrival of a single photon.[111]

In both Figures 5.1 and 5.2, Q_{21} is the so called *quenching* rate constant. It describes the rate at which energy is transferred through non-radiative collisions between excited atoms or molecules in the E_2 state and atomic or molecular collision partners of species i. This rate constant is computed similarly to that in Ref. 5 as:

$$Q_{21} = N_T \textstyle\sum_i \chi_i \sigma_{s,i} v_{s,i} \tag{5.3}$$

where $N_T = P/k_B T$ is the total population of the excited state, χ_i is the mole fraction of quenching species i, $\sigma_{s,i}$ is the collision cross-section between the excited species, s, and quenching species, i, and $v_{s,i} = \sqrt{8k_B T_{trans}/\pi\mu_{s,i}}$ is the mean relative velocity[116,117] between the excited species and quenching species, with $\mu_{s,i}$ being their reduced mass and T_{trans} their translational temperature. The spontaneous emission coefficient, A, in Figures 5.1 and 5.2 is also

known as the Einstein *A* coefficient and describes the probability for spontaneous emission of a photon by an atom or molecule in the excited state.[111]

For the two-level model in Fig. 5.1, the rate of change of the populations N_1 and N_2, in the E_1 and E_2 states, respectively, can be obtained from relations similar to those presented in Ref. 5:

$$\frac{dN_1}{dt} = -\frac{dN_2}{dt} = -N_1 W_{12} + N_2(Q_{21} + A_{21}) \tag{5.4}$$

$$N_1 + N_2 = N_S = \chi_s f_B N_T \tag{5.5}$$

Equation 5.5 is a conservation law saying that the combined populations of the E_1 and E_2 states is equal to the initial population of the excitation species' E_1 state, N_S, which is in turn the product of the species mole fraction, χ_s, the total population, N_T, and the temperature-dependent Boltzmann fraction, f_B. Equation 5.4 assumes that the laser intensity is sufficiently weak such that stimulated emission (W_{21}) can be neglected.

The Boltzmann fraction, f_B, describes the ratio of the number of absorbers initially occupying E_1 relative to all possible energy states at a particular temperature, *T*, when a system is in thermodynamic equilibrium.[117] This term has a general form given by:[5,117,118]

$$f_B = \frac{g_j e^{-E_j/k_B T}}{\sum_j g_j e^{-E_j/k_B T}} \tag{5.6}$$

where g_j is the degeneracy of state *j*. Degeneracy refers to the number of quantized states that exist in a given energy level, E_j.[117] The summation in the denominator is termed the *partition function*, *Q* as described in Eq. 3.18.

More involved differential rate equations can be formulated for the two-photon method like those presented in Ref. 115. It should be noted that the models presented in Figures 5.1 and 5.2 neglect transitions from E_1 to E_2 resulting from collisions, with a rate constant of Q_{12}. This is usually a good assumption for large energy separations associated with the visible or UV transitions typically employed for LIF. Transitions from the E_2 and E_3 states resulting from pre-dissociation (Q_{pre}) and ionization (Q_{ion}), which are described in Refs. 5 and 110, have also been neglected.

5.1 Linear, Steady State Solution

If a continuous laser source is used to populate the E_2 state and detection of fluorescence occurs well after this source is turned on, then N_2 can be assumed to have reached its steady-state value. From this assumption, the left-hand-side of Eq. 5.4 is set to zero, resulting in two algebraic equations (Eqs. 5.4 and 5.5) for two unknowns (N_1 and N_2). The same assumption can be made to determine the population, N_2, achieved by a pulsed laser source if the time required to reach steady state is short compared to the duration of the pulse. This population is computed as:

$$N_2 = \frac{\chi_s f_B N_T W_{12}}{W_{12}+Q_{21}+A_{21}} \tag{5.7}$$

The product of this excited state population and the spontaneous emission rate constant is N_2A_{21} and represents the number of transitions per unit time and per unit volume. Integrating this constant value with respect to time gives the total number of transitions per unit volume during the detection period. Substituting Eq. 5.1 for W_{12}, and assuming that W_{12} is small compared to A_{21} and Q_{21} (which is valid for low-intensity excitation), a relation for the total number of photons collected via fluorescence by the detection device is:[110]

$$S_{LIF} = \chi_s f_B N_T B_{12} I G \Phi t_{det} V \frac{\Omega}{4\pi} \eta \tag{5.8}$$

where $\Phi = A_{21}/(Q_{21} + A_{21})$ is the fluorescence yield, t_{det} is the period of detection, V is the volume probed by the laser source, Ω is the solid angle over which detection occurs, and η is the detection efficiency. The fluorescence yield, Φ, describes the fraction of de-excitation transitions that occur via spontaneous emission (fluorescence) relative to all de-excitation transitions (i.e. spontaneous emission and collisional quenching, assuming pre-dissociation and ionization are negligible). Neglecting the constants in Eq. 5.8, a generalized form for the fluorescence signal similar to that presented in Refs. 110 and 119, including its thermodynamic (χ,P,T) dependencies and velocity dependence (arising from the Doppler effect), is:

$$S_{LIF} \propto \chi_s N_T f_B(T) B_{12} I G(\chi_s, P, T, U) \Phi(\chi_s, \chi_i, P, T) t_{det} \tag{5.9}$$

5.2 Non-Steady State Solution

For a pulsed laser source, if N_2 is changing during the period of detection, then the entirety of Eq. 5.4 must be solved to obtain the time-dependent population, $N_2(t)$. Similarly, if the duration of the laser pulse is of the same order of magnitude as the time required to reach steady state, then the population at the end of the laser pulse, $N_2(t_{laser})$, can be obtained by solving Eq. 5.4. By assuming the laser intensity behaves as a Heaviside step function in time, the population $N_2(t)$, existing during laser excitation can be calculated by substituting the relation for N_1 from Eq. 5.5 into Eq. 5.4 and integrating with respect to time:[110]

$$N_2(t) = \chi_s f_B N_T \frac{W_{12}}{r} \cdot (1 - e^{-rt}),\ 0 < t \leq t_{laser} \tag{5.10}$$

where $r = W_{12} + Q_{21} + A_{21}$. The inverse of this value, r^{-1}, is the characteristic time needed to achieve steady state. This solution assumes an initial condition which typically specifies the initial excited state population to be zero ($N_2(0) = 0$).

When the laser source is turned off, the only pathways to return to the ground state from the excited state are assumed to be through either spontaneous emission or collisional quenching. Therefore, for the period following laser excitation, the first term on the right-hand-side of Eq.

5.4 is zero. This modified version of Eq. 5.4 is then used to determine the excited-state population for the period after laser excitation by integrating with respect to time:[110]

$$N_2(t) = \chi_s f_B N_T \frac{W_{12}}{r} \cdot (1 - e^{-rt_{laser}}) \cdot e^{-(t-t_{laser})/\tau_{LIF}},\ t > t_{laser} \tag{5.11}$$

This solution assumes that the laser intensity is turned off instantaneously, with an initial condition given by Eq. 5.10, evaluated at $t = t_{laser}$. This solution shows that the population in the excited state decreases exponentially in time after the laser pulse.

The term $\tau_{LIF} = (Q_{21} + A_{21})^{-1}$ in Eq. 5.11 is referred to as the fluorescence lifetime and describes the rate at which the population in a particular excited state transitions to a lower state. As with the derivation of Eq. 5.8, the total number of photons collected via fluorescence over the detection period is determined by multiplying Eqs. 5.10 and 5.11 by the spontaneous emission rate Einstein coefficient A_{21}, accounting for the collection volume and detection system, and integrating with respect to time:[110]

$$S_{LIF} = \chi_s f_B N_T \Phi B_{12} I G t_{laser} \left\{ \left[1 - \frac{1-e^{-rt_{laser}}}{rt_{laser}} \right] + \left[\frac{\left(1-e^{-rt_{laser}}\right)}{t_{laser}/\tau_{LIF}} \right] \right\} V \frac{\Omega}{4\pi} \eta \tag{5.12}$$

Like Eq. 5.8, this solution assumes that W_{12} is small compared to A_{21} and Q_{21}. However, if the laser irradiance, I, is sufficiently large such that W_{12} and W_{21} are of the same order of magnitude as Q_{21} and A_{21}, then both must be included in the solution. This gives $r = W_{12} + W_{21} + Q_{21} + A_{21}$ during laser excitation. By defining the irradiance at which the fluorescence signal saturates as[5,110] $I_{sat} = (Q_{21} + A_{21})/(B_{12} + B_{21})$ and rearranging r such that $r = \tau_{LIF}^{-1}[I/I_{sat} + 1]$, a more detailed formulation for the fluorescence signal, including effects from laser saturation, is given as:[110]

$$S_{LIF} = \chi_s f_B N_T \Phi B_{12} \frac{I}{1+I/I_{sat}} G t_{laser} \left\{ 1 + \frac{1-e^{-rt_{laser}}}{rt_{laser}} \left(\frac{I}{I_{sat}} \right) \right\} V \frac{\Omega}{4\pi} \eta \tag{5.13}$$

When $I \ll I_{sat}$, Eq. 5.13 simplifies to a form similar to that of Eq. 5.10.

5.3 Multi-Level Fluorescence Modeling

In the preceding discussion, a simplified two-level model of fluorescence was put forth, which provides for an understanding of the most basic physical mechanisms and energy transfer processes involved. This basic description allows for the development of a general analytic relation between the fluorescence signal and these mechanisms and processes. However, such a simple description does not account for rotational or vibrational energy transfer occurring between the absorbing species and the surrounding gas mixture. Since each electronic energy level depicted in Fig. 5.1 can have vibrational and rotational fine structure for molecular species, such energy transfer processes result in a redistribution of the populations to various vibrational and rotational states. To account for these processes, analytical models including multiple energy

states and a system of population rate equations are used. Discussion of such modeling aspects can be found in Refs. 5, 109 and 110.

5.4 Translational Temperature

Translational temperature resulting from the random thermal motion of the absorbing species can be determined by measuring the Doppler-broadened width of the absorption line-shape function of Eq. 4.14. If the temperature, pressure, and mole fractions at a particular location are assumed to be constant, then the Boltzmann fraction and fluorescence yield in Eq. 5.9 at that location are also assumed to be constant. If these assumptions are valid, and if the laser line-shape function is known, then the fluorescence signal will be proportional to the overlap integral at a particular frequency. By scanning the laser's spectral frequency across a particular transition, the absorption line-shape function can be obtained.

Once the absorption line-shape is obtained, the contribution of homogeneous broadening mechanisms to the line-shape must be determined to allow for calculation of the Doppler-broadened line width. Homogeneous broadening can include components from Van der Waals broadening and Stark broadening effects, [120] in addition to collisional pressure-broadening effects. In many cases, the Van der Waals and Stark effects can be ignored, resulting in homogeneous broadening from pressure alone. If the pressure is known, then the component of the line-shape due to homogeneous broadening can be determined. Alternately, if the pressure is sufficiently low, then collisional pressure broadening can be ignored. A fitting algorithm can then be used to determine the contribution of Doppler broadening to the line-shape. This allows for a more accurate temperature calculation as only one parameter, $\Delta\nu_D$, must be iterated upon to fit the line-shape. The translational temperature, T_{trans}, of the absorbing species can then be obtained by modifying Eq. 5.2:

$$T_{trans} = \frac{m}{8\ln(2)k_B}\left(\frac{c\Delta\nu_D}{\nu_0}\right)^2 \tag{5.14}$$

Both single-photon[120- 122] and two-photon [123 - 127] methods have been used to measure translational temperature. The requirement of scanning a laser's frequency to resolve the Doppler-broadened line-shape can limit the time resolution of the temperature measurement such that only average translation temperatures can be obtained.

Figure 5.3 shows LIF data (dotted line, upper plot) from Ref. 120 obtained by performing a frequency scan with a semiconductor laser source over an argon metastable transition centered at 810.4 nm. Each frequency scan over the absorption transition took 500 seconds to complete. In the experiment, argon plasma was generated using an inductively-coupled plasma torch. The translation temperature, T, and electron number density, n_e, were obtained by fitting the Voigt line-shape function, which accounted for both Doppler-broadening and several collisional broadening mechanisms, to the experimental LIF data (solid line, upper plot). The lower plot in Fig. 5.3 shows the residual: the difference between the experimental LIF data and the fitted line-shape. An analysis of one of the scans in Ref. 120 gave T_{trans} = 6800±690 K, resulting in a ~10% measurement uncertainty.

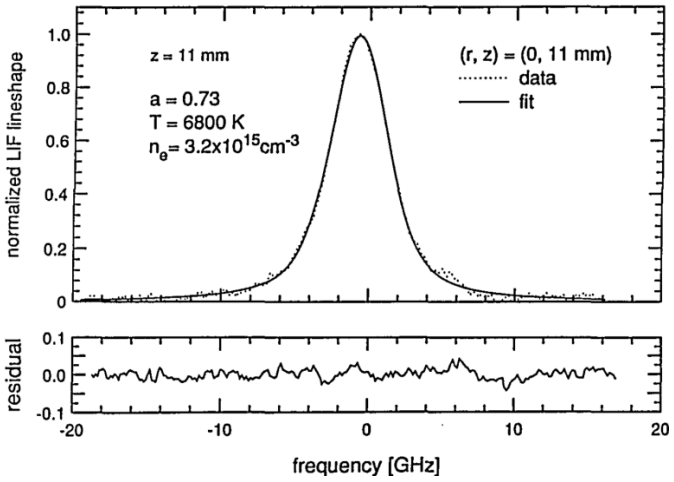

Figure 5.3. Experimental LIF data measured (dotted line, upper plot) in an Argon plasma and corresponding fit of Voigt line-shape (solid line, upper plot) to the experimental data (upper plot) and difference between experimental data and fit (lower plot). Image reprinted from Ref. 120 with permission of the authors and the publisher.

5.5 Rotational Temperature

For molecules, the rotational temperature, T_{rot}, can be obtained by exciting two absorption transitions and relating the signal intensities observed from each transition to the rotational temperature through modification of Eq. 5.9. This method was demonstrated in Ref. 128 using a two-photon excitation method to measure rotational temperature at a point in a cold (~300 K) turbulent flow. For each rotational transition, the population fraction, f_B, is dependent on the rotational energy, F_J, rotational quantum number, J, and rotational temperature, T_{rot}, of the absorbing species. This assumes that excitation occurs in the same vibrational state, v, such that the vibrational energy, G_v, is constant for each probed rotational transition. If χ_s, G, Φ, and t_{det} are assumed to be independent of the rotational state of the absorbing species, then the ratio, R, of fluorescence signals can be simplified to the following relation, similar to that in Refs. 110, 129-132:

$$\frac{S_{LIF,i}}{S_{LIF,j}} = R = C\,\frac{B_{12,i}E_i}{B_{12,j}E_j}\,\frac{(2J_i+1)\exp\left[-F_{J,i}/k_BT_{rot}\right]}{(2J_j+1)\exp\left[-F_{J,j}/k_BT_{rot}\right]} \tag{5.15}$$

where the subscripts i and j refer to the particular excited absorption transition, E is the laser energy such that $E = at_{laser}I$, a is the beam cross-sectional area, t_{laser} is the temporal pulse

width of the laser, and C is a constant which includes all terms that are independent of the rotational state of the absorbing species. Solving for T_{rot} in Eq. 5.15 yields:

$$T_{rot} = \frac{-\Delta E_{rot}}{k_B \ln\left[CR\frac{B_{12,j}E_j(2J_j+1)}{B_{12,i}E_i(2J_i+1)}\right]} \tag{5.16}$$

Here, $\Delta E_{rot} = (F_{J,i} - F_{J,j})$, and is the difference in energy between the probed rotational levels. To minimize the uncertainty associated with the measured rotational temperature, δT_{rot}, a propagation-of-error analysis can be performed on Eq. 5.15 by computing the derivative of the signal ratio, R, with respect to T_{rot}:[130,133]

$$\frac{\delta T_{rot}}{T_{rot}} = \frac{k_B T_{rot}}{\Delta E_{rot}} \frac{\delta R}{R} \tag{5.17}$$

This analysis suggests that by increasing ΔE_{rot}, and thereby probing two widely separated rotational energy levels, the uncertainty in T_{rot} can be proportionally decreased for a given error in R.[130]

Figure 5.4 shows a mean rotational temperature map of nitric oxide measured in the wake of a 6.35-mm-thick flat plate in a Mach 3 turbulent flow, taken from Ref. 133. The map was obtained by averaging a series of images taken for excitation from rotational levels J = 8.5 and J = 10.5, computing the ratio of the two averaged images, and using a relation similar to that in Eq. 5.16 to compute T_{rot}. In this experiment, it was shown that the turbulent nature of the flowfield required excitation of two relatively closely spaced rotational levels (J = 8.5 and 10.5). This requirement arose from the nonlinear relation between R and T_{rot} in Eq. 5.16, which can be heavily influenced by flowfield turbulence.

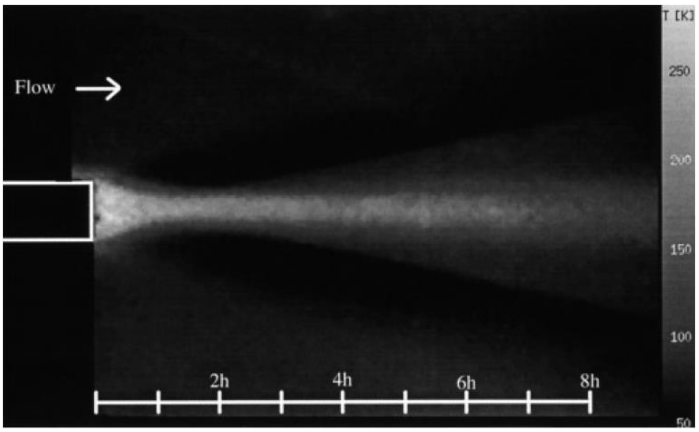

Figure 5.4. Rotational temperature map obtained in the supersonic wake of a flat plate using two-line rotational thermometry. Image reprinted from Ref. 133 with permission from the authors and Springer Science and Business Media.

Figure 5.4 shows a time-averaged temperature measurement obtained using a single laser, which probed the two transitions in separate wind tunnel runs. To obtain instantaneous temperature measurements in a plane using this method, a two-laser, two-camera system can be used, as in Refs. 129-131. In Ref. 130, instantaneous two-line temperature imaging of OH in a shock tube at a nominal pressure of 40.53 kPa and temperature range of 1500-2950 K resulted in temperature measurements with errors of ~20%-25%.

Multi-rotational-line temperature methods also exist and can potentially provide relatively higher sensitivity and dynamic range T_{rot} measurements, particularly at lower temperatures where rotational energy levels are closely spaced.[134] Such methods are appropriate when large variations in T_{rot} are expected, requiring probing of several rotational levels. The rotational temperature is computed by exciting multiple rotational lines and measuring the signal. This measured fluorescence signal, together with the measured laser energy are then substituted into the following relation:[132]

$$\ln\left[\frac{S_{LIF,i}}{B_{12,i}E_i(2J_i+1)}\right] \tag{5.18}$$

A plot of this logarithmic term versus $F_{J,i}$, known as a Boltzmann plot, yields a linear trend with a slope of $-k_B T_{rot}$. Refs. 134-137 used this method to characterize rotational temperatures in arc jet flows. An alternative multi-line approach used in Ref. 138 for measurements in a flame involved fitting a simulated rotational spectrum to experimental data to obtain T_{rot}.

5.6 Vibrational Temperature

The vibrational temperature, T_{vib}, can be measured using an approach similar to that used for rotational temperature. For T_{vib} measurements, a two-line approach can be used. Such an approach is presented in Ref. 139, in which the same rotational levels, $J_i = J_j$, are probed in two different vibrational levels, $v_i \neq v_j$, resulting in nearly constant rotational energies, F_J, but different vibrational energies, G_v. Assuming χ_s, G, Φ, and t_{det} to be independent of the rotational and vibrational levels, the ratio of fluorescence signals, R, can be used to measure vibrational temperature, T_{vib}, in a way analogous to that in Eqs. 5.15 and 5.16.

As with rotational temperature measurements, a multi-vibrational-line temperature measurement method can also be used to infer T_{vib} by modifying the logarithmic term from Eq. 5.18:[132]

$$\ln\left[\frac{S_{LIF,i}}{B_{12,i}E_i(2J_i+1)\exp\left[-F_{J,i}/k_B T_{rot}\right]}\right] \tag{5.19}$$

If the rotational level, J_i, is fixed and the rotational energy, $F_{J,i}$, is kept approximately constant, then the vibrational temperature can be computed independently of rotational temperature.[132] This is done by generating a Boltzmann plot of vibrational energy, $G_{v,i}$, versus this logarithmic term, resulting in a linear relation with a slope equivalent to $-1/(k_B T_{vib})$.

Figure 5.5(a), taken from Ref. 132, shows a Boltzmann plot generated using a relation like that in Eq. 5.19 to infer vibrational temperature. The image data in the experiment was used to measure T_{vib} at a point downstream of a free-piston shock tunnel nozzle on the centerline of the flow. In this experiment, three absorption transitions were selected that had nearly constant rotational energies, F_J, but differing vibrational energies, G_v. In Fig. 5(b), also taken from Ref.

132, the vibrational temperature of NO was observed to be constant with distance downstream of the nozzle, even though the nozzle was conical and the rotational temperature was shown to be decreasing with distance downstream, as the flow expanded. A simple computational model (shown in Fig. 5(b)) was not able to accurately predict the measured vibrational temperature.[132] As shown in Fig. 5(b), T_{vib} = 785±30 K, giving an uncertainty of ~4%.

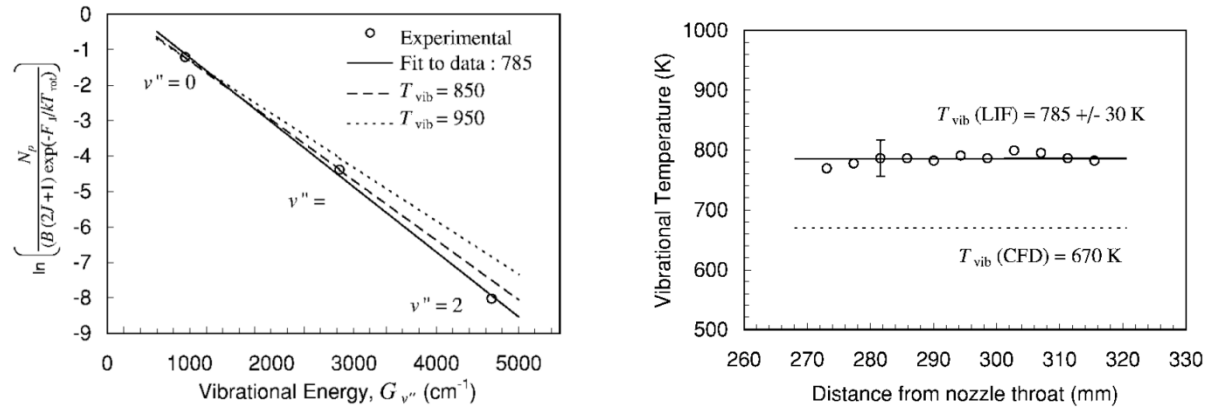

(a) (b)

Figure 5.5. Vibrational temperature measurement obtained by probing multiple vibrational levels and generating (a) a Boltzmann plot and (b) vibrational temperatures plotted as a function of distance downstream. Images taken from Ref. 132 with permission of the authors.

5.7 Species Concentration

Returning to the simplified Eq. 5.8, it is possible to quantify the number density, $\chi_s N_T$, using LIF. However, several factors complicate the interpretation of a LIF signal and its relation to concentration. For instance, Q_{21} in Eq. 5.3 depends on the concentration and temperature of the absorbing species and all other constituent species in the probed mixture. If the temperature of the mixture were unknown, then a separate measurement of temperature would be required to determine both Q_{21} and the temperature-dependent Boltzmann fraction. The measurement system also requires an appropriate absolute intensity calibration to a known reference, which can be further complicated by the collection optics and filters used in such a measurement. The response of the detection system as a function of S_{LIF} intensity and spectral frequency must also be well understood. The following discussion highlights some of the methods that have been used to provide concentration measurements that address some of these issues.

5.7.1 Non-quantitative flow visualization

A relatively simple approach to obtaining a qualitative visualization of species concentration is to use laser-induced fluorescence to visualize the spatial distribution of the absorbing species. To first-order, the fluorescence signal in Eq. 5.9 is proportional to the relative species concentration, $\chi_s N_T$, assuming all other terms are constant. In hypersonic nonequilibrium test facilities, the formation of reactive species at the high enthalpies required to simulate true flight conditions can influence the gas dynamics under study. For example, arc-heated facilities are often used to simulate true flight enthalpy conditions by depositing significant energy into a test gas and then expanding that gas to hypersonic Mach numbers. This process can result in a non-uniform species distribution resulting from the unsteady nature of the electrical arc.

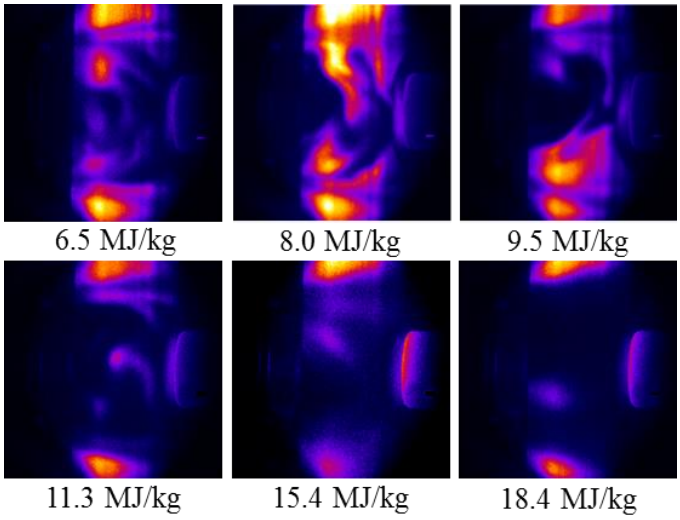

Figure 5.6. Instantaneous nitric oxide planar LIF flow visualization images in false color acquired in the Hypersonic Materials Environmental Test System (HyMETS) arc-heated facility at NASA Langley Research Center. Flow is from left to right. Images taken from Ref. 140 with permission of authors.

Figure 5.6 from Ref. 140 shows instantaneous nitric oxide (NO) planar LIF images in false color acquired in the Hypersonic Materials Environmental Test System (HyMETS) arc-heated facility at the NASA Langley Research Center for a flow simulating earth's atmosphere at several enthalpy conditions. The flow in this figure is from left to right. The object on the right-hand edge of the field of view is a 25 mm diameter silicon carbide tipped probe aligned with the axis of symmetry of the facility nozzle. For the lowest enthalpy condition shown (6.5 MJ/kg), the spatial distribution of NO within the core of the nozzle flow is irregular, suggesting that the energy deposition by the arc upstream of the nozzle is non-uniform. As the flow enthalpy increases to 18.4 MJ/kg, the distribution of NO remains irregular and the total production of NO appears to decrease.

Other examples of such LIF-based flow visualization experiments are provided in Ref. 141. The interpretation of such flow visualization images and their relation to quantitative species concentration measurement is complicated. The remaining terms in Eq. 5.9, such as the quenching rate constant, often vary significantly in high-speed nonequilibrium flows and can be difficult to determine. The sections that follow detail approaches for quantitative measurements of concentration which address such complicating factors.

5.7.2 Saturated LIF

To avoid the complications associated with an unknown quenching rate constant, a relatively high laser irradiance where $I \gg I_{sat}$ can be used to probe the absorbing species.[5] In this instance, the stimulated absorption and emission rates dominate both collisional quenching and spontaneous emission rates; that is, $(W_{12} + W_{21}) \gg (Q_{21} + A_{21})$. The result of this leads to a modified form of Eq. 5.8 where stimulated emission is included and the fluorescence signal is of a form similar to that in Ref. 5:

$$S_{LIF} = \chi_s f_B N_T A_{21} \frac{B_{12}}{B_{12}+B_{21}} t_{det} V \frac{\Omega}{4\pi} \eta \tag{5.20}$$

If A_{21}, B_{12}, and B_{21} are known, then this method can be used to measure concentration if the remaining terms, such as f_B, can be determined. In practice, it is difficult to achieve $I \gg I_{sat}$ because high powered pulsed laser beams are typically Gaussian, both spatially and temporally, so much of the acquired signal can originate from the lower intensity edges of the Gaussian beam, which excite the fluorescence linearly.[5] Further discussion of this method is found in Refs. 5 and 109.

5.7.3 Pre-dissociation LIF

Pre-dissociative fluorescence involves inducing a transition to a level in the excited state, which can then couple to a dissociative state, resulting in dissociation of the molecule into smaller molecules or atoms. Pre-dissociative fluorescence concentration measurements are similar to saturated fluorescence measurements in that the dependence on Q_{21} in Eq. 5.8 can be removed, in this case by exciting the absorbing species to a pre-dissociative state where the pre-dissociation rate, Q_{pre}, is faster than both Q_{21} and A_{21}.[5] A discussion of this mechanism can be found in Refs. 142 and 143 and a general discussion of the method can be found in Refs. 5 and 109. An application of the pre-dissociative technique was presented in Ref. 144 to measure time-averaged OH concentrations in a supersonic hydrogen-air turbulent combusting flow. Concentrations as high as 5.4×10^{16} cm^{-3} with uncertainties of 21% or less were reported.[144]

5.7.4 Short-Pulse LIF

There are two methods of using short laser pulses to quantitatively determine concentration. The first probes the species of interest with a laser pulse having a duration much shorter than the time between collisions with other species. With this method, the concentration can be determined by relating the measured exponential fluorescence decay behavior to the initial signal magnitude during the short-pulse excitation period. While this decay is a function of both A_{21} and Q_{21}, extrapolation of the exponential behavior to initial excitation provides an inferred peak intensity magnitude, which is assumed to be independent of collisional quenching effects.[109] This independence is assumed since a sufficient number of collisions, required to transfer energy non-radiatively from the excited state, would not yet have occurred. A discussion of this method can

be found in Ref. 109. Reference 145 uses a form of this short-pulse method for OH concentration measurements in a turbulent flame.

A second method for measuring concentration involves using a laser pulse that is shorter than or comparable to the fluorescence lifetime but not shorter than the collisional timescales described in Ref. 5. In this approach, the fluorescence lifetime is measured directly, usually using a photomultiplier tube. This short-pulse LIF method can also be used to determine spontaneous emission[146] and collisional quenching[147,148] rate constants when the thermodynamic conditions of the probed mixture are known. Even for unknown conditions, measurement of the fluorescence lifetime allows for the quenching rate to be determined and accounted for. Refs. 149 and 150 use a two-photon LIF technique in which fluorescence lifetime measurements are used to correct for collisional quenching effects in a similar manner. Figure 5.7(a), taken from Ref. 149, shows spectral scans of atomic nitrogen in the NASA Ames Aerodynamic Heating Facility arc jet flow (red data) and laboratory flow reactor (green data). Fluorescence measurements from the flow reactor and a krypton reference cell were used for intensity calibration in order to provide absolute atomic nitrogen number densities. The fluorescence lifetimes observed in the arc jet and flow reactor were used to correct for collisional quenching effects. Figure 5.7(b), also taken from Ref. 149, shows radial atomic nitrogen number density measurements for two air/argon arc jet runs taken 35.6 cm downstream of the nozzle exit. The reported uncertainty in number density was ~12%.[149]

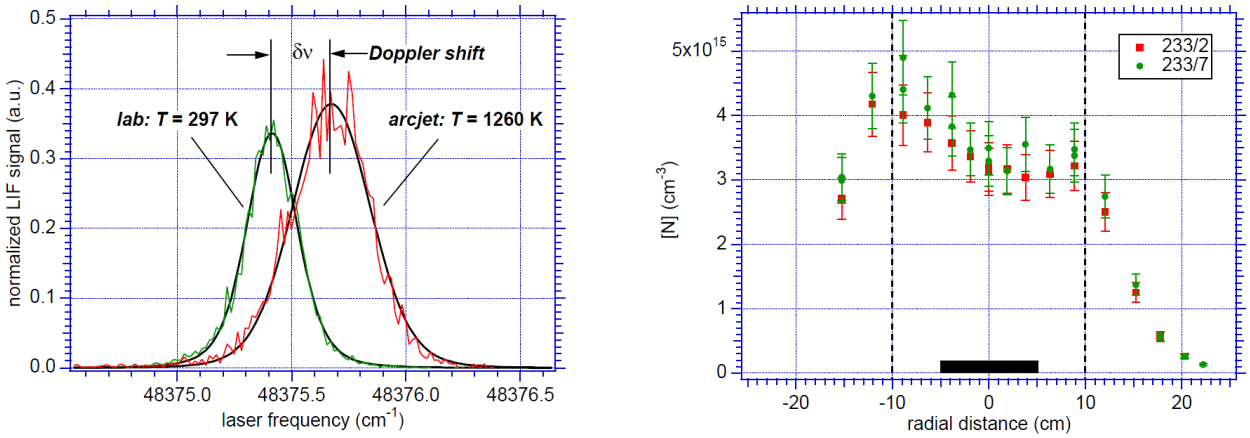

Figure 5.7. (a) Spectral scans of atomic nitrogen in the NASA Ames Aerodynamic Heating Facility arc jet flow and in a laboratory flow reactor and (b) measured number densities spanning the radial direction of the arc jet 35.6 cm downstream of the nozzle exit. Image taken from Ref. 149 with permission of the authors.

A similar approach is being developed for mole fraction measurements in hypersonic turbulent boundary layers using naphthalene PLIF.[151,152] One benefit of using naphthalene is that it sublimates at slightly elevated temperatures (with respect to room temperature), allowing for

the study of scalar transport effects in transitional boundary layers, turbulent boundary layers, and ablating surfaces.

5.7.5 Bi-Directional Beam LIF

If two overlapping, counter-propagating beams are tuned to the same transition, the ratio of fluorescence signals results in the cancellation of all terms in Eq. 5.9 at a point in the flow, with the exception of the spatially dependent laser irradiance. Thus, the spatially varying ratio of fluorescence signals can be equated to the spatially varying ratio of irradiances of the respective beams. The Beer-Lambert law of Eq. 4.3 can then be used to relate irradiance, and therefore fluorescence signals, to number density via the relation:[58]

$$k_s(\nu) = N_s \varphi_s(\nu) \qquad (5.21)$$

where $\varphi_s(\nu)$ is the transition cross-section of the absorbing species, describing the absorbing species' interaction with the incident irradiance on a per atom or molecule basis.[111] Combining Eq. 5.21 with Eq. 4.4 allows for a relation between the natural logarithm of the signal ratio and the absorbing species number density to be made:[153]

$$N_s(x) = \frac{1}{2\varphi_{s,0}} \frac{d}{dx} \ln\left[\frac{S_{LIF,1}(x)}{S_{LIF,2}(x)}\right] \qquad (5.22)$$

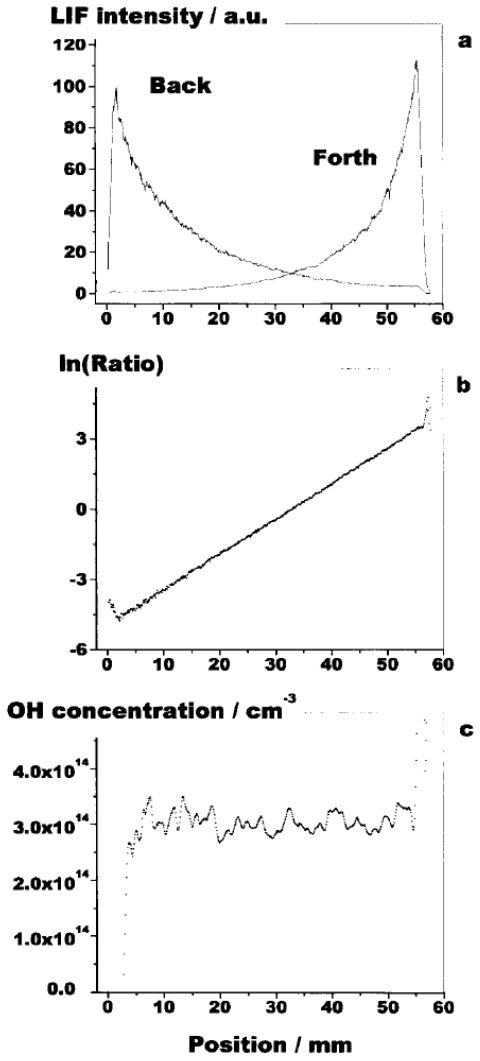

Figure 5.8. Graphical depiction of methodology used to measure concentration using bi-directional beam LIF. Top plot shows spatially varying fluorescence signals, middle plot shows natural logarithm of ratio of these signals, and bottom plot shows OH concentration calculated using Eq. 5.22. Image reprinted from Ref. 153 with permission of the authors and Springer Science and Business Media.

where $S_{LIF,1}(x)$ and $S_{LIF,2}(x)$ are the spatially varying fluorescence signal intensities of the forward- and backward-propagating beams, respectively. In Eq. 5.22, $\varphi_{s,0}$ is the peak transition cross-section, with $\varphi_{s,0} = \varphi_s(\nu_0)$.[111]

This concentration measurement technique was first demonstrated in Ref. 153. The technique only requires that a value for $\varphi_{s,0}$ be known in order to make an absolute concentration measurement of N_s.[153] For total absolute concentration, however, f_B must either be assumed or

measured, as from Eq. 5.5, $N_s = \chi_s f_B N_T$. Figure 5.8, taken from Ref. 153, graphically depicts the process of obtaining a concentration of OH in a methane-air flame. In the top plot, the fluorescence intensities are plotted versus position across the flame. The middle plot shows the natural logarithm of the ratio of these two signals with position and the bottom plot shows the calculated absolute OH concentration using Eq. 5.22. Measurements of OH concentration were also made in a plane in Ref. 153 by imaging fluorescence from two counter-propagating laser sheets. Equation 5.22 was applied using each row of pixels to compute signal ratios. Single-shot imaging of a hydrogen/air/oxygen flame allowed for calculation of means and standard deviations of OH concentration. Using 10 images for each laser sheet direction (20 total images), Figure 5.8 from Ref. 153 showed a mean peak OH concentration of ~8.8×10^{14} cm^{-1} with a standard deviation of ~$\pm 1.7 \times 10^{14}$ cm^{-1}, which is ~19.7% of the mean.

5.7.6 Combined LIF/Rayleigh/Raman

In reacting flows, flows undergoing transition-to-turbulence, and turbulent flows, the time-varying nature of flow properties makes it difficult to ascertain concentration. By making simultaneous time-resolved measurements of temperature and major species concentrations, the thermodynamic-dependent parameters in Eq. 5.9 (Boltzmann fraction, overlap integral, and fluorescence yield) can be determined, and a direct relation between concentration and fluorescence signal established. A combined fluorescence, Rayleigh scattering, and Raman scattering measurement technique was used for this purpose in Ref. 154. In that experiment, the Raman scattering was used to measure instantaneous concentrations for major species (O_2, N_2, H_2O, and H_2) in a turbulent hydrogen jet flame. This allowed for the mole fractions of the collision partners, χ_i, in Eq. 5.3 to be calculated. The combined Rayleigh/Raman scattering measurements were then used to measure temperature. The temperature-dependent collisional cross-sections and relative velocity in Eq. 5.3 could then be calculated, and the collisional quenching rate, Q_{21}, determined. The temperature-dependent absorption line-shape and Boltzmann fraction could also be determined from the temperature measurement. The additional measurement of laser energy then provided for a direct relation between NO fluorescence signal and concentration to be established. In Ref. 155, this technique was used to make concentration measurements of CO in turbulent premixed and stratified CH_4/air flames. A stated CO concentration accuracy and precision (single standard deviation) of 10% and 4.5%, respectively, were given.[155]

5.8 Pressure

Measurements of pressure can also be obtained using a LIF-based approach, although such measurements are not as common as LIF-based temperature and species concentration measurements (described in the preceding sections) for determination of the thermodynamic state of a gas. This is in part due to the implicit relationship between fluorescence signal and pressure in Eq. 5.9, as opposed to the explicit relationships with temperature and concentration.

One method by which pressure can be measured is by tuning to the center frequency of an absorption transition and relating the measured fluorescence signal to pressure. For such measurements, the selected absorption transition must be carefully chosen such that the temperature dependence (i.e. f_B) can be removed over the range of temperatures expected for the experiment. When this is done, the fluorescence signal is inversely proportional to the static pressure if certain additional simplifying assumptions are made. This approach has been used in low-quenching ($Q_{21} \ll A_{21}$) flows[133] or quenching-dominated ($Q_{21} \gg A_{21}$) flows where the pressure broadening is much larger than the Doppler broadening.[156,157]

Often for quenching-dominated LIF-based pressure measurements, however, the dependence of fluorescence signal on pressure when tuned to the center of an absorption transition is nearly removed, as N_T (and hence pressure) can be factored out of both the numerator and denominator in Eq. 5.9. An alternative approach is to infer pressure from the absorption lineshape function. This can be accomplished if a separate measure of temperature can be made so that the absorption lineshape dependence on temperature can be isolated from its dependence on pressure. Common methods include those which relate the width of the absorption lineshape to pressure,[158] those which resolve the entire absorption lineshape function,[159] and those which relate the ratio of fluorescence signal from the wing of the lineshape to the signal from the center of the lineshape.[160-162]

5.9 Doppler-Based Velocimetry

The Doppler effect can be used to determine flow velocities for atomic and molecular species. The translational motion of the absorbing species in the direction of the excitation laser's propagation, described by a velocity component U, results in a shift of the absorption line-shape function away from its transition center frequency, ν_0, according to:[58]

$$\Delta\nu = \frac{U}{c}\nu_0 \tag{5.23}$$

This velocity-dependent frequency shift of the absorption line-shape function is implicit in the overlap integral, G, and thus, its effect on fluorescence signal can be seen through the dependence of G on the velocity component, U, in Eq. 5.9. When a component of translational motion of the absorbing species opposes the laser's direction of propagation, corresponding to the negative $(-)$ solution of Eq. 5.23, the incident laser radiation appears to be at a higher frequency from the perspective of the gas. Hence, as the laser's frequency is scanned over the absorption transition, Y_ν, the measured intensity of fluorescence corresponding to this profile is shifted toward a lower frequency, or red-shifted. The converse is true when motion is in the same direction as the laser's propagation, corresponding to the positive $(+)$ solution of Eq. 5.23, where the absorption profile is shifted toward a higher frequency, or blue-shifted.

In one implementation, velocity component measurements can be made by scanning the laser over an absorption transition in both the measurement volume and a reference cell. In this case, the Doppler shift between the absorption profiles is used to compute an average velocity according to Eq. 5.23. Examples of such measurements include those in an arcjet,[121,122,126,163] supersonic underexpanded jets,[158,159,164-166] shock tunnel,[167,168] and non-reacting supersonic flow with a rearward-facing step.[169-171] Such measurements require that the flowfield be relatively steady since shot-to-shot fluctuations in fluorescence intensity from thermodynamic and fluid dynamic variations can affect the measured line-shape. The velocity measurements can also be complicated by a frequency shift in the line-shape function resulting from collisional effects (pressure). In compressible flows, the pressure field can vary significantly, and hence the collisional shift in the line-shape function can likewise vary. Absorption of laser energy can also result in an apparent frequency shift in the line-shape function. Recall that the line-shape function must be inferred from the overlap integral, G, which represents the convolution of the absorption line-shape and laser spectral line-shape. If absorption is significant, then irradiance will vary spatially according to Eq. 4.3, resulting in a spatially varying overlap integral. An analysis of how absorption affects the line-shape frequency shift is presented in Ref. 168. If flow symmetry is assumed, then the frequency shift due to pressure can be estimated.[167] Flow symmetry can also be used in the application of Eq. 4.3 to correct for the frequency shift resulting from absorption.[122] Alternatively, if two counter-propagating laser beams are used, these frequency shift effects can be completely removed. The use of counter-propagating beams results in two excitation peaks, separated in frequency by twice the velocity-induced Doppler shift. The need for a reference cell measurement to ascertain velocity can also be removed, as a counter-propagating beam approach is self-referencing.[165,172,173]

Figure 5.9 in Ref. 168 shows a two-component velocity measurement about a heat shield model taken in a hypersonic free-piston shock tunnel. In this experiment, laser sheets were directed in both the radial (vertical) and axial (horizontal) directions so that measurements of the Doppler-shifted absorption profiles for the respective directions could be obtained and compared with measurements from a static reference cell to infer velocities. An estimation of velocity errors incurred from the frequency shifts due to absorption and collisional effects was also performed. In Ref. 168, three separate absorption transitions were probed to measure two different velocity components, with one transition being used for both components. This resulted

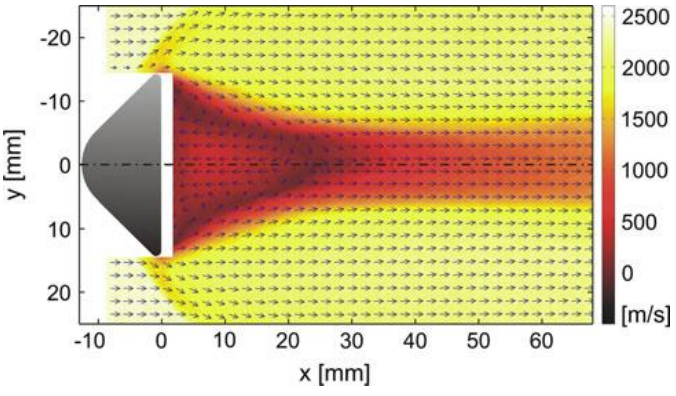

Figure 5.9. Two-component velocity measurement using fluorescence-based Doppler velocimetry technique. Vectors denote flow direction and color map represents magnitude. Image reprinted from Ref. 168 with permission of the authors and Springer Science and Business Media.

in a measured axial freestream velocity of 2394±68 m/s and a measured radial velocity of 53±50 m/s, giving respective uncertainties of ~2.8% and ~94.3%.[168]

Another form of the fluorescence-based Doppler velocity measurement is a fixed frequency method, which can allow for an instantaneous velocity component measurement. With the fixed frequency technique, a narrow linewidth laser is tuned off the absorption profile peak to a point where the slope of the profile is maximum, as described in Refs. 160 and 174. Assuming that the absorption profile is approximately linear in the region of maximum slope, the measured signal intensity can be related to the Doppler shift of the profile. This fixed frequency Doppler velocimetry technique has been applied to a free jet,[175] supersonic underexpanded jet,[176] and reacting supersonic flow.[177] The stated random and systematic errors in Ref. 176, when added in quadrature, gave a total uncertainty of ~12%. In Ref. 177, the stated lowest time-averaged and single-shot uncertainties achieved were ~3% and ~15%, respectively, for a 1600 m/s velocity range.

5.10 Flow-Tagging Velocimetry

Another technique by which velocity can be measured using fluorescence is flow-tagging velocimetry. Fluorescence-based flow-tagging velocimetry is a time-of-flight technique that involves laser excitation—or tagging—of the gas along a line, series of lines, or grid pattern. With this form of velocimetry, the species of interest in the gas absorbs the incident radiation from a laser source, which induces either of the following: 1) fluorescence, 2) a reaction that forms a product that then emits a photon via fluorescence, or 3) a reaction that forms a product that can then be probed with another laser source to induce fluorescence. Images of the fluorescence pattern are acquired at two time delays, with velocity computed by measuring the displacement of the tagged molecules between images. Typically, a line or series of lines can be used to measure a single-component of velocity while a crossed grid pattern can be used to measure two-components. Two general fluorescence-based methods of flow-tagging velocimetry are discussed here; one that requires a single laser source and another that requires multiple laser sources. The main advantage of flow-tagging velocimetry, as compared to most Doppler-based methods (which are time averaged), is that it can make instantaneous (single-shot) measurements with fast time resolutions (as short as a few hundred nanoseconds). A disadvantage, however, is that flow-tagging velocimetry cannot provide full velocity field information. A broader discussion of molecular-tagging velocimetry, which relies on molecular tracers for flow-tagging, is provided in Ref. 178.

5.10.1 Single-laser methods

The first method involves either direct or indirect excitation of fluorescence with a single laser source. The first application of this method to a gaseous flow involved excitation of phosphorescence of biacetyl molecules, as described in Ref. 179. If this method is used, the fluorescence lifetime of the tagged molecules must be long enough so that advection provides for measurable displacements with tagged regions having signal intensities that are still above the detection limit of the imaging system at the time the second image is acquired. Typical experiments involve capturing a reference image acquired during the tagging process, or a relatively short time thereafter. If a single-framing camera is used, such as in Ref. 180, a single reference image or set of reference images is acquired. The timing of the single-frame camera is then delayed and a subsequent image or set of images is then acquired. If a two-camera system or dual-framing camera is used, such as in Ref. 181, the delayed image is acquired in sequence after the reference image. The velocity is computed by measuring the displacement of the tagged molecules that occurs in the time between when the reference and delayed images were acquired. The form of this technique relying on direct excitation of fluorescence for flow tagging has been applied to the study of supersonic jets,[182-188] hypersonic boundary layers,[180,181,189,190] and arcjet flowfields.[122]

Figure 5.10, taken from Ref. 180, shows images from tagging a single line of nitric oxide using direct excitation of fluorescence within a flat plate hypersonic laminar boundary layer. In this Figure, the left-most image corresponds to the reference image, while the remaining images, from left to right, correspond to delayed images taken at 250 ns, 500 ns, and 750 ns after tagging, respectively. Measurements of freestream velocity, spatially averaged from a point just above the velocity boundary layer (3 mm) to 15 mm above the flat plate, resulted in a mean of 3,035±100 m/s at 90% confidence, giving an uncertainty of 3.3% of the mean.[180] Single-shot uncertainty estimates for a 3,000 m/s freestream flow and for camera delay settings of 250 ns, 500 ns, and 750 ns were 4.6%, 3.5%, and 3.5%, respectively.[180]

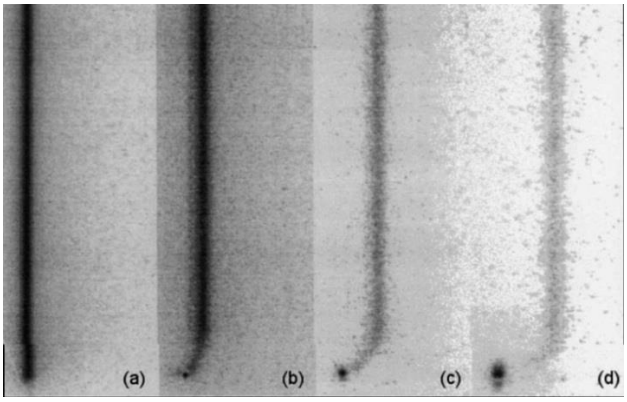

Figure 5.10. Single-line excitation of nitric oxide fluorescence used to study hypersonic boundary layer flow over a flat plate. Images, from left to right, correspond to camera delay settings of 0 ns, 250 ns, 500 ns, and 750 ns. Image reprinted from Ref. 180 with permission of the authors.

An indirect excitation scheme, as described in Refs. 191 - 193 , relies on photodissociation of molecular nitrogen for flow tagging. The technique uses a femtosecond laser pulse to dissociate molecular nitrogen into two nitrogen atoms, which then recombine after a collision, forming molecular nitrogen in an intermediate state. A subsequent collision brings the molecular nitrogen to

an excited electronic B state, which then emits a photon via fluorescence upon transitioning to the excited electronic A state. Ref. 193 provides a description of this process. One benefit of this indirect technique, known as Femtosecond Laser Electronic Excitation Tagging (FLEET), is that the recombination rate of dissociated atomic nitrogen allows for a much longer fluorescence lifetime. This would allow displacements to be measured over greater time scales, providing for accurate measurements of velocity in low-speed flow regions, such as in a hypersonic wake flow. Additionally, the technique relies on molecular nitrogen for tagging, which is present in most hypersonic facilities.

5.10.2 Multi-laser methods

A second method of fluorescence-based flow-tagging velocimetry involves writing a line, series of lines, or grid pattern into the flowfield by one of several laser-based mechanisms. This pattern can then be interrogated, or read, by subsequent laser pulses to induce fluorescence, allowing for the determination of velocity through measurement of the displacement of the pattern. Such techniques usually involve two or three different lasers and are therefore more time consuming to set up and more difficult to execute.

One mechanism by which a pattern can be written into the flowfield is via ionization of the absorbing species, known as Laser Enhanced Ionization (LEI) flow tagging. The tagging process is accomplished by promoting the species (such as sodium in Refs. 194-196) to a higher energy state via laser excitation near the ionization limit. Collisions then result in the ionization of the species, with the tagging pattern corresponding to the ionized regions. Subsequent laser pulses are used to induce fluorescence of the absorbing species in regions that have not been photo-ionized. Supersonic measurements of velocity in a shock tube were performed using LEI flow-tagging in Refs. 194 and 195, and hypersonic velocity measurements in an expansion tube were performed in Ref. 196.

A second mechanism that can be used to write a pattern into the flowfield is by vibrational excitation of molecular oxygen via Raman pumping. This is followed by reading the pattern of the vibrationally-excited oxygen by inducing fluorescence. The technique, known as Raman Excitation and Laser-Induced Electronic Fluorescence (RELIEF),[197] is advantageous as it relies on the flow-tagging of oxygen which is a common working gas of most hypersonic facilities. This technique has been used to characterize turbulence in a free jet[198] and underexpanded jet.[199] The RELIEF technique, however, is limited to temperatures below 750 K. Above this temperature, a significant fraction of oxygen molecules are vibrationally excited, making it difficult to distinguish the tagged molecules from the background.[200]

Yet another mechanism involves using one laser to photo-dissociate a molecular species. This results in the formation of a product species for which a second laser can be used to read the location of the written pattern by exciting laser-induced fluorescence in the product species. The formation of the product species typically occurs through one or more reactions. A list of partner

species used in the writing and reading process include: H_2O-OH,[201-207] N_2O-NO,[208] O_2-O_3,[209,210] N_2/O_2-NO,[211-214] and NO_2-NO.[184,215-222]

Figures 10(a) and 10(b), taken from Ref. 219, show images of vibrationally excited NO fluorescence in a grid pattern formed via photodissociation of NO_2 in a mixture containing 6.3% NO_2 in N_2. The images were taken in a supersonic underexpanded jet 400 ns (Fig. 5.11(a)) and 800 ns (Fig. 5.11b) after the pattern was written into the flow with a two-dimensional array of 355 nm beams. Two components of velocity were obtained by relating the displacement of the grid in the left image to a grid imaged in a stationary gas. The upper half of Fig. 5.11(c), taken from Ref. 219, shows measured streamwise velocities compared with computation, shown in the lower half of Fig. 5.11(c). The use of two pulsed dye lasers in this experiment permitted the excitation of both a low (J = 1.5) and high (J = 8.5) rotational level within the same vibrationally excited (v = 1) NO state. The fluorescence images corresponding to the low-J (Fig. 5.11(a)) and high-J (Fig. 5.11(b)) rotational levels also allowed for measurement of the rotational temperature by using a calculation similar to that presented in Eq. 5.16. The top half of Fig. 5.11(d), from Ref. 219, shows measured rotational temperature compared with computation, shown in the lower half of Fig. 5.11(d). Stated root-mean-square (RMS) uncertainties in the velocity measurement were ~5% with high signal-to-noise.[219] The stated RMS uncertainties in rotational temperature ranged from 9% to 35% prior to the Mach disk.[219]

NO_2-NO flow tagging velocimetry has also been used to study boundary layer transition on a flat plate in a Mach 10 wind tunnel.[221,222] Pure NO_2 was seeded into the boundary layer through a spanwise slot located downstream of the sharp leading edge. The angle of attack of the flat plate was 20 degrees, reducing the edge Mach number to about 4.2. Parallel focused beams of 355 nm light oriented normal to the surface of the flat plate (and in a plane parallel with the streamwise direction of the flow) dissociated the NO_2, creating NO. After a 40 ns delay, the NO was probed by a 226 nm laser, at which time the camera acquired an image. One microsecond later, a second 226 nm laser probed the NO and the second image was acquired with the same camera. The two images were compared to compute velocity profiles. Figure 5.12 shows the resulting velocity

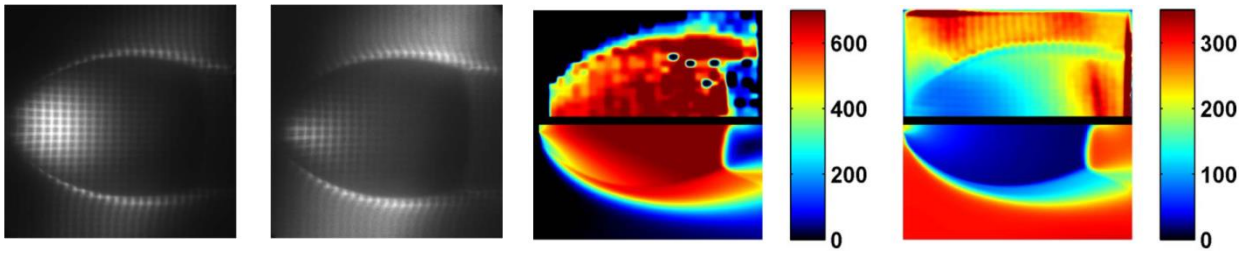

(a) (b) (c) (d)

Figure 5.11. Flow-tagging images of vibrationally excited NO fluorescence obtained (a) 400 ns and (b) 800 ns after photodissociation of NO_2. The two-dimensional grid pattern allows for calculation of two velocity components. Measured (c, top) and computed (c, bottom) streamwise velocity maps. Measured (d, top) and computed (d, bottom) rotational temperature map. Image reprinted from Ref. 219 with permission of the authors and the publisher.

profiles for two cases, one with no trip (i.e. tripping element, a protuberance designed to trip the flow from laminar to turbulent) and one with a 1-mm tall cylindrical trip, where the measurements were made downstream of, and on the centerline of, the trip. (The laminar boundary layer thickness was also approximately 1 mm thick.) The figure shows mean profiles (black, top two charts) as well as profiles of the fluctuating component of velocity, *u'* (red, bottom two charts). For the case of no trip, the velocity profiles compare well with a compressible Blasius solution (shown in light grey). When the trip is present, the measured mean profiles depart from the laminar solution, showing a profile that is more full than the laminar profile near the plate surface with a pronounced velocity deficit near the edge of the profile. The fluctuating streamwise velocity increases by a factor of three, up to 250 m/s, between the two cases, with the fluctuations highest in the wake of the trip. The single-shot measurement precision was 15-25 m/s, which was 1-2% of the maximum velocity in the boundary layer. The accuracy was estimated to be 5-15 m/s.[221]

5.11 Advantages and Limitations of Laser-induced Fluorescence

The time scales associated with inducing fluorescence via laser excitation are typically a few hundred nanoseconds, which is much shorter than hypersonic flow time scales, therefore providing sufficient temporal resolution for high-speed transition-to-turbulence measurements. The availability of pulsed lasers capable of picosecond and femtosecond excitation allow for fluorescence measurements with time scales much less than those associated with collision and reaction time scales. Recently developed kHz- and MHz-rate pulsed laser systems have allowed image sequences consisting of tens to thousands[223] of images to be acquired, providing time-resolved information pertaining to high-speed fluid dynamic behavior. Both fluorescence-based velocimetry[218] and visualization [224, 225] experiments in hypersonic flow fields have been performed with these types of laser systems. The spatial resolution of a LIF technique is also sufficient for many applications, and higher than other techniques such as Raman or CARS, with laser sheet thicknesses typically in the range of 0.1 to 1 mm and magnifications of tens of pixels per mm, depending on the experimental setup. Fluorescence-based measurements are more sensitive than other techniques (for example Raman spectroscopy) with sensitivity on the order of parts-per-million or better.[5]

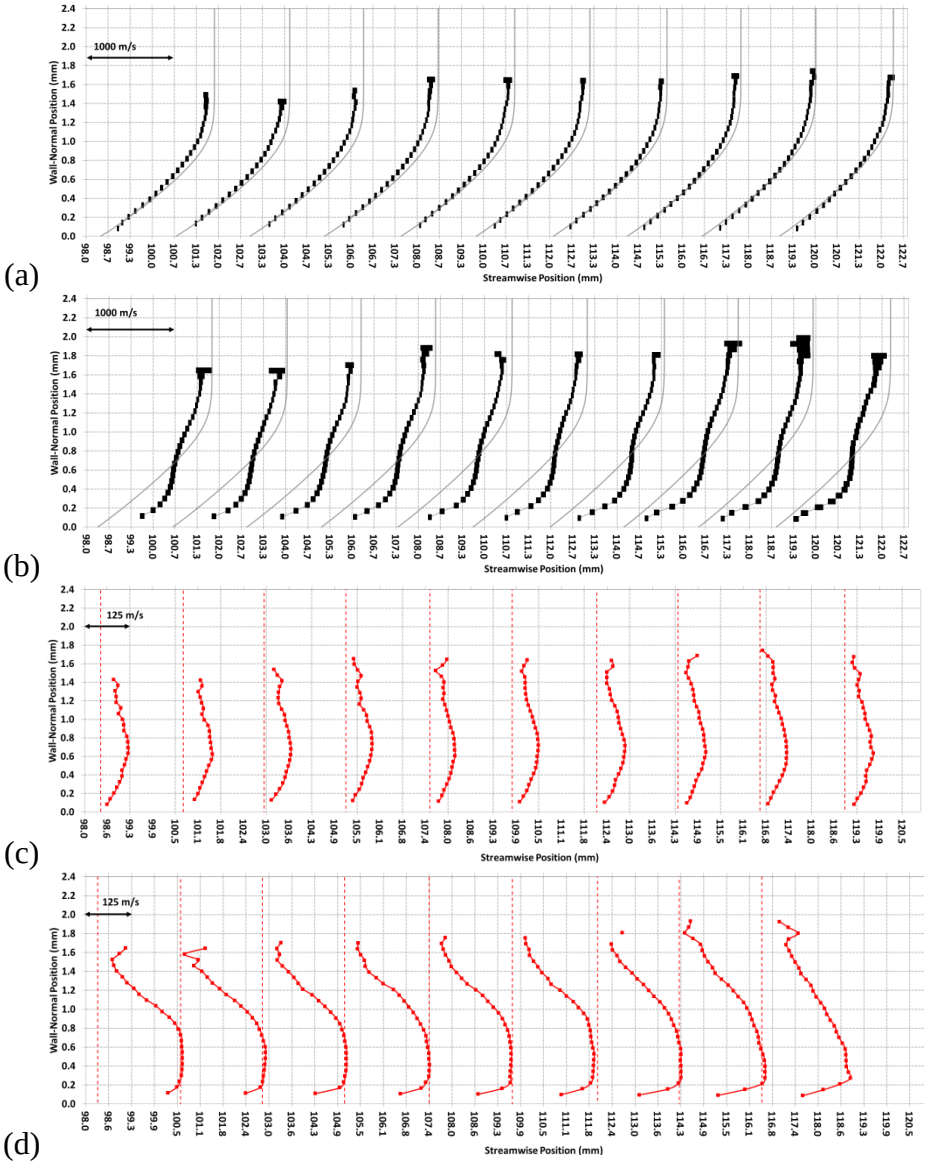

Figure 5.12. Streamwise velocity profiles on a flat plate in a Mach 10 facility for the case of no trip (a) and a k = 1 mm tall, 4 mm diameter cylinder trip (b) and the fluctuating streamwise velocity for no trip (c) and a k = 1 mm tall, 4 mm diameter cylinder trip (d). Images reprinted from Ref. 222 with permission of the authors.

Additionally, a wide range of species including intermediate combustion species can be probed using fluorescence techniques. Reference 109 provides an extensive listing of many species that have been detected using LIF and other methods. Another advantage of LIF is that it is readily extended to planar or volumetric measurement (see Refs. 226 and 227).

Several factors complicate acquisition and interpretation of LIF signals, complicating quantitative measurements. Quenching of the fluorescence, which prevents easy quantification of signal intensities, was discussed extensively above. Absorption of laser energy as the laser light passes through the flowfield can limit the effectiveness of fluorescence-based measurements, as the energy will decrease in an exponential manner over a given spatial path length according to

the Beer-Lambert relations in Eqs. 4.3 and 4.4. This makes quantitative measurements difficult, as the laser energy at a particular location may not be easily determined. Absorption can be significant when the concentration of the absorbing ground state population is high, the transition cross-section is relatively large, the Einstein B coefficient for stimulated absorption is relatively large, and/or the path length through which the laser radiation passes is relatively long. To avoid strong absorption, a transition may be selected for which the population is small based on analysis of the Boltzmann fraction, as was done for PLIF visualization measurements in a hypersonic shock tunnel described in Ref. 228. Absorption can also limit measurement capabilities when fluorescence from the probed volume is re-absorbed by the species of interest. This effect, known as *radiative trapping*, occurs when fluorescence emission at frequencies readily absorbed by highly populated states must pass through gas containing these potential absorbers before reaching the imaging system. Measurements in a non-uniform or turbulent mixture are especially susceptible to errors associated with absorption and radiative trapping effects, as the absorption coefficient is a spatially- and temporally-varying property. A discussion of these issues, and some methods used to circumvent them, is provided in Ref. 5.

Another disadvantage of LIF is that it usually probes only a single species at a time, compared to Raman or CARS, which can interrogate many species simultaneously. However, the fact that PLIF can measure spatial distributions of species can compensate for the single-species capability in some applications.

Consideration must also be given to the optical access of the test facility. Since much of the work described in this discussion requires fluorescence excitation using laser frequencies in the UV portion of the electromagnetic spectrum, the window material used in hypersonic facilities must be capable of transmitting such frequencies with minimal absorption. Also, typically two or three windows are required for LIF or PLIF applications. The laser (beam or sheet) is typically brought in from one window and observed through another window at right angles to the first window. A third window can allow the laser to leave the test section, reducing scattered light, and allowing the quantification of absorption of the laser beam/sheet in some applications. These windows are typically relatively large compared to those required for CARS or diode laser absorption measurements. When short-pulse LIF experiments are performed, the inverse relationship between the pulse temporal width and spectral width (which for a Gaussian pulse is $\tau_{laser} = 0.44/\Delta\nu$)[111] can result in distortion of the temporal characteristics of the pulse. This is because the refractive properties of the optical windows of the test facility affect the speed with which the frequency components of the short pulse pass through the window material. Reference 111 discusses issues related to short pulse excitation and interaction with optical components.

6. Rayleigh and Raman Scattering

6.1 Introduction

When a light beam passes through a gaseous medium, it can interact with the gas molecules or particles in the gas, thereby scattering light away from the path of the incident beam. *Elastic* scattering occurs if no energy is gained or lost to the medium. If energy is either absorbed or lost by the medium, the scattering is *inelastic*. Light scatter from particles that have a diameter, d, on the order of or larger than the light wavelength, λ, is termed Mie scattering. Scattering for which $d << \lambda$ is known as *spontaneous Rayleigh scattering* if elastic and *spontaneous Raman scattering* if inelastic. These processes are shown schematically in Figs. 6.1 and 6.2. Represented on the energy level diagram in Fig. 6.1, a photon excites a molecule from an originating state, 1, to a 'virtual' state, 2, from which the scattered photon is emitted. The virtual state, represented by a dashed line, is not an actual resonant state of the molecule. Instead, it indicates a non-resonant, short-lived state in which the electron distribution of the molecule is distorted. This virtual state immediately relaxes to the originating state (in the case of Rayleigh scattering) or another state (in the case of Raman scattering). Relaxation to a higher lying (e.g. vibrational) state than the originating state is termed *Stokes Raman* scattering. In this case, the molecule absorbs a quantum of energy through this process. In *anti-Stokes Raman* scattering the molecule imparts a quantum of energy to the scattered photon so that the scattered photon has higher energy than the incident photon. In this case, the originating state must not have been a ground state.

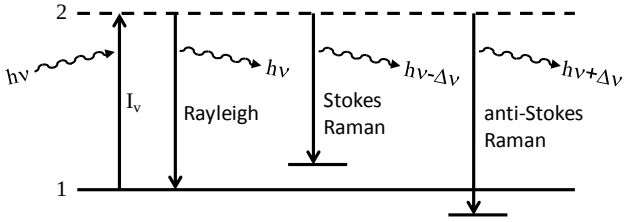

Figure 6.1. Energy level diagram indicating incident radiation, Rayleigh scattering and Raman scattering.

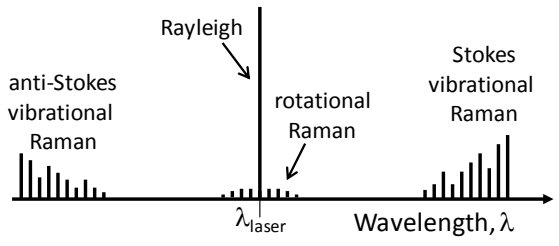

Figure 6.2. Notional Raman/Rayleigh spectra.

Figure 6.2 shows notional Raman/Rayleigh spectra, not drawn to scale. Rayleigh scattering is shown at the laser's wavelength. Discrete pure rotational Raman lines, associated with rotational quanta imparted to or subtracted from the incident laser frequency, are shown on opposite sides of the Rayleigh peak. Vibrational Raman bands are located further away, spectrally shifted towards the red (Stokes) and the blue (anti-Stokes). The vibrational Raman bands show rotational fine structure. Raman scattering is much weaker than Rayleigh scattering. Raman scattering is typically three orders of magnitude smaller than Rayleigh scattering for most gases of interest to supersonic and hypersonic flows.[5]

6.2 Theory of spontaneous Rayleigh and Raman scattering

Comprehensive reviews of the theory and application of Rayleigh and Raman scattering have been given by others.[5,109,229,230] Herein we provide a brief introduction and overview. Later sections will show how this theory is applied to measure thermodynamic properties. Consider an electromagnetic wave incident upon a molecule, perturbing the molecule's electron cloud and making it oscillate at the same frequency as the incident wave. These oscillations cause a periodic charge separation within the molecule, known as an induced dipole moment. Oscillating dipole moments act like antennas, emitting radiation. As described in more detail by Baldwin,[231] if these oscillations are in-phase, the emission adds constructively, producing a coherent beam. If out-of-phase (for example, in the direction orthogonal to the beam), the emitted light interferes destructively and the radiation cancels. For a monochromatic plane wave passing through a gas, the constructive interference occurs only in the forward direction. The resulting emitted coherent light is perfectly in-phase with and indistinguishable from the incident wave. In a gas composed of a finite number of molecules, the destructive interference at other angles is not fully complete because of statistical variations in the number of particles located in different wavelength-sized volumes of the gas.231'[232] That is, there are not exactly the same number of particles in each wavelength sized volume, which would be required to cancel out the radiation perfectly. This statistical variation in the number density then leads to Rayleigh and Raman scattering. Rayleigh and Raman increase significantly in intensity at shorter wavelengths: both scale approximately as $1/\lambda^4$.[5]

The radiant intensity, I^{Ω}, which is the scattered power per unit solid angle, is proportional to the square of the induced dipole moment. The induced dipole moment, $\vec{p}$, is given by:[5]

$$\vec{p} = \varepsilon_0 \alpha \vec{E} \tag{6.1}$$

where ε_0 is the permittivity of free space, α is the molecular polarizability and $\vec{E}$ is the incident electric field given by $\vec{E} = \overrightarrow{E_0}\cos(\omega_0 t)$, where $\overrightarrow{E_0}$ is the amplitude of the electric field, ω_0 is the frequency of the laser light and t is time.

The polarizability of a molecule depends on its internal structure and varies with time during vibrational oscillations at the natural frequency of the molecule, ω_v, vibrating in the direction of its normal spatial coordinate, Q. The polarizability can be approximated with a Taylor series expansion:

$$\alpha = \alpha_0 + \left(\frac{\partial \alpha}{\partial Q}\right)_0 dQ \tag{6.2}$$

where the small physical displacement, dQ, of the atoms about their equilibrium positions (denoted by the subscript 0) during vibrations is:

$$dQ = Q_0 \cos(\omega_v t) \tag{6.3}$$

Combining Eqs. (6.1)-(6.3):

$$\vec{p} = \left[\alpha_0 + \left(\frac{\partial\alpha}{\partial Q}\right)_0 Q_0 \cos(\omega_v t)\right] \varepsilon_0 \overrightarrow{E_0} \cos(\omega_0 t) \tag{6.4}$$

Expanding and using a trigonometric identity:[5]

$$\vec{p} = \alpha_0 \varepsilon_0 \overrightarrow{E_0} \cos(\omega_0 t) + \tfrac{1}{2}\left(\frac{\partial\alpha}{\partial Q}\right)_0 \varepsilon_0 Q_0 \overrightarrow{E_0} [\cos(\omega_0 - \omega_v)t + \cos(\omega_0 + \omega_v)t] \tag{6.5}$$

The first term on the right side of Eq. (6.5) describes Rayleigh scattering at a frequency corresponding to the incident laser's wavelength. The second term indicates Raman scattering which is shifted from the Rayleigh scattering by $\pm\omega_v$ resulting in upshifted (anti-Stokes) and downshifted (Stokes) Raman scattering. While significant theory has been developed to describe the physics of Raman and Rayleigh scattering, the strengths of the scattering for different gases is generally measured and reported as a temperature-independent differential cross section:[5]

$$\left(\frac{\partial\sigma}{\partial\Omega}\right)_{zz} \equiv \frac{I_{zz}^{\Omega}}{NI} \tag{6.6}$$

which can be rearranged as:

$$I_{zz}^{\Omega} = \left(\frac{\partial\sigma}{\partial\Omega}\right)_{zz} NI \tag{6.7}$$

where the subscript *zz* refers to a polarization in the z (vertical) direction caused by an incident electric field oriented in the *z* direction, *N* is the number density of the gas and *I* is the laser irradiance.[5] The differential cross sections vary by process (Rayleigh vs. Raman), by molecule, and vary with the laser wavelength but are independent of pressure and temperature.

Rayleigh scattering from different molecules cannot be distinguished spectrally, so it is not usually used to detect individual species. Under circumstances where the composition is fixed or known, or limited to vary under controlled conditions, [233, 234] Rayleigh scattering can be used to measure the gas density, ρ. As discussed further below, the Rayleigh scattering cross section varies from molecule to molecule, with some hydrocarbon species having cross sections more than an order of magnitude larger than N_2. The cross section for a mixture of gases is equal to the mole-fraction-weighted average of the individual cross sections. If the composition can be estimated or measured, for example

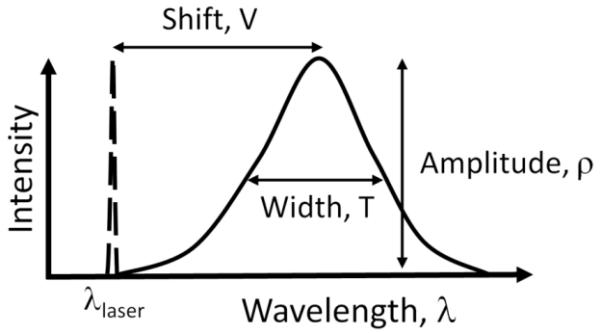

Figure 6.3. Notional sketch of spectrally dispersed Rayleigh scattered light (solid line) which has been Doppler shifted from the incident laser light (dashed).

by Raman scattering,[235] then the effective cross section for the gas mixture can be determined, allowing the density to be determined from the measured Rayleigh scattering. Under conditions where the pressure and composition are known or can be determined and where the perfect gas law applies, the gas temperature can be inferred from the measured density.[5] Such measurements can suffer from interference from Mie scattering from particles and laser scattered light.[5] To avoid Mie interferences, the gases can be filtered to remove particles. Careful experimental design and blackening of surfaces can minimize scattered laser light.

Spectral analysis of Rayleigh scattering yields additional parameters that can be measured. Figure 6.3 shows a schematic of the dispersed Rayleigh scattered light (solid line), separated from the incident laser light (dashed line). The spectral shift of the Rayleigh from the laser is caused by the Doppler shift of the gas relative to the incident light beam and depends on the detection angle. The width of the Rayleigh spectrum depends, in part, on the gas temperature. The amplitude of the scattering, as described above, depends on the gas density (and composition). Thus, in principle, by spectrally dispersing the Rayleigh scattered light, the temperature, velocity, and density of a gas can be measured simultaneously. These effects are detailed below with examples given.

Revisiting Eq. (6.5), notice that for Raman scattering to occur, $\left(\frac{\partial \alpha}{\partial Q}\right)_0$ must be nonzero. This happens when a molecule exhibits a *change* in its polarizability with vibrational displacement. For example, as the atoms in the N_2 molecule vibrate, they become less polarizable as the atoms approach each other (charges exhibiting more force because they are closer to each other) and more polarizable when further apart (charges more weakly interacting). This results in a nonzero $\left(\frac{\partial \alpha}{\partial Q}\right)_0$. Such vibrations are *Raman active*. On the other hand, some vibrational modes do not change the molecule's polarizability, for example the asymmetric stretch of CO_2 has the following vibration pattern: O→ ←C O→. Such modes have $\left(\frac{\partial \alpha}{\partial Q}\right)_0 = 0$ and are termed *Raman inactive*. Further quantum mechanical selection rules and molecular structure considerations (atomic mass, bond length, moment of inertia, etc.) determine the shape and structure of the Raman spectra.[5] Since the frequency of Raman spectra depend strongly on the individual species' molecular structure (each vibrational resonance occurring at a different energy), Raman spectra from different molecules appear spectrally separated when they are dispersed, typically using a grating-based spectrometer equipped with a camera to acquire the spectra. Because Raman scattering is species-specific, it can be used to measure individual species concentrations, where in Eq. (6.6), *N* is the species being detected and the differential cross section is that of the individual species.

6.3 Advantages and Disadvantages of Rayleigh and Raman Scattering

Rayleigh and Raman scattering have many inherent advantages compared to other measurement techniques. Both use just a single laser and the laser need not be resonant with any

particular molecular resonance as in absorption or laser induced fluorescence (LIF). This allows high-powered, fixed frequency lasers to be used for Rayleigh or Raman. Since they are linear laser techniques involving only a single excitation beam, Raman and Rayleigh are relatively easy to set up and understand, and the data are, in general, easier to analyze than nonlinear techniques like coherent anti-Stokes Raman spectroscopy (CARS). Neither Raman nor Rayleigh is sensitive to collisional quenching, a phenomenon which complicates the interpretation of LIF signals. Absolute intensity calibration of both techniques is relatively straight forward and easily performed. Raman and Rayleigh can be performed simultaneously using the same laser to measure species concentrations (Raman), temperature (Raman and/or Rayleigh), density (Raman and/or Rayleigh) and velocity (Rayleigh).

The major disadvantage of Raman and Rayleigh scattering is the low signal intensity. The low signal from Raman scattering generally prevents minor species (less than a few percent by mole fraction) from being detected using this technique. Because the signals are so low, large (low *f*-number) collection optics are usually used. Ideally, the detection optics need to be placed close to the measurement region and, in ducted flows, large windows are required. Hypersonic and combusting flows can sometimes be luminous. Natural luminosity, like spontaneous Rayleigh and Raman scattering, emits light in all directions. In order to improve the signal-to-noise ratio, temporal, spatial, and spectral filtering can be used to collect the desired radiation and block unwanted natural luminosity. For example, gated detection of pulsed signals (or lock-in detection of continuous signals) can be used.

6.4 Translational Temperature, Velocity, and Density Measurements

The gas temperature and velocity can be determined from the Rayleigh spectrum by resolving the Doppler broadening and Doppler shift, respectively. The Rayleigh scattering linewidth is typically in the range of 1-6 GHz (0.03-0.17 cm^{-1}) for supersonic and hypersonic flow experiments in the range of a few hundred to a few thousand kelvins, depending on the temperature and angle of incidence of detection and collection of the light (see Ref. 229 for detailed information about the Rayleigh scattering lineshape and angular dependence). A high-resolution laser can be used so that the broadening caused by the laser's lineshape is negligible compared to this Doppler broadening. For example, injection seeded, pulsed Nd:YAG lasers typically have linewidths of about 0.1 GHz (0.004 cm^{-1}) while continuous sources can have linewidths that are orders of magnitude smaller. To spectrally resolve Rayleigh scattering, a high-spectral-resolution instrument is required. Two methods, described below and also in the introduction, are typically used: gas vapor cells and Fabry-Perot etalons.

A gaseous cell filled with iodine vapor can be used in combination with excitation in the visible wavelength range, where I_2 has many absorption lines, by placing a low-pressure gas cell containing crystalline iodine and I_2 vapor in front of a detector or camera. The diameter of the cell should be larger than the diameter of the collection lens. The cell length, pressure and temperature of the I_2 cell are chosen to control the I_2 gas concentration and spectral line shape

and therefore the absorption magnitude and profile. Attenuation of transmitted light by a factor of 10^5 can be achieved using high-resolution cw lasers, though it is more difficult to achieve attenuations greater than ~10^3 with off-the-shelf injection-seeded, pulsed Nd:YAG lasers.[236] The absorptions can be used to reject spurious scattered laser light, while passing the pressure- and Doppler-broadened and Doppler-shifted Rayleigh scattering, allowing background-scatter-free density measurements. These sharp absorption features can also be used for temperature and velocity measurements by using the steep edge of the absorption spectral profile to provide spectral resolution. Since the absorption spectrum of the gas filter is well known, if the laser frequency is scanned across the filter, then the Doppler-broadened and Doppler-shifted Rayleigh-scattered light will transmit through the filter, being acquired by the camera. Each pixel on the camera will then have obtained a convolution of the Rayleigh-scattered light with the absorption spectrum. These spectra can then be deconvolved to determine the gas temperature through the thermal broadening and gas velocity through the observed Doppler shift. Miles et al.[229] demonstrated this approach in a Mach 2 pressure-matched jet flow, shown in Fig. 6.4. Variations of this technique can provide both time-averaged and single-shot measurements. For single-shot measurements, the dynamic range of velocities that can be measured is limited, although by increasing the gas cell buffer gas pressure, the dynamic range has been increased by Elliot et al,. who made single-shot measurements with ~9% uncertainty over a velocity range from 200 to 600 m/s.[237,238]

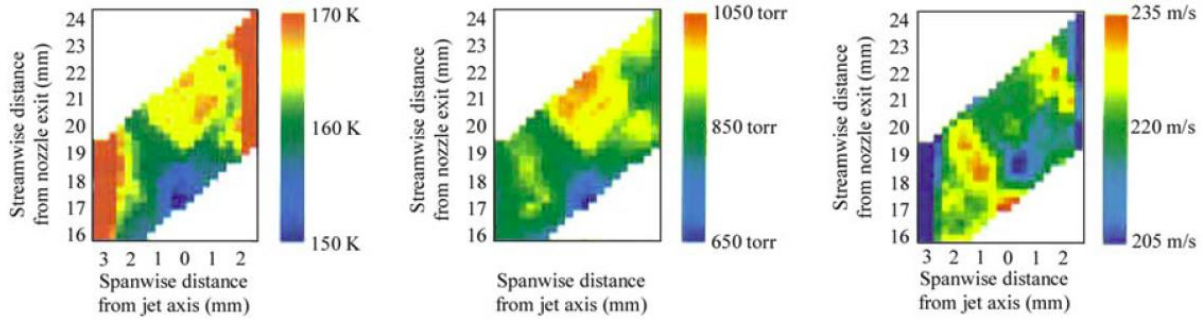

Figure 6.4. Temperature (left), pressure (center) and velocity (right) measured in a Mach 2 supersonic jet flow using Rayleigh scattering observed through a gas vapor cell using a frequency-scanned, injection-seeded Nd:YAG laser.[229]

By using a Fabry-Perot etalon, single-shot Rayleigh spectra can be obtained, allowing instantaneous (in ~100 ns) and simultaneous measurement of temperature, density and velocity. A Fabry-Perot etalon consists of two planar, reflective surfaces that cause interference, dispersing the transmitted light spatially, so that in the focal plane of the etalon, the spectrum of the light is separated spatially and can be resolved spectrally. Two different strategies have been developed to acquire these spectra. The first uses a CCD camera in the focal plane of the etalon to capture the dispersed spectrum.[239-242] The second method uses spatial masks or mirrors to direct the Rayleigh-scattered light to single-point detectors such as photo-multiplier tubes

(PMTs).[243,244] Typically, CCD cameras read out more slowly than single-point detectors such as PMTs, so using PMTs generally results in higher-speed detection. Measurement rates up to 32 kHz have been reported using this approach.[244] However, using a CCD camera offers several measurement advantages, described below.

Figure 6.5 shows one such example of CCD-based detection of Rayleigh-scattered light from Bivolaru et al.[241] A pulsed Nd:YAG laser is focused into a heated Mach 1.6 jet flow. The Rayleigh-scattered light is collected at right angles by a lens system that down-collimates the collected light and passes it through a solid etalon. The etalon-processed light is then focused on an electron-multiplying charged-coupled device camera (EMCCD) where the interference fringes are realized. This image is called an interferogram. An optical fiber (OF) directs some of the spectrally narrow laser light into the optical path so that a circular reference fringe will appear in the interferogram, as in Fig. 6.6(a). The pair of oval patterns located in the white rectangle show Doppler-shifted, Doppler-broadened, Rayleigh-scattered light collected by the lenses and dispersed by the etalon. A similar pattern is shown on the left side of the interferogram. These four oval patterns originate from four different spatial locations a few mm apart in the flow, thus resulting in four simultaneous, spatially-separated measurements. The gas velocity, $\boldsymbol{V}$, and the Doppler shift, Δf, are related by: $\Delta f = ((\boldsymbol{k_s}-\boldsymbol{k_o})\cdot \boldsymbol{V})/\lambda$, where λ is the wavelength of the incident light, $\boldsymbol{k_o}$ is the wave vector of the incident light and $\boldsymbol{k_s}$ is the wave vector of the collected light. (The wave vector points in the direction of light propagation and has a magnitude of $2\pi/\lambda$.) In the vector diagram shown in Fig. 6.5, $\boldsymbol{k_{o1}}$ is the wave vector of the incident light and $\boldsymbol{k_{s1}}$ is the wave vector of the collected light. The observed Doppler shift measures the velocity component V_1 in the direction defined by $\boldsymbol{k_{s1}} - \boldsymbol{k_{o1}}$, which bisects the angle β between the laser and collection wave vectors. Similarly, a mirror M_r reflects this incident beam back through the lens, L_2, and into the measurement volume with wave vector $\boldsymbol{k_{o2}}$ resulting in collected Rayleigh signal having a wave vector $\boldsymbol{k_{s2}}$. This signal is sensitive to the velocity component V_2. The reflected beam was slightly misaligned in the downward direction so that the two measurements would be spatially separated on the interferogram, shown in Fig. 6.6(a). Furthermore, the geometry of this experiment was constructed so that the V_1 would be orthogonal to the jet axis, measuring a radial velocity component while V_2 was parallel to the jet axis, measuring the axial velocity component. In Fig. 6.6(a), four spatially separated measurements of axial velocity are collected in the bottom half of the interferogram while four measurements of radial velocity are collected in the top half. Figure 6.6(b) shows the two boxed peaks after they have been processed to linearize the interferograms and to bin the data into single spectra.[240,241] These spectra were fitted with Gaussians to determine the Doppler shift and broadening associated with Rayleigh scattering, relative to the reference peaks. Subsequent work by this team and others has been able to simultaneously determine the gas velocity, temperature and density from similar spectra.[245,246]

In Ref. 241, Bivolaru et al. reported velocity measurements with a precision of ~40 m/s in a flow with ~1200 m/s, or about 3% of the maximum velocity. The dynamic range of the

instrument was ~3000 m/s. (The dynamic range is mainly determined by the thickness of the etalon, which sets the free spectral range, or fringe-to-fringe spectral separation.) Thus, expressed as a percentage of the dynamic range of the instrument, the measurement precision is ~1%. To obtain more precise measurements at lower temperatures, the experiment can be designed to use higher spectral resolution.

The use of the camera-based approach has some advantages over the PMT-based approach. First, it can tolerate (and in fact, benefits from) scattering from stationary surfaces in the flow. Such scattering, as long as it is not too large, provides a reference frequency to determine the Doppler shift. Second, having a laser frequency reference in each interferogram makes the system insensitive to variations in the etalon transmission spectrum or the laser wavelength. In typical PMT-based experiments, the etalon must be temperature controlled, vibration isolated (if it is an air spaced etalon) and the laser frequency must be carefully controlled. Uncontrolled drift in either the etalon or laser would result directly in a systematic error in the PMT-based approach while it is automatically corrected in the CCD-based approach. A third advantage of the CCD-based approach is that it is somewhat more tolerant of scattering from clusters and particles in the flow, lessening the need for gases to be filtered. Scattered light from particles typically appears in CCD-based interferograms as spatially distinct, circular artifacts. These can sometimes be removed by image processing. However, if the scattering is too large either spatially or in intensity, it can corrupt the measurement; even in this case, other spatial locations in the flow may yield measurements from the same interferogram. As shown in Fig. 6.6, the CCD-based detection allows multiple spatial points to be measured simultaneously, allowing measurements at adjacent spatial locations to be correlated. Furthermore, with CCD-based detection, it is straightforward to measure multiple velocity components with the same instrument, also shown in Fig. 6.6. Finally, CCD-based detection has often been combined with pulsed-laser excitation, which has two benefits: it makes the measurement instantaneous, occurring in ~10 ns, and the signal intensity is much higher, allowing measurement in much lower density flows, such as atmospheric-pressure flames and low-pressure gas flows. Instantaneous measurements at 1/5 of atmospheric density or lower are possible with this approach.[241]

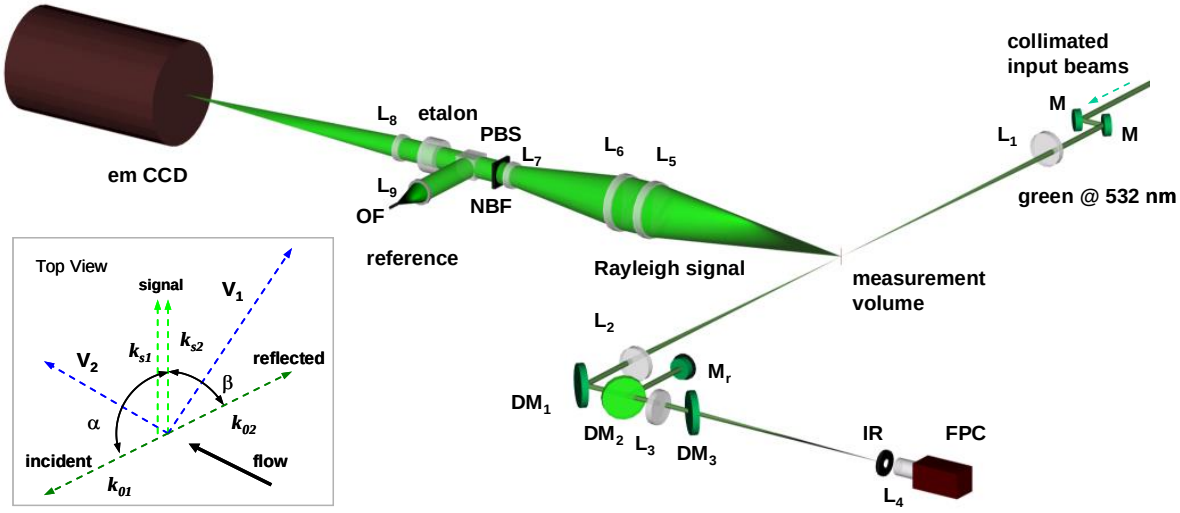

Figure 6.5. Two-component interferometric Rayleigh scattering system from Ref. 241. Mirrors are denoted by M, dichroic mirrors by DM and lenses by L. PBS is a polarizing beam splitter while NBF is a narrowband filter. IR is an iris and FPC is a focal plane camera used to monitor the beam alignment. In this experiment, the dichroic mirrors were required to filter out other laser beams associated with a dual-pump CARS measurement that was being performed simultaneously. Reprinted with permission of the authors.

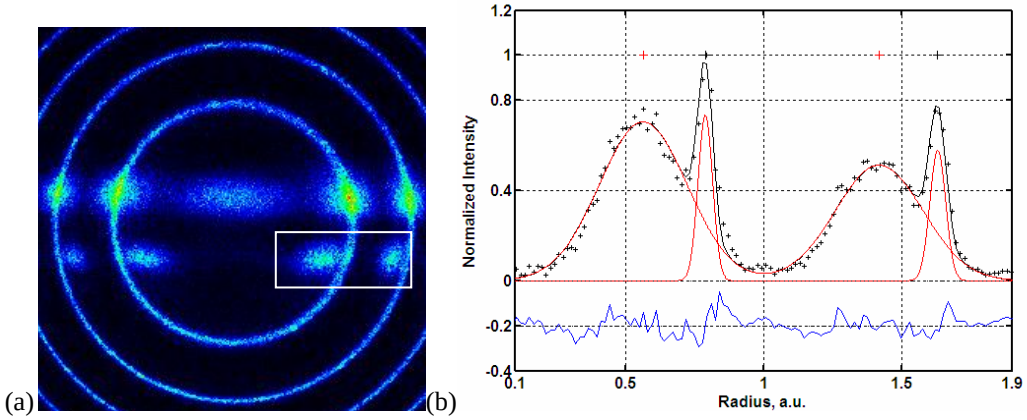

Figure 6.6. (a) Fabry-Perot interferogram of Rayleigh-scattered light obtained by laser beams from two different directions as well as laser-light, resulting in the circular pattern. (b) the linearized Rayleigh-scattered spectrum obtained from the boxed region in (a), showing best fits to the reference and Doppler-shifted light.[241] Reprinted with permission of the authors.

6.5 Rotational and Vibrational Temperature Measurements

Raman scattering is sensitive to individual molecular rotational and vibrational transitions. Since the population of these lines depends on (actually defines) the temperature, it is possible to measure rotational and vibrational temperatures from spontaneous Raman spectra. Figure 6.7 shows a typical Raman spectrum obtained in a hydrocarbon-air flame at high pressure.[247] A

pulse-stretcher was used to extend the duration of the 500-mJ, 532-nm pulse by nearly a factor of 10, thereby lowering the peak laser power to avoid laser-induced breakdown while maintaining high pulse energy to yield a sufficiently high signal-to-noise ratio.[247] This spectrum shows many temperature and concentration dependent features. The relative heights and shapes of the different bands depend on temperature and gas concentration. Modeling, calibration and analysis of such Raman spectra can yield rotational and vibrational temperatures as well as concentrations.

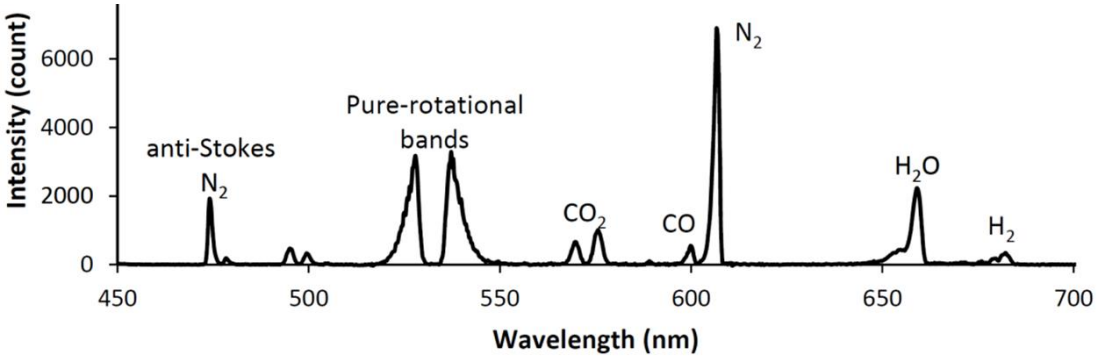

Figure 6.7. Five-hundred-pulse-average Raman spectrum in a high-pressure CH_4 air flame. The excitation laser wavelength was 532 nm. A 532 nm filter blocks Mie, Rayleigh and spurious laser scattering as well as some of the low-rotational-quantum-number rotational Raman lines. A subframe burst gating (SBG) technique was also used to subtract background emission from this spectrum.[248] Reprinted with permission of the authors and publishers. Combustion science and technology by TAYLOR & FRANCIS INC. Reproduced with permission of TAYLOR & FRANCIS INC. in the format reuse in a book/textbook via Copyright Clearance Center.

Several different strategies for temperature measurement based on spontaneous Raman scattering exist. Rotational temperatures can be measured from pure-rotational Raman scattering either using high-resolution or low-resolution detection, as indicated in Fig. 6.8.[249] The advantage of low-resolution detection is that the spectrum can be acquired simultaneously with the same instrument used to acquire multi-species spectra like that shown in Fig. 6.7. A disadvantage of this low-resolution technique is that many different species have similar pure rotational Raman shifts, so they overlap in the same spectral region close to the excitation laser. Such interferences from different species can lead to measurement errors. This technique works over a wide temperature range, including at room temperature. Alternately, rotational temperatures could be determined by resolving the rotational-vibrational Raman scattering, typically of N_2,[250] as is often done for CARS.[251] When flows are in rotational-vibrational equilibrium, it is more common to measure the temperature using vibrational bands, as described below, because they result in higher signal-to-noise ratios and consequently, more precise temperature measurements.

Vibrational temperatures can be measured from the relative heights of different vibrational Raman bands. A commonly used method compares the ratio of the Stokes to anti-Stokes (S-AS) vibrational Raman bands of N_2. [5,252-254] N_2 is often used because it is present in high concentration in many supersonic, hypersonic and combusting flows, resulting in adequate signal-to-noise ratio. Also, N_2 is used because it is relatively well understood and well resolved spectrally from other species. Recall from Fig. 6.1 that the anti-Stokes scattering originates from an excited vibrational state whereas the Stokes scattering can originate from the ground vibrational state. Thus, the integrated intensity of the anti-Stokes N_2 spectrum at 473 nm in Fig. 6.7 can be compared to the Stokes scattering at 607 nm. This ratio, which is a monotonic function of temperature, can be used to determine the temperature. Since this method integrates

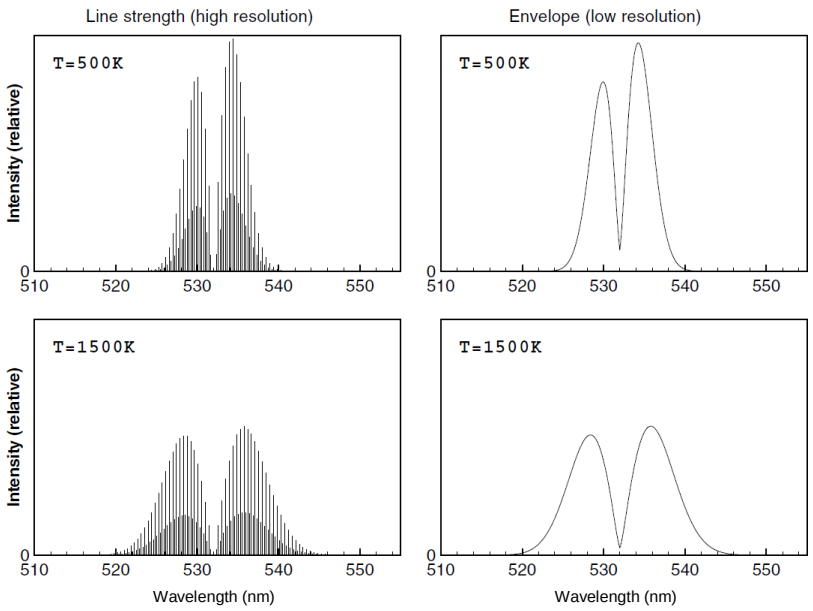

Figure 6.8. Theoretical calculation of the pure rotational Raman spectra of N_2 at two different temperatures and two different spectral resolutions, adapted from Ref. 249. © IOP Publishing. Reproduced with permission of the authors and of IOP Publishing. All rights reserved.

the signal intensity in the two different bands, it improves the signal-to-noise ratio, allowing single-shot determination of temperature. Single shot precisions of ~20% of the measured temperature have been obtained at several points along a line using this method.[252] This technique becomes insensitive to temperature below about 700 K because the low population in the excited vibrational state causes low signal-to-noise ratio.[5]

A second method of measuring the vibrational temperature is to spectrally resolve the different vibrational bands of a molecule such as N_2, though the individual rotational lines need not be resolved. The relative heights of the vibrational levels can be plotted on a Boltzmann plot or can be fitted spectrally to determine the vibrational temperature.[255] For example, Sharma and coworkers[255] used a KrF excimer laser operating at 248 nm to generate spontaneous Raman scattering in the Electric Arc Shock Tube (EAST) facility at NASA Ames Research Center. The EAST facility, normally operated as a shock tube, was fitted with a two-dimensional converging-diverging nozzle so that a shock reflection generated a high pressure (100 atm), high temperature (5600 K) reservoir of N_2 gas that expanded through the nozzle. The sudden expansion through

the nozzle results in vibrational-rotational nonequilibrium, which was monitored with Raman scattering. Measurements were performed at different distances downstream to study the evolution of the vibrational relaxation. Figure 6.9 shows a sample spectrum generated and spectrally fit to determine the rotational and vibrational temperatures. The vibrational temperatures were then plotted versus distance downstream in the flow so that different vibrational relaxation models could be tested.[255] Though not explicitly stated in the paper, the temperature measurement precision appears to be about 5%.

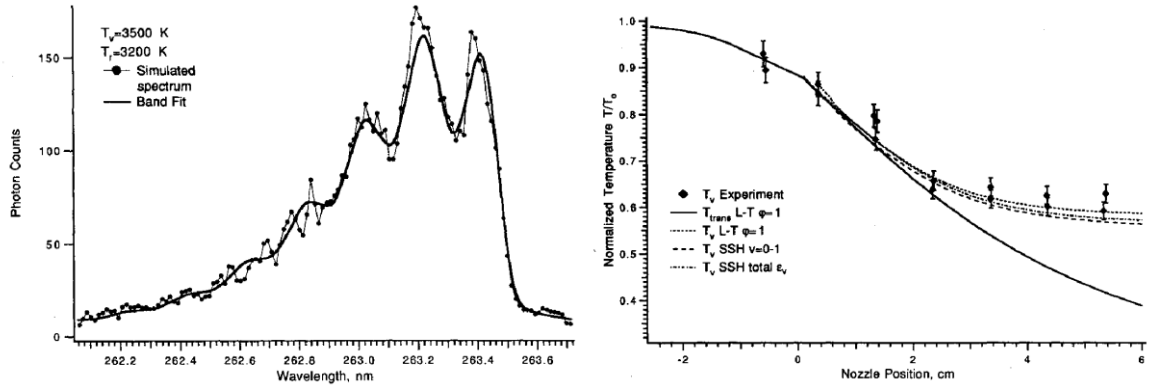

Figure 6.9. An experimental Raman spectrum of N_2, fitted for rotational and vibrational temperature (left), and resulting vibrational temperatures measured as a function of distance downstream of the nozzle (right), adapted from Ref. 255 with permission of the authors.

6.6 Species Concentration Measurement

Rayleigh scattering has been used in some specialized experiments for determining species concentration. For example, the Rayleigh scattering cross section for propane is 13.5 times larger than for air, allowing mixing to be quantified in propane/air jets.[256] However, *Raman* scattering is much more commonly used to measure species concentrations. Sandia National Laboratories have extensively used Raman scattering for major-species concentration measurements (along with Rayleigh and LIF measurements for temperature and minor-species concentration measurements, respectively).[155] This system uses a series of four frequency-doubled Nd:YAG lasers to produce temporally-stretched 1.8 Joule pulses which are focused to a 0.22 mm ($1/e^2$) diameter spot size. A separate laser excites LIF of CO. An imaging system directs the collected Raman/Rayleigh/LIF scattered light into the optical analysis system shown in the bottom-right panel of Fig. 6.10. The system contains two mechanical chopper wheels (one "slow" and one "fast") that are synchronized with the laser to transmit the signals while rejecting flow luminosity. It also has a transmission grating and multiple lenses, beam splitters and cooled (low noise) CCD cameras. This system images a 6-mm-long segment of the Rayleigh, Raman and LIF probe volume, allowing concentrations and temperature to be obtained along a line. The spatial resolution for the Raman measurements was ~10 pixels / mm along the 6-mm-long probe volume, though the actual spatial resolution was slightly worse due to optical distortions from the flame.[155]

A sample of the resulting concentration measurements are shown in Fig. 6.10. Raman has been used to measure N_2, O_2, CH_4, CO_2, H_2O and H_2 while CO was measured with two-photon LIF excited at 230.1 nm. Temperature was measured from the intensity of the Rayleigh-scattered light, using the ideal gas law to convert density to temperature as described above. The data are graphed versus temperature to show the correlation of species with temperature and to allow comparison with an unstrained flame calculation, shown in blue. The individual (red) data points correspond to different single pulses of the laser. Thus, these measurements are 'single shot' having been obtained with flow freezing (~100 ns) time resolution. Data such as these have been acquired at many locations in a variety of different flames, allowing the development of a large database of turbulent flames. The accuracy of the Raman concentration measurements varies from 2% to 10% of the measured concentration, while the precision (based on one standard deviation) varies from 0.7% to 7.5% depending on the species. The accuracy of the temperature measurement, based on Rayleigh scattering signal intensity, was reported to be 2% with a 1-σ precision of 0.75%.

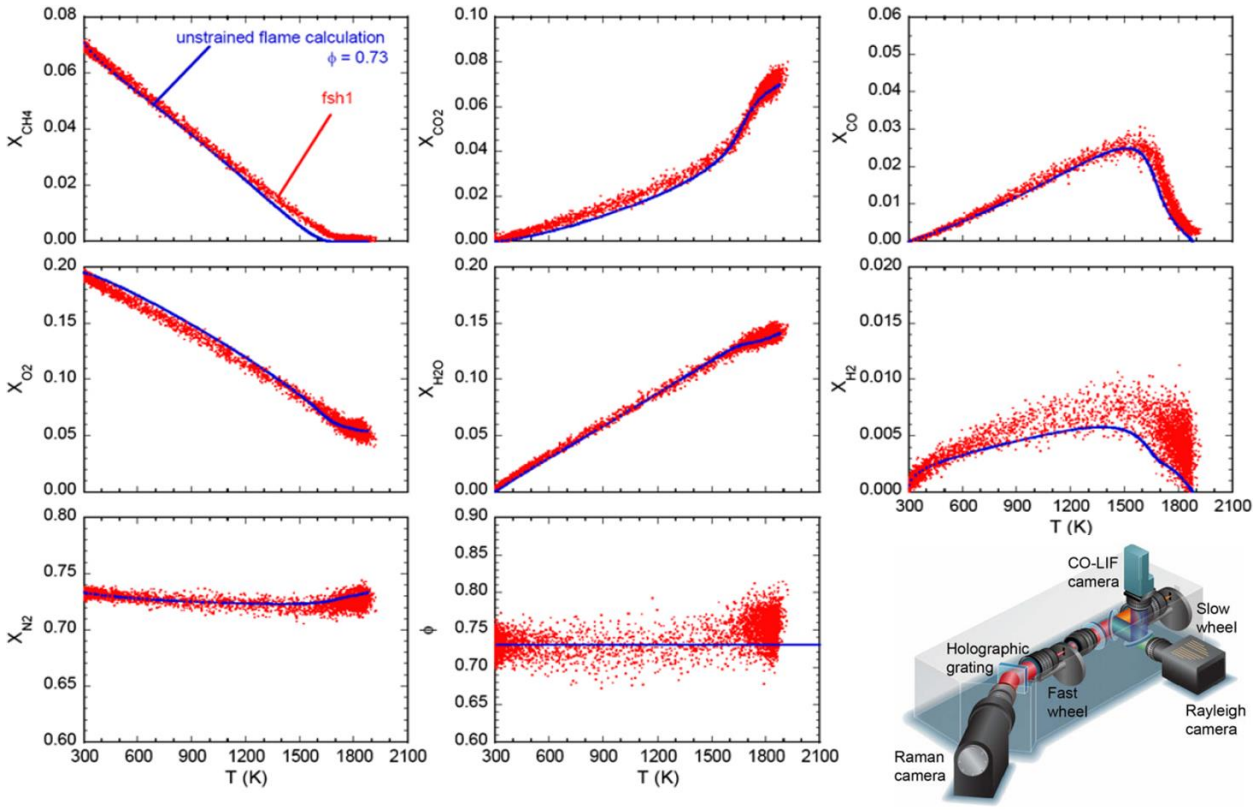

Figure 6.10. Scatter plots of mole fraction and equivalence ratio (ϕ) data at one location in an atmospheric pressure, methane-air flame compared with a calculation, and a schematic of the optical components associated with the collection and analysis of light from the Sandia Raman/Rayleigh/LIF imaging system (bottom right). Adapted from Ref. 155 with permission of the authors and The Combustion Institute.

7. Coherent Anti-Stokes Raman Spectroscopy

7.1 Introduction

Comprehensive reviews of the theory and application of Coherent anti-Stokes Raman spectroscopy, often called coherent anti-Stokes Raman *scattering*, or CARS, in a gas have been given by others.[5,109] A brief introduction and overview are provided herein. CARS is a non-linear optical process in which three laser beams interact with the gas generating a fourth, laser-like signal beam. The energy level diagram of this process (each arrow represents a change in state due to photon absorption, an up arrow, or emission, a down arrow, and the length of the arrow is proportional to energy change or, equivalently, photon frequency) is shown in Fig. 7.1

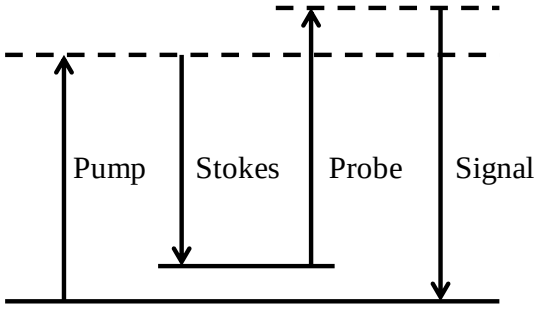

Figure 7.1. Energy level diagram showing the CARS process.

The pump beam and the lower frequency Stokes beam interact with the gas, a pump frequency photon is absorbed and a Stokes frequency photon is emitted coherently with the Stokes beam, and the gas is excited to a higher energy state via a state that in most CARS setups is a virtual state (although it could also be a real state). The difference between the frequencies of the upper and lower state, $\omega_{pump} - \omega_{Stokes}$, is called the Raman shift. A probe beam photon is coherently scattered from this excited state, shifted up in frequency by the Raman shift to form part of the signal beam, and the gas molecule returns to its original state. Total momentum as well as energy is conserved. Therefore, the momentum of the scattered photons equals that of the incident photons, leading to the following equation:

$$\overrightarrow{k_{pump}} + \overrightarrow{k_{probe}} = \overrightarrow{k_{Stokes}} + \overrightarrow{k_{signal}} \tag{7.1}$$

Since the *k*'s are the wave vectors (length proportional to photon frequency with direction the same as that of the beam), this equation allows the direction of the signal beam to be found from the directions of the pump, Stokes, and probe beams.

A physical interpretation of this process is that the interaction of the pump and Stokes beams establishes an optical fringe pattern in the gas. If the pump and Stokes frequencies are the same, as with a related technique called degenerate four-wave mixing (DFWM), this fringe pattern is stationary. In CARS, the frequencies are

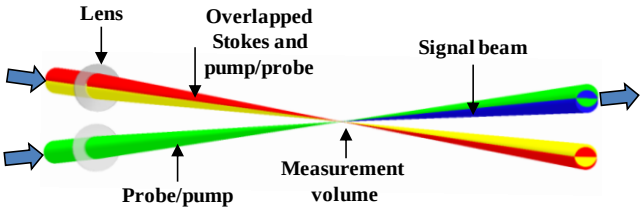

Figure 7.2. Planar BOXCARS beam geometry.

different and the fringe pattern moves across the interaction region, modulating the intensity at any particular point at the beat frequency, i.e., the Raman shift frequency. This moving fringe pattern excites a polarization response in the gas which acts as a moving grating from which a probe beam photon is scattered, in a manner similar to Bragg scattering, to form the signal beam photon. Since the grating is moving, the frequency of the signal photon is shifted relative to the probe photon by the Raman shift frequency. (An analogous effect occurs in an acousto-optical modulator where acoustical waves in a solid material, such as glass, form a moving grating of varying index of refraction, and incident laser light is coherently or Bragg scattered from this volumetric "grating" with its frequency shifted by the acoustical frequency.[257])

If the pump, probe, and Stokes lasers are all single frequencies, then the signal is also at a single frequency, as indicated in Fig. 7.1. If the pump and/or Stokes lasers are broadband lasers, while the probe is single frequency, then the signal is broadband also, and contains a spectrum that reflects the variation of CARS susceptibility of the molecules in the probe volume as a function of Raman shift. In many broadband CARS setups, the probe and pump frequencies are the same (derived from the same laser source). In the dual-pump CARS technique, [5,258] pump and probe frequencies are different and these two laser beams have interchangeable roles (each beam performs the role of pump in one CARS process and probe in a second CARS process). The signal is thus the coherent superposition of the signal from the two processes, generated over two different ranges of Raman shift. When the desired Raman shift is small, as in rotational CARS (i.e., when the transitions probed are pure rotational transitions, which differ by relatively small quanta of energy and are thus relatively closely spaced spectrally), the pump and Stokes beams can be derived from the same broadband laser while the probe beam is single frequency (dual-broadband CARS).[5]

Since CARS is a non-linear process (see Section 1.2) it requires high irradiance levels. Consequently, CARS signal in a gas is typically generated by focusing pump, Stokes, and probe beams, and overlapping them at their common focus. If the beams are initially separate and crossed at the common focus, the arrangement is called BOXCARS; if they lie in a plane (Fig. 7.2), it is called planar BOXCARS. In this arrangement the measurement volume is the small region of overlap of all three beams.

7.2 CARS Theory[5,109,257]

CARS, like Raman and Rayleigh scattering, arises because of time-varying polarization induced in the gas in the presence of electromagnetic radiation. CARS, specifically, arises due to the third order susceptibility, χ_{CARS}, for which the induced polarization is described as follows:

$$P^{(3)}\left(\omega_{signal}\right) = \epsilon_0 \chi_{CARS} E(\omega_{pump}) E(\omega_{Stokes}) E(\omega_{probe}) \tag{7.2}$$

The *E*'s are the complex electrical field amplitudes. This equation can be substituted into the wave equation relating the electrical field to the induced polarization and solved by integration along the direction of the signal beam. The CARS irradiance is thus:

$$I_{signal} \propto I_{pump} I_{Stokes} I_{probe} |\chi_{CARS}|^2 L^2 \tag{7.3}$$

L is the length of the measurement volume, i.e., the length of the region along which the pump, Stokes, and probe beams all overlap. Rigorous calculations of the CARS susceptibility require quantum mechanical treatments, but classical derivations are simpler to understand. The gas is modeled as a simple harmonic oscillator in which the variation of the normal coordinate, *Q* (intermolecular spacing in the case of vibrational states), with time is described by a second order linear ordinary differential equation, with a time-dependent forcing function proportional to the average over an optical cycle of the square of the electrical field. (Thus, the forcing term oscillates at the Raman shift frequency.) The constant of proportionality in the forcing term is proportional to $\left(\frac{\partial \alpha}{\partial Q}\right)_0$, and consequently to the Raman scattering cross section, where α is the optical polarizability of the molecule. The CARS susceptibility is found by solving for the time dependence of the normal coordinate, combining with Eqs. (6.1) and (6.2) for the polarization (from the chapter on Rayleigh and Raman scattering), and comparing with Eq. (7.2):

$$\chi_{CARS} \propto \frac{N\left(\frac{\partial \sigma}{\partial \Omega}\right)}{\Delta\omega\left(2-\frac{\Delta\omega}{\omega_v}\right)+i\left(1-\frac{\Delta\omega}{\omega_v}\right)\Gamma} \tag{7.4}$$

The susceptibility is proportional to the molecule number density, *N*, and the differential Raman cross section, $\left(\frac{\partial \sigma}{\partial \Omega}\right)$, and reaches a peak where the detuning, $\Delta\omega \equiv \omega_v - \left(\omega_{pump} - \omega_{Stokes}\right)$, approaches zero. The damping coefficient, Γ, determines the line width. A quantum-mechanical treatment yields the following equation:

$$\chi_{CARS} = \sum_j \frac{K_j \Gamma_j}{2\Delta\omega_j - i\Gamma_j} + \chi_{nr} \text{ where } K_j \propto N\Delta_j \left(\frac{\partial \sigma}{\partial \Omega}\right)_j \tag{7.5}$$

The index *j* refers to a particular transition and Δ_j is the fractional difference in the population of the two states of the gas between which a transition is taking place (the two real levels in the energy level diagram of Fig. 7.1); χ_{nr} is the non-resonant susceptibility, a nearly constant term for the CARS process in which all the states in Fig. 7.1, other than the ground state, are virtual states. The (real part of the) line shape in Eqn. (7.5) is a Lorentz function with full-width at half maximum equal to Γ_j. This line shape is the same as the (complex conjugate of the) line shape for the classical solution when the detuning is small relative to the vibrational frequency. The line width depends inversely upon the lifetimes of the two states involved in the transition, which depend upon the rate of collisions between molecules (collisional broadening). Light emitted by molecules in motion is observed at a slightly different frequency by a stationary observer by an amount proportional to the velocity component towards the observer. This effect, when averaged

over many molecules travelling in different directions, results in Doppler broadening. Since the distribution of molecular velocity components about the bulk mean in a gas in equilibrium is Gaussian, the line shape becomes a Voigt profile, a convolution between Gaussian and Lorentzian functions. At pressures much above atmospheric, additional line narrowing effects occur.

Since the CARS signal is proportional to $|\chi_{CARS}|^2$, a CARS spectrum reflects the populations of the molecular energy states involved in the transitions. Since these populations, in equilibrium, are related via the Boltzmann equation to the temperature, CARS can measure temperature. Integrated CARS signal is also strongly dependent upon number density and, in principle, could be used to measure density. This is not typically done because of experimental difficulties in maintaining a consistent geometry of the laser beams at the beam intersection. Small uncontrolled motions of the beams due to refraction in inhomogeneous gas fields, movements of the optical system, variation in the quality of the laser beams, etc., cause changes in signal intensity, and calibrations fail. However, where two gas species are resonant in a spectrum, the ratio of the population of one species to another may be found from the shape of the spectrum. Where only one species present is resonant, but χ_{nr} is known, the fraction of that species may be found from the relative amplitude of the resonant signal to the non-resonant "background"; however, χ_{nr} depends on the number density of all species present. If all species but one are resonant in the spectrum then the composition can be fully determined by reference to the non-resonant background.[259] Use of CARS as a diagnostic tool requires comparison of experimental and theoretical spectra.[260] Calculation of theoretical spectra is quite complex and numerically time-consuming: after computation of theoretical susceptibility, spectra must be convolved with laser line shapes and instrument probe function.[261]

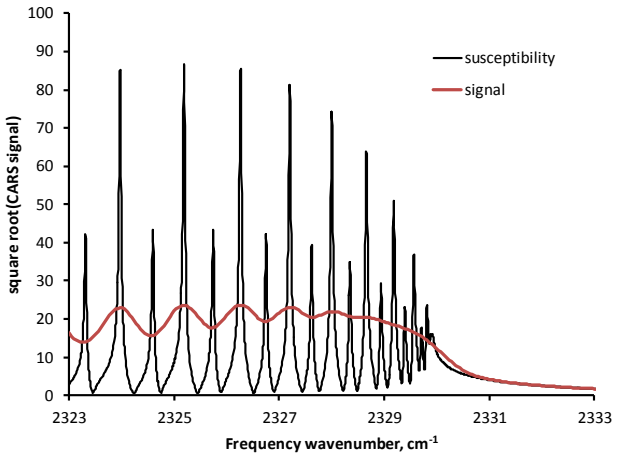

Figure 7.3. CARS N_2 Q-branch susceptibility and spectrum near band head at 1 atm., 1400 K.

Nitrogen is a very useful species for measurement of temperature since it is usually present in fuel-air combustion or hypersonic flows, and is readily probed by CARS. The band head of the N_2 Q branch is located at a Raman shift of 2330 cm^{-1} (units of inverse wavelength, proportional to frequency divided by the speed of light), and is readily accessible using available lasers. The Q branch occurs as a result of transitions between adjacent vibrational states ($\Delta v=+1$, where v is the vibrational quantum number) with no change in the rotational state ($\Delta J=0$, where J is the rotational quantum number). Figure 7.3 shows a portion of the N_2 Q-branch spectrum near the band head. Transitions are between v=0 and v=1and each peak corresponds to a different J value.

Since rotation of the molecules affects the energy associated with a given vibrational state, the energy difference between v=0 and v=1 (at given rotational level) is a function of the rotational level. Two spectra are shown in this figure – the first is the CARS susceptibility and the second is a computed typical broadband CARS spectrum formed by convolution of typical laser line shapes and a typical instrument function with the susceptibility.[261] As may be seen, line shapes are typically not fully resolved in experiments.

Figure 7.4 shows the sensitivity of the signal spectrum to (a) temperature and (b) concentration. The calculations are for (a) air and (b) either air (79% N_2) or 10% N_2, 21% O_2, 69% H_2O, with a pressure of 1 atmosphere. The CARS signal strength varies strongly with temperature, partly through the effect of temperature on density (N) via the N^2 dependence of the CARS susceptibility. By using the Sandia CARSFT code,[260] the pressure and temperature dependence was determined to be proportional to $p^2T^{-3.5}$ at moderate to high pressures.[262] However, the shape of the spectrum also changes. At low temperature, only one vibrational band is present, associated with v=0 to v=1 transitions, and is relatively narrow (because fewer J levels are occupied). At the higher temperatures, "hot" bands are present also, associated with v=1 to v=2 and v=2 to v=3 transitions, and more J levels are populated. As the fraction of N_2 is reduced, the amplitude of the band structure becomes smaller relative to the non-resonant background, and sensitivity to N_2 is lost for concentrations less than a few percent. This lack of sensitivity below a few percent is typical and prevents measurement of minor species, although a number of CARS techniques, for example *resonance* CARS (e.g., Ref. 263), have been developed to circumvent this limitation.

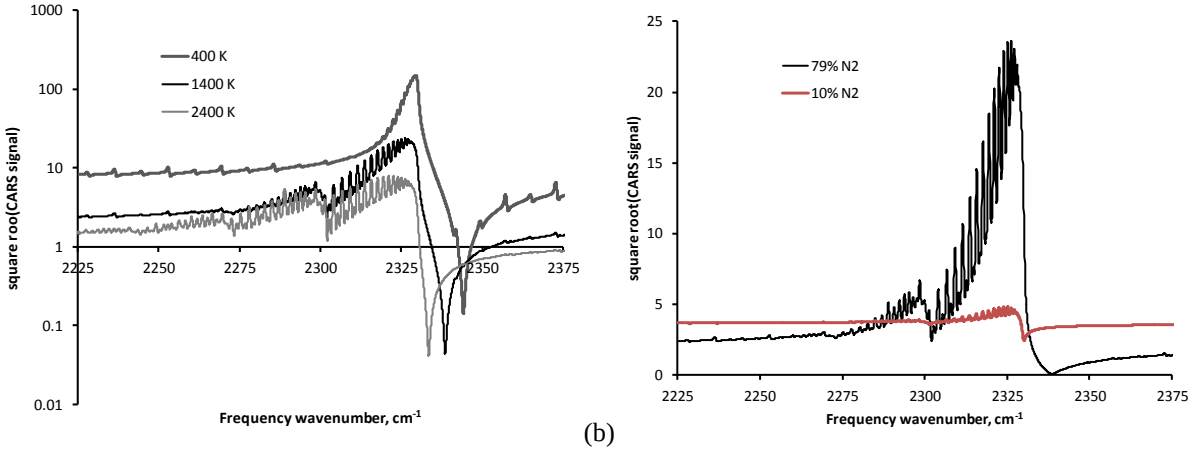

Figure 7.4. Effects of (a) temperature and (b) concentration on the CARS N_2 Q-branch spectrum.

7.3 Ultrafast CARS

Ultra-fast techniques have been surveyed by Roy et al.[264] The CARS technique as described above is a steady-state process involving the mixing of four beams simultaneously present. For given laser energy available in the pump, probe, and Stokes laser beams, the energy in the signal beam is proportional to t^{-2}, where t is the time over which the measurement is made.

Nanosecond (ns= 10^{-9} s) CARS is performed with Q-switch pulsed lasers where the pulse energy is distributed over 5 ns to 10 ns, at a pulse rate on the order of 10 Hz. There are many 10's or 100's of thousands of Raman frequency cycles during each laser pulse, so that CARS is effectively a steady-state process. However, with the advent of femtosecond (fs= 10^{-15} s) lasers (e.g., titanium-sapphire), very short pulse widths of order 10^{-14} seconds are possible at high pulse repetition rate (1 kHz or more), and the pulse width is less than the period of a Raman cycle. Due to the t^{-2} scaling, strong signal energy is available with modest pulse energy.

The theory of fs CARS is different from ns CARS since a steady state problem is replaced with an impulsively initiated, time-dependent one.[265] First, a polarization grating is established in the gas by the interaction of pump and Stokes beams. This grating evolves in time through rotational-vibrational relaxation and then, after some delay (typically up to several hundred picoseconds in measurement applications), a signal is generated by scattering the probe pulse off the grating. By making measurements at different probe delays the relaxation of the grating, which carries with it an imprint of the vibrational and rotational state of the probed molecules, may be observed. "Chirping" techniques have been developed where the probe beam is broadened both temporally and spectrally in such a way that the frequency of the probe varies with time. The temporal relaxation is thus mapped into frequency space, obtained in a single laser pulse, and may be analyzed with an optical spectrometer.[266]

Picosecond (ps = 10^{-12} s) CARS employs mode-locked solid state lasers with pulse lengths on the order of 10 ps and has characteristics of both ns and fs CARS. As with fs CARS, generation of the grating by the pump and Stokes beams, and scattering of the probe to form the signal, are typically separate steps. However, the probe pulse is still relatively long compared with the Raman cycle period, and the signal contains an optical spectrum similar to that of ns CARS.[267] An advantage of ps CARS over ns CARS is that the ps pulses required to obtain adequate signal-to-noise ratio CARS spectra are better suited to pass through commercially available optical fibers without damaging the fibers.[268] Both fs and ps CARS have the potential advantages over ns CARS of much higher data (pulse) rates and the absence, when the probe is delayed relative to the pump-Stokes laser pulses, of non-resonant background effects. Another advantage of fs CARS is simpler theoretical modeling, since few or no collisions occur in the time of the measurement (negligible collisional effects).[264]

7.4 Advantages and Disadvantages of CARS for probing Supersonic, Hypersonic and Nonequilibrium Flow

In hypersonic propulsion systems (scramjets), flow velocities are supersonic in inlets and nozzles, and may be supersonic or a mixture of subsonic and supersonic in the combustors. In combustors, pressures are roughly one atmosphere while temperatures are similar to those of low speed combustion. Thermal nonequilibrium (not typically present in low speed combustion) as well as chemical nonequilibrium can be present due to the short flow through time (on the order of milliseconds). CARS has several advantages in this application. The signal comes as a laser

beam, which means that it can be collected through a relatively small aperture and may be separated from non-coherent interferences by spatial filtering. This is particularly useful in an engine combustor where there may be emission from the gases and thermal radiation from the wall, and where, for structural reasons, it may not be possible to incorporate large windows. Typical CARS measurements are spatially and temporally resolved, with ~1.5 mm long and 50 μm diameter measurement volume, and a 10 ns time scale. CARS is able to non-intrusively measure local temperature and composition. Since the Q-branch spectrum reflects the rotational-vibrational state of the molecule, the populations of these states may be directly determined, which is useful when thermal equilibrium (and therefore a single "temperature") does not exist.

CARS has been used much less frequently in hypersonic freestreams, where temperatures and pressures can be very low. Due to the previously-mentioned $p^2T^{-3.5}$ scaling of the CARS signal, the signal to noise ratio may be low. At low temperatures only the vibrational ground state and far fewer rotational states of molecules are populated. Vibrational CARS (e.g., of the N_2 Q-branch) then depends upon measuring high resolution spectra of the rotational structure of the "cold" band near the band head, which depends upon the pressure-dependent collisional effects on line shape, as well as temperature. Measurements of both pressure and temperature, at pressures down to about 0.1 atm., have been made in an underexpanded supersonic jet using this approach. [269] If the v>0 bands are populated at low rotational temperature (vibrational nonequilibrium), this can be easily measured. Alternatively, pure rotational CARS ($\Delta v=0$, $\Delta J=\pm 2$) is sometimes used at low temperatures since the lines have greater separation than in the Q-branch, but no information on the vibrational state is obtained.[270]

In nonequilibrium flows CARS has a significant advantage that it can simultaneously monitor multiple individual state populations. Thus non-Boltzmann distributions can be probed, as in the examples below. Using vibrational broadband CARS, separate rotational and vibrational temperatures can be determined from CARS spectra.

CARS has some disadvantages compared to other measurement techniques. It typically measures at only a single point, and so does not typically provide simultaneous information at multiple spatial locations. Instead, the probe volume is typically scanned around the flow allowing time-averaged spatial properties to be measured. The data rate is low in ns systems (order 10 Hz) so that in pulsed hypersonic facilities only one single measurement is obtained per facility run. Also, its ~1.5 mm long probe volume can be too large in certain applications where it is desired to resolve small length scales such as shock waves, shear layers or turbulent eddies. Many of these limitations are being overcome with fs CARS where 1D[271] and 2D[272] imaging have been demonstrated recently with smaller probe volumes and data acquisition rates in the kHz regime have been achieved.[264] CARS requires optical access on two sides of the flow, which may limit application in some facilities. The experimental setup for CARS, involving two or three pulsed laser systems along with large spectrometer(s), is relatively complicated and time consuming to set up. Furthermore, the nonlinear nature of the theory of CARS complicates the interpretation and analysis of the resulting spectra. However, with the combination of accurate

and precise temperature and multi-species measurement capabilities, CARS is used in many supersonic, hypersonic, and nonequilibrium flow applications.

7.5 Mole Fraction and Nonequilibrium Temperature Measurement

Extensive dual-pump CARS measurements have been made in a dual-mode scramjet burning hydrogen.[273] The experiments were conducted in a facility which provided electrically heated clean air to the scramjet combustor via a Mach 2 nozzle. The CARS lasers, which were located outside the scramjet lab, consisted of an injection-seeded Nd:YAG, frequency doubled to 532 nm, an in-house broad band dye laser (Stokes laser) centered around 603 nm with FWHM of 10 nm, and a commercial narrow-band dye laser centered around 550.5 nm. Beams were relayed to the experiment via a translation system that could move the measurement volume and through special slotted windows in the scramjet. Beams were focused and crossed in the scramjet in a planar BOXCARS arrangement (Fig. 7.2) to form the measurement volume. The signal beam was transmitted out of the scramjet, recollimated, separated from one of the pump beams, relayed to a 1 m spectrometer, then imaged onto a cooled CCD array with 1340×100 pixels. The measured spectra had background subtracted and were normalized by a CARS spectrum in argon, which has no resonances, to remove the spectrum of the broad-band laser. The resulting spectra were fitted to theory, using the Sandia CARSFIT code[260] to generate the theoretical spectra and an in-house fitting code[261] to do the fitting, resulting in temperature standard deviations of ~3%.[274] The fitted parameters included vibrational temperature of N_2, a single rotational temperature for all resonant species, and mole fractions of N_2, O_2, and H_2.

Vibrational nonequilibrium was observed in the flow at the exit of the nozzle and in the freestream of the scramjet flow, which could be fitted to around 1200 K in vibrational temperature of N_2 and 1000 K in vibrational temperature of O_2, while the facility air stagnation temperature was 1200 K and the nozzle exit static temperature was around 680 K.[275] The low rate of relaxation of N_2 vibrational energy relative to rotational (which rapidly comes into equilibrium with translational), and the higher but still relatively low rate for O_2 is consistent with known rates in the literature.[276] Measurements in which a varying amount of steam was added to the air flow are consistent with the known effect of water vapor to promote equilibrium.[277] Figure 7.5 shows the effect of water vapor in the dual-pump CARS spectrum; notice the large effect of steam on the hot band of the N_2 spectrum and a lesser effect on the hot band of the O_2. The intensity of these bands is proportional to the population difference between the v=1 and v=2 vibrational states (roughly proportional to the population of v=1 since the population of v=2 is small).

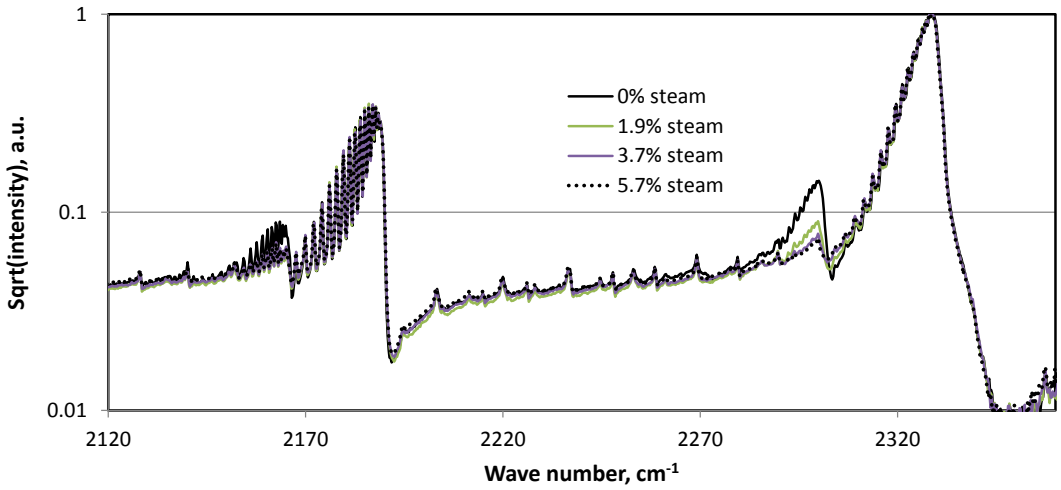

Figure 7.5. Experimental dual-pump CARS spectra in a Mach 2 flow with varying amounts of steam added to the air. The N_2 Q-branch is on the right and the O_2 on the left. Reprinted from Ref. [275] with permission of the authors.

Figure 7.6 shows some typical (averaged) measured spectra and fits to theory in the scramjet. Spectrum (a) was in the freestream air of the flow and is shown with a fitted rotational temperature of 923 K and N_2 vibrational temperature of 1133 K. N_2 and O_2 Q-branch resonances may be seen. Spectrum (b) is in the combustion plume and shows H_2 rotational (S) lines as well as the aforementioned Q-branches, with fitted rotational and vibrational temperatures of 1588 K and 1766 K, respectively. Figure 7.7 shows contour maps of vibrational temperature in the combustor operated in the "scram" mode. The wireframe represents the corners of the flow path; a single hydrogen injector is located at the downstream end of the small ramp visible on the top surface of the flow path. Flow enters at Mach 2 from the test facility nozzle and is from left to right. The development of the combustion may be seen; combustion is initiated on the top of the plume of hydrogen, near the fuel injector, and wraps around and engulfs the plume further downstream.

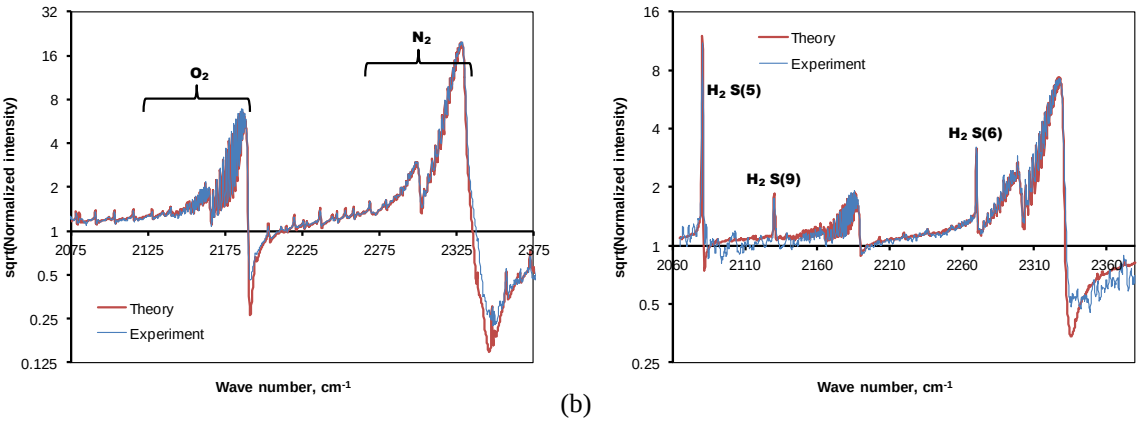

(a) (b)

Figure 7.6. Typical fits of theory to experimental dual-pump CARS spectra in a dual-mode scramjet: (a) freestream, (b) combustion plume. Reprinted from Ref. [275] with permission of the authors.

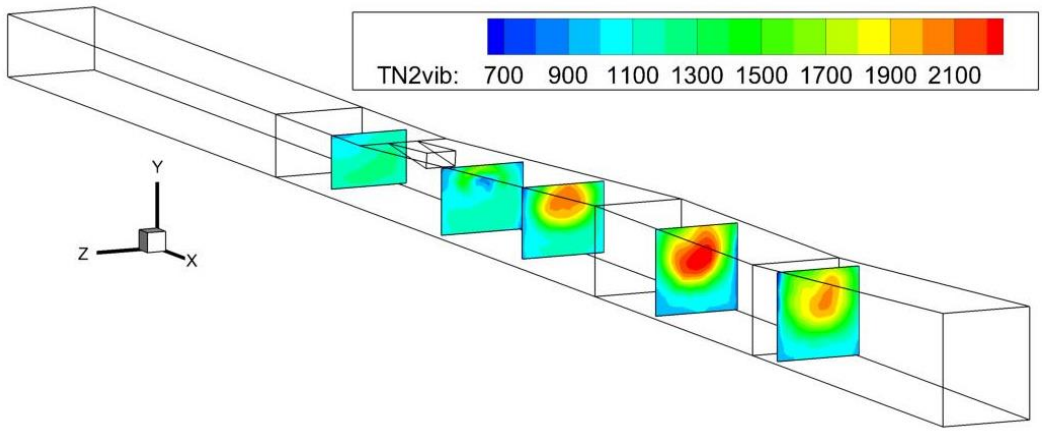

Figure 7.7. Contour plots of CARS-measured mean vibrational temperature in a dual-mode scramjet. Reprinted from Ref. [273] with permission of the authors.

Simultaneous with the temperature measurements, species concentrations were also determined from CARS data. The concentration information was derived from the relative intensity of the different resonant features in the CARS spectra, comparing to the intensity of the nonresonant background, and considering that the mole fractions must sum to one.[259] Figure 7.8 shows CARS mole fraction measurements obtained at the same conditions as Fig. 7.7. The mole fraction is uniform air in the first plane at the left of each of the figures. Evidence of the cold H_2 fuel jet is seen in the temperature map (Fig. 7.7) and all three mole fraction maps in the second plane, which is located just downstream of the fuel injector (Fig. 7.8). As the fuel jet spreads spatially and is consumed by combustion, the presence of N_2 in the center of the downstream fuel plume shows evidence of fuel-air mixing. However, the O_2 mole fraction does not track exactly with the N_2 because it is reacting with the H_2. Not until the final plane at the right side of each figure, when all the H_2 is consumed, does the O_2 penetrate to the center of the duct, in the wake of the fuel plume.

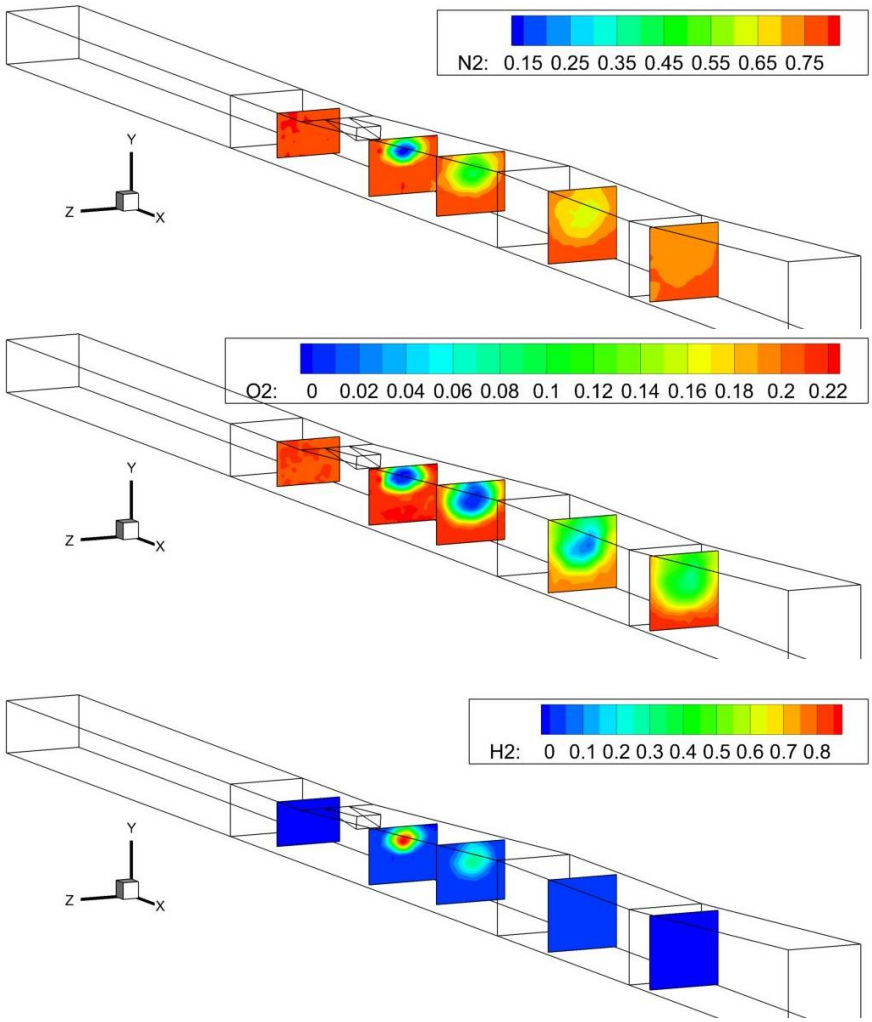

Figure 7.8. Contour plots of CARS-measured mean mole fractions of N_2 (top), O_2 (middle) and H_2 (bottom) in a dual-mode scramjet at the same conditions as Fig. 7.7.[273] Reprinted from Ref. [273] with permission of the authors.

7.6 Measurement of non-thermalized population distributions using CARS

Nonequilibrium flows sometimes result in non-Boltzmann distributions, for example among rotational or vibrational states. Montello et al.[278] used picosecond CARS to probe non-thermal vibrational distributions in N_2 generated in low pressure (100 Torr) N_2 and air pulsed discharges. They used a 150 ps duration, frequency-doubled Nd:YAG laser to generate the two green pump beams. The Nd:YAG laser also pumped a red broadband dye laser for the Stokes beam. These frequencies were chosen to probe the Q-branch Raman spectrum of N_2. The CARS signal was dispersed on a spectrometer, allowing instantaneous quantification of the N_2 vibrational distribution function (VDF). By varying the time between the CARS acquisition and the pulsing of the plasma discharge, the time evolution of the VDF could be studied.

Figure 7.9(a) shows vibrational N_2 CARS spectra obtained at different times after the beginning of the ~100 ns duration pulsed discharge. The narrowness of the bands indicates a relatively low rotational temperature, compared to the VDF. The populations of the excited vibrational levels are observed to increase with time (though the rotational distribution stays relatively constant). Vibrational levels from 0-9 were observed to have measurable population. When the vibrational populations are graphed with respect to vibrational quantum number (Fig. 7.9(b)) a thermalized population distribution would appear as a nearly straight line on this semi-log plot. Instead, departure from the Boltzmann distribution is observed, as evident from the non-linear trends in the data. A theoretical model captures much of the nonequilibrium physics occurring in this plasma.[278]

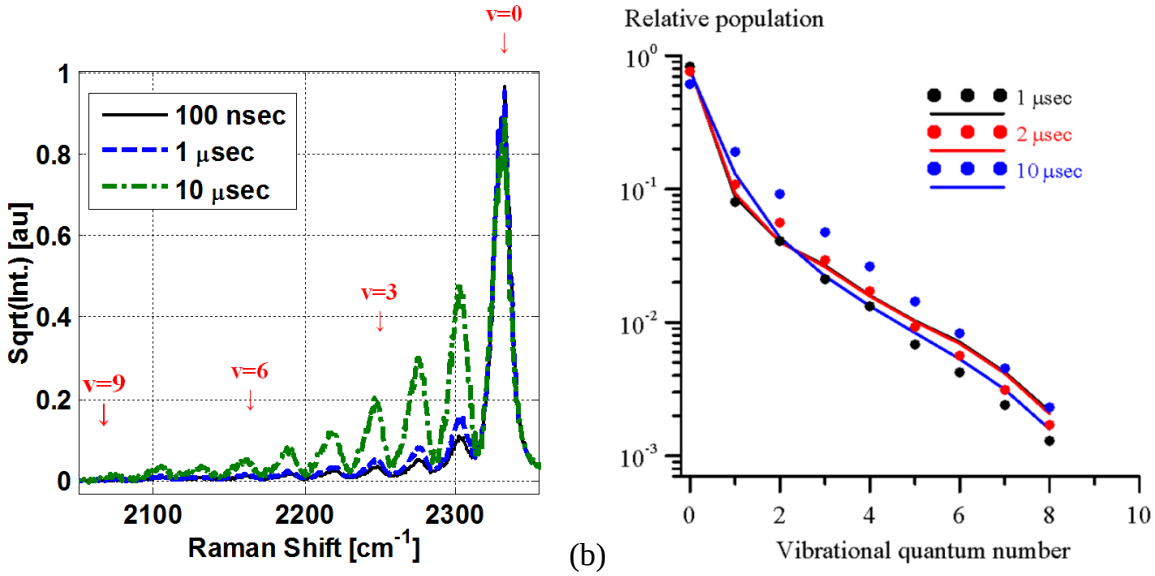

Figure 7.9. (a) N_2 Q-branch CARS spectrum obtained in a pulsed discharge operating with 100 Torr of N_2 shown for three different measurement times after the beginning of the ~100 ns discharge pulse. (b) Experimental and predicted vibrational energy level populations based on (a), showing non-thermal vibrational distributions which evolve with time. Reprinted from Ref. [278] with permission of the authors.

7.7 CARS summary

In summary, CARS is a powerful technique for simultaneously and quantitatively measuring multiple flow parameters in gas flows with thermal and/or chemical nonequilibrium. If the gas is in thermal equilibrium, CARS can be used to measure temperature; if not it can provide information on rotational and vibrational (for rotational-vibrational CARS) state populations, allowing separate determinations of rotational and vibrational temperature or rotational and vibrational distribution functions in non-thermalized flows. It also can be used to quantify the relative concentration of the species probed. It is spatially and temporally resolved, with a short measurement time (sub-ps to 10 ns) and a measurement volume that is typically on the order of 1 mm long. Nanosecond CARS is limited by available lasers to measurement rates of about 10 Hz, but femtosecond CARS data rates are often 1 kHz or more. Nanosecond CARS is a well-

established technique, picosecond and femtosecond CARS in gases is quite recent, due to the advent of suitable lasers, and techniques are still under development. The primary limitations of state-of-the art CARS systems include its complexity (which has meant relatively few applications to large-scale test facilities), the fact that measurements are pointwise and not planar or volumetric, and (for nanosecond CARS) the low data rate. Other issues include sensitivity to optical misalignment due to vibrations or refractive index variations along the beam path, and lack of spectral and collision-rate modeling for some species.

8. Other Molecular-Based Measurement Techniques

8.1 Introduction

Many different surface-based, probe-based and particle-based instruments have been used to study nonequilibrium hypersonic flows. However, this manuscript focuses only on molecular-based measurement techniques. Optical emission spectroscopy, absorption spectroscopy, Raman scattering, Rayleigh scattering, laser-induced fluorescence (LIF) and coherent anti-Stokes Raman spectroscopy (CARS) are some of the most commonly used techniques, and for this reason have been detailed in the preceding sections. This section briefly describes additional molecular-based measurement techniques that have been used, or that show some promise for use, in studying nonequilibrium hypersonic flows.

8.2 Interferometry

Interferometry uses interference of light to measure small changes in optical path length. Variation in gas flow properties along the optical path cause the index of refraction to vary, which generates these path length changes relative to a reference path. The two paths are then aligned onto a one- or two-dimensional detector where interference (or a so-called *interferogram*) is observed. This method is very sensitive because it can measure optical path differences that are fractions of a wavelength of the light from which they are generated.

In fluid mechanical applications, interferometry is usually used for flow visualization or to measure the gas density. The gas density is related to the index of refraction through the Gladstone-Dale equation:

$$n - 1 = K\rho \tag{8.1}$$

where n is the index of refraction, ρ is the density and K is the Gladstone-Dale constant, which depends on the gas and the wavelength of light. The Springer Handbook of Experimental Fluid Mechanics recently reviewed applications of various types of interferometry to fluid mechanics.[230] These include Mach Zehnder interferometry, holographic interferometry, shearing interferometry and others. The different interferometric methods can be sensitive to the density or the gradient in density.[230] Interferograms typically have light and dark fringes, which correspond to interference in the light caused by index of refraction variations introduced to one

of the paths. Sometimes, to enable post-processing, the optics are purposely misaligned producing a series of mostly-parallel sinusoidal fringes that act as a spatial carrier frequency allowing Fourier transforms to be used in post processing. Such interferograms are called *finite fringe interferograms* (as opposed to *infinite fringe interferograms* wherein the two paths are precisely aligned).

As a path-averaged measurement technique, most interferometry techniques require experimental methods and/or analysis to determine spatially-resolved information. If measurements along multiple lines of sight can be obtained, tomographic reconstruction can be used to deconvolve spatial information. Or, in axisymmetric flows, an Abel inversion can be used, as described previously. However, in the general case of 3D turbulent flows, these approaches are challenged by the short spatial and temporal scales of the experiments, which require many simultaneous high-resolution views from different angles. While time-averaged measurements in such turbulent flow fields are possible, it is more difficult to use these methods to resolve small temporal or spatial scales.

Interferometry is particularly useful in luminous high-enthalpy flow facilities, where spectral, spatial and temporal discrimination can be used to obtain the interferograms while rejecting flow luminosity. Interferometry was used extensively to study nonequilibrium hypersonic flows several decades ago. See, for example, the use of Mach-Zehnder interferometry to study the effect of nonequilibrium flow on the shock stand-off distance and post-shock density field.[279] More recently, holographic interferometry has been used in expansion tube facilities which are simply too luminous to use other techniques such as laser-induced-fluorescence. In one experiment,[280] the 532 nm and 355 nm outputs from an Nd:YAG laser were used to produce two simultaneous finite fringe interferograms in air passing over a cylinder at 12 km/sec in the X1 superorbital expansion tube at the University of Queensland, Australia. Both holographic finite fringe interferograms were acquired on the same photographic plate. After reconstruction, a Fourier transform method was used to process the interferograms. In this experiment the fringe shift is sensitive to both the density and the electron concentration, necessitating the two measurements to determine the two properties. Density and electron concentration maps were determined from the interferograms.[280]

8.3 Background Oriented Schlieren (BOS)

A relatively new measurement technique that is sensitive to density (through index of refraction gradients) is known as Background Oriented Schlieren (BOS).[281,282] BOS uses a CCD camera equipped with a lens to image a flow placed in front of a *background* consisting of a random dot pattern (or other[283,284] random pattern). A *reference* image of the background pattern is acquired with the flow absent and then a second image is acquired with the flow present. Refractive index gradients cause the dots to move slightly from one image to the other. The pair of dot pattern images is processed using particle-image velocimetry (PIV) software to recover

the path-integrated light deflections (pixel shifts) caused by the refractive index (density) gradients.

To obtain the highest possible spatial resolution, both the dot pattern and the flow disturbance should be in crisp focus. This suggests the use of small lens apertures to obtain a large depth of field. To obtain maximum sensitivity, the flow disturbance should be located as close to the camera lens as possible.[285] Since it is difficult to achieve a long enough depth of field to optimize both of these requirements, in practice, the object is usually put closer to the background dot pattern, for example from 0.5 to 0.875 of the way from the camera to the background pattern.[285, 286] Also affecting spatial resolution are the camera pixel size, the resolution and quality of the background pattern used and the interrogation window size used in image processing.

In a two-dimensional flow, the pixel shifts can be used to directly compute the density gradient and thus the density field.[285] In an axisymmetric flow, the density gradient varies along the optical path and additional processing of the data is required to make quantitative measurements. In such axisymmetric cases, an Abel or Radon inversion can be used to compute the density field, for example in the supersonic flow over a cone at zero degrees angle of attack.[287] In non-axisymmetric flows, tomography using multiple camera views is required to obtain density information.[285] The multiple views can either be obtained using a single camera that observes the flow from different angles at different times, resulting in time-averaged measurements,[285] or by using multiple cameras to take many simultaneous images, providing time resolution, which is a current research topic. Since BOS measures gradients and is thus a relative measurement technique, the density in one point in the flow must be known or estimated to obtain the density field. BOS has the advantages of being a low-cost technique and being able to provide both qualitative flow visualization and quantitative measurements for large fields of view. One disadvantage is that BOS does not produce real-time visualization and measurement results since the raw images require processing. Also, as a tomographic technique using a limited number of views, it has much lower spatial resolution than laser-sheet based techniques such as planar laser induced fluorescence, at least in unsteady flows where it is impractical to have a large number of views.

8.4 Electron-Beam Fluorescence

In low-density ($< 10^{16}$ molecules/cm^3) hypersonic flows, electron beam fluorescence is an attractive measurement approach.[288] An electron beam can be directed into the flow to excite a line, or swept through the flow to stimulate fluorescence in a plane. Multiple species, such as NO and N_2, can be excited and detected at different wavelengths. The fluorescence signal, if quenching is negligible, can be related to species concentration. Decades ago, density and temperature were measured in hypersonic boundary layers using electron beam fluorescence.[289] More recently, electron-beam fluorescence has been used to distinguish rotational and vibrational temperatures by spectrally resolving the emitted fluorescence, as well as to measure the gas

velocity from time-of-flight measurements, using a technique similar to that shown in Fig. 5.10.[288] However, at higher pressures, several problems complicate the use of electron-beam fluorescence. First, quenching becomes significant, complicating interpretation of concentration data and minimizing fluorescence lifetimes used to obtain flow tagging velocity. Second, the beam begins to disperse at higher densities, preventing measurement in a line or plane. Finally, excitation from scattered electrons becomes significant at higher pressures, which complicates interpretation of the images. Nonetheless, the electron beam fluorescence method has been shown to be useful in a wide variety of low-pressure hypersonic flows and even has potential for measurements in flight. [290,288]

8.5 Degenerate Four-Wave Mixing (DFWM)

Like CARS, Degenerate Four-Wave Mixing (DFWM) is a nonlinear, four-wave mixing measurement technique that involves the crossing of three laser beams to generate a fourth beam that is detected. DFWM's three input laser beams are all of the same color (degenerate) and are usually tuned to an absorption in the atom or molecule being probed. The signal beam from DFWM measurements is typically analyzed in the spectral domain using scanned or broadband lasers to measure a spectrum of signal intensity versus wavelength. DFWM has been used to measure gas concentration, temperature and velocity.[5] Compared to LIF, it has an advantage for measuring species concentrations because it is relatively insensitive to collisional quenching, owing to the fact that it is an absorption-based technique (not depending on fluorescence).[291] Since each beam is resonant, it is also relatively sensitive and can be used for detecting minor species.[5] Since the DFWM signal is a laser-like beam, it is suitable for studying luminous flows since background radiation can be spatially filtered with an aperture. DFWM is usually implemented as a single-point measurement, though it has been extended to line and 2D imaging applications.[5] The main drawbacks of DFWM are that it is more difficult to align and implement than LIF, it has much lower spatial resolution than LIF (because of its elongated probe volume), it is sensitive to absorption of the laser beams, it is sensitive to saturation of the molecular transitions, and it requires very high beam quality to obtain 2D images.[5] DFWM temperature measurements in a flame have reported accuracies and precisions more than a factor of two worse than CARS[292,5] while also having a larger probe volume.

8.6 Laser-Induced Thermal Acoustics (LITA)

Another four-wave mixing technique, laser-induced thermal acoustics (LITA), uses two pump beams to generate acoustic waves that scatter a probe laser into a signal beam that is detected.[293] The two pumps and probe can be the same wavelengths, in which case it is also DFWM. Or, the probe beam can be a different wavelength than the pumps, which reduces light interferences from the incident, high-powered pump beams. Whereas the signal beam from the DFWM techniques described in the previous section is usually analyzed in the *spectral* domain, LITA usually uses the *time* domain (signal beam intensity versus time) to measure gas velocity, speed of sound (which can be converted to temperature if the gas composition is known)[293,294]

and gas pressure.[295] In the time domain, the signal intensity is characterized by a damped oscillation, which can have beat frequencies containing the velocity and temperature information. Velocity and temperature accuracies and precisions on the order of 1 m/s and 1 K, respectively, have been reported in air flows.[294,296] These accuracies and precisions are the best reported in this manuscript for these parameters. LITA is usually implemented as a single-point, single-velocity-component measurement. The main limitations of LITA are its relative complexity and that the measurements are obtained over relatively long probe volumes – on the order of 1 to 2 cm. While this is much longer than most turbulent length scales occurring in hypersonic flows, it can be sufficient to probe laminar flows if the probe volume is oriented with its long axis oriented perpendicular to the steepest gradients in the flow.

9. Conclusions

This manuscript has described numerous molecular-based measurement techniques that are potentially applicable to the investigation of hypersonic nonequilibrium flows. One might ask, *"Which technique is best?"* or *"Which one should I use?"* The answer to the first question is that no one is best. The different techniques measure different properties in different ways and have relative merits. In addition, flow conditions and facility constraints may prevent application of specific measurement techniques. The answer to the second, more important question, depends on many factors. It depends on the measurement requirements as well as the past experience of the research team. It depends on the available equipment, the budget for new equipment and the time frame available to make the measurement. Some techniques, such as CARS, require a year or years of training to gain enough experience to apply the technique expertly. Dual-pump CARS requires home-built equipment (i.e. a broadband dye laser) as well as two commercially available lasers, a spectrometer, a low noise CCD camera, and other equipment. It is therefore relatively time consuming and expensive to set up. If a researcher or research team has experience with similar technology (for example Nd:YAG lasers, dye lasers, CCD cameras), then the work will progress faster. Less complicated (easier to set up and to understand) methods might yield usable results in a shorter time frame. These practical issues are certainly important, but a major consideration in planning an experiment is tailoring the chosen technique to the measurement requirements, the characteristics of the facility and the expertise of the scientist or engineer performing the experiment.

A measurement campaign should begin by answering the following questions, for example by interviewing the final "customer" of the data:

- What parameter(s) need to be measured?
- Must multiple parameters be obtained simultaneously to determine correlations?
- What spatial resolution is required?
- Is imaging required or are single-point or line measurements sufficient?
- What temporal resolution is required? (e.g. time required for a single measurement)

- Do measurements need to be time resolved? (e.g. a continuous sequence of data)
- What accuracy is needed?
- What precision is needed?
- What quantity of data is required?
- When is the data needed? Is instant (real-time) data required?
- Where in the flow are measurements required? (inflow, exit, near walls, etc.)
- What type of optical access is available?
- Can (toxic) seed gases be introduced? Will they influence the properties being measured?
- What is the ordered priority of the above requirements?

This list of requirements must be matched with available measurement technologies such as those reported in the sections above. There is rarely a perfect solution for this exercise. Instead, there is a compromise between the needs of the customer and the capabilities of the instrumentation team and the chosen technique. Goals should then be established before the research actually starts. This exercise is fruitful for the measurement scientist because it often results in a need for a new measurement technique that can be developed if existing techniques are not suitable

Acknowledgements

The authors wish to thank Jennifer Inman and Joel Everhart of NASA Langley Research Center, Christopher Combs from The University of Texas at Austin and Christopher Peters from Princeton University for assistance in reviewing this manuscript. The authors acknowledge support from the NASA Fundamental Aeronautics Program, Hypersonics and High Speed Projects. Dr. Cutler received support from the National Center for Hypersonic Combined Cycle Propulsion grant FA 9550-09-1-0611. The technical monitors on the grant are Chiping Li (AFOSR), and Aaron Auslender and Rick Gaffney (NASA).

References

[1] Schuler, K.E., "Studies in Nonequilibrium Rate Processes. II. The Relaxation of Vibrational Nonequilibrium Distributions in Chemical Reactions and Shock Waves," J. Phys. Chem., 1957, 61 (7), pp 849–856, July 1957

[2] Bird, G. A. "Breakdown of translational and rotational equilibrium in gaseous expansions." AIAA Journal 8, no. 11 (1970): 1998-2003.

[3] W. G. Vincenti and C. H. Kruger Jr., "Introduction to Physical Gas Dynamics," Robert E. Krieger Publishing Company, Malabar, Florida, 1986, originally published by Wiley, New York,1965

[4] J. D. Anderson Jr., "Hypersonic and High-Temperature Gasdynamics," 2nd Ed. AIAA Education Series, Reston Virginia, 2006.

[5] A. C. Eckbreth, *Laser Diagnostics for Combustion Temperature and Species 2nd Ed*., Combustion Science & Technology Book Series, Volume 3, Taylor & Francis, New York, 1996.

[6] G. Tedeschi, H. Gouin, and M. Elena, "Motion of tracer particles in supersonic flows," *Experiments in Fluids*, Vol. 26, pp. 288-296, 1999.

[7] F.K. Lu and D.E. Marren AIAA (Ed), Advanced Hypersonic Test Facilities (2002), p. 17

[8] R.S.M. Chue, C.Y. Tsai, R.J. Bakos, J.I. Erdos, AIAA (Ed), Advanced Hypersonic Test Facilities (2002), p. 29

[9] Lackner, Maximilian, Gerhard Totschnig, Franz Winter, M. Ortsiefer, M. C. Amann, R. Shau, and J. Rosskopf. "Demonstration of methane spectroscopy using a vertical-cavity surface-emitting laser at 1.68 μm with up to 5 MHz repetition rate." Measurement Science and Technology 14, no. 1 (2003): 101.

[10] Kurtz, J. J., Aizengendler, M., Krishna, Y., Walsh, P., O'Byrne, S. "A rugged, high-sensitivity, TDLAS-based oxygen sensor for a scramjet inlet," ISABE-2013-1605, Proceedings of the 21st International Symposium on Air-Breathing Engines, Busan, Korea, Sept. 9-13, 2013

[11] S. A. Tedder, J. L. Wheeler, A. D. Cutler, and P. M. Danehy, "Width-increased dual-pump enhanced coherent anti-Stokes Raman spectroscopy," Applied Optics Vol. 49, No. 8, pp. 1305–1313, March 2010.

[12] R. G. Seasholtz, and A.E. Buggele. "Improvement in suppression of pulsed Nd: YAG laser light with iodine absorption cells for filtered Rayleigh scattering measurements." NASA Technical Memorandum 113177, November 1997.

[13] N. Chai, S. V. Naik, N. M. Laurendeau, R. P. Lucht, S. Roy, and J. R. Gord. "Single-laser-shot detection of nitric oxide in reacting flows using electronic resonance enhanced coherent anti-Stokes Raman scattering." *Applied Physics Letters* 93, no. 9 (2008): 091115-091115.

[14] M. A. Woodmansee, V. Iyer, J. C. Dutton, and R. P. Lucht. "Nonintrusive pressure and temperature measurements in an underexpanded sonic jet flowfield." AIAA journal 42, no. 6 (2004): 1170-1180.

[15] Cruden, B., *Electron Density Measurement in Reentry Shocks for Lunar Return*, Journal of Thermophysics and Heat Transfer, Vol. 26, No. 2 (2012), pp. 222-230.

[16] Winter, M. W., Raiche, G., Prabhu, D. K., "Emission Spectroscopy and Radiometry Measurements in the NASA Ames IHF Arc Jet Facility," proceedings of the 5th ESA-CNES RHTG workshop in Barcelona, Spain, 16th to 19th Oct. 2012.

[17] Cauchon, D. L., Radiative Heating Results from the FIRE II Flight Experiment at a Re-entry Velocity of 11.4 Kilometers per Second, TM X-1402, NASA, 1967.

[18] Erdman, Peter W., Edward C. Zipf, Patrick Espy, Carl L. Howlett, Deborah A. Levin, Robert J. Collins, and Graham V. Candler. "Measurements of ultraviolet radiation from a 5-km/s bow shock." Journal of Thermophysics and Heat Transfer 8, no. 3 (1994): 441-446.

[19] Kontinos, D. A., Wright, M. J., "Introduction: Atmospheric Entry of the Stardust Sample Return Capsule," Journal of Spacecraft and Rockets, Vol. 47, No. 5 (2010), pp. 705-707.

[20] Trumble, K. A., Cozmuta, I., Sepka, S., Jenniskens, P., Winter, M., "Postflight Aerothermal Analysis of the Stardust Sample Return Capsule," Journal of Spacecraft and Rockets, Vol. 47, No. 5 (2010), pp. 765-774.

[21] Winter, M. W., McDaniel, R. D., Chen, Y.-K., Liu, Y., Saunders, D., Jenniskens, P., Radiation Modeling for the Reentry of the Hayabusa Sample Return Capsule, AIAA-2012-1296, 50th AIAA Aerospace Sciences Meeting, Nashville, Tennessee, 9 - 12 Jan 2012.

[22] Herzberg, G., *Molecular Spectra and Molecular Structure: Vol. I, Spectra of Diatomic Molecules*, D. Van Nostrand Company, LTD, 1950.

[23] Gilmore, F R, Laher, R R, and Espy, P J, "Franck-Condon factors, r-centroids, electronic transition moments, and Einstein coefficients for many nitrogen and oxygen band systems," J. Phys. Chem. Ref. Data, Vol.21, p.1005, 1992.

[24] Wiese, W. L., Smith, M. W. and Miles, B. M.: *Atomic Transition Probabilities, Volume I, Hydrogen through Neon*, Institute for Basic Standards, National Bureau of Standards, Washington, D. C., October 1969.

[25] NIST-database: *physics.nist.gov/cgi-bin/At_Data/main_asd*

[26] Bashkin, S., Stoner, J.O. Jr.: *Atomic Energy Levels and Grotian Diagrams, Vol.2*, North-Holland, Amsterdam, 1982.

[27] Aaron M. Brandis, Alan Wray, Yen Liu, David W. Schwenke, Winifred M. Huo, Christopher O. Johnston, "Validation of HyperRad for Earth Entries," AIAA 2013-2777), 44th AIAA Thermophysics Conference, 2013.

[28] Dunham, J: *The energy levels of a rotating vibrator*, Phys. Rev. 41, 721, 1932.

[29] Gilmore, F R, Laher, R R, and Espy, P J, "Franck-Condon factors, r-centroids, electronic transition moments, and Einstein coefficients for many nitrogen and oxygen band systems," J. Phys. Chem. Ref. Data, Vol.21, p.1005, 1992.

[30] Winter, M.: Emissionsspektroskopische Untersuchung der Umströmung von Probenkörpern in hochenthalpen Plasmaströmungen / Emission Spectroscopic Investigation of the Flow Field around a Blunt Body in a High Enthalpy Flow, Dissertation (in German), Universität Stuttgart, Germany, Dec. 2006.

[31] Park, C.: *Nonequilibrium Hypersonic Aerothermodynamics*, John Wiley and Sons, New York, 1989.

[32] P. M. Morse, "Diatomic Molecules according to the Wave Mechanics: II. Vibrational Levels," Phys. Rev. 34, 57 (1929).

[33] Steele, D., Lippincot, E. R., and Vanderslice, J. T., "Comparative Study of Empirical Internuclear Potential Functions," Review of Modern Physics, Vol. 34, 1962, pp. 239-251.

[34] Le Roy , R. J.: *RKR1 2.0 - A Computer Program Implementing the First-Order RKR Method for Determining Diatomic Molecule Potential Energy Functions*, Guelph-Waterloo Centre for Graduate Work in Chemistry, University of Waterloo, Waterloo, Ontario N2L 3G1, Canada, April 2004.

[35] Vest, C. M. "Holographic interferometry." New York, John Wiley and Sons, Inc., 1979. 476 p. 1 (1979).

[36] Winter, M. W., Prabhu, D. K., "Excited State Chemistry in the Free Stream of the NASA IHF Arc Jet Facility Observed by Emission Spectroscopy," 42nd AIAA Thermophysics Conference in Honolulu, Hawaii, 27 - 30 Jun 2011.

[37] Modest, M: *Radiation Heat Transfer*, Academic Press, Elsevier Science, USA, 2003.

[38] Griem, H. R.: *Plasma Spectroscopy*, McGraw-Hill Book Company, New York, USA, 1964.

[39] Laux C. O.: *Radiation and Nonequilibrium Collisional-Radiative Models*, VKI Special Course on Physico-Chemical Models for High Enthalpy and Plasma Flows Modeling, Belgium, June 4-7, 2002. See also Laux, C.O., Pierrot, L., and Gessman, R.J., "State-to-state modeling of a recombining nitrogen plasma experiment," *Chemical Physics*, Vol. 398, pp. 46-55, DOI: 10.1016/j.chemphys.2011.10.028, 2012.

[40] Quintero, M.C., Rodero, A., Garcia, M.C. and Sola, A.: *Determination of the Excitation Temperature in a Nonthermodynamic-Equilibrium High-Pressure Helium Microwave Plasma Torch*, Applied Spectroscopy, Volume 51, Number 6, p. 778-784, 1997.

[41] Whiting, E E, Park, C, Liu, Y, Arnold, J O, and Paterson, J A, "NEQAIR96, Nonequilibrium and Equilibrium Radiative Transport and Spectra Program: User's Manual," NASA RP-1389, NASA, December 1996.
[42] Johnston, C. O., Hollis, B. R., and Sutton, K., "Spectrum Modeling for Air Shock-Layer Radiation at Lunar-Return Conditions," Journal of Spacecraft and Rockets, Sep.-Oct. 2008.
[43] Fujita, K., and Abe, T., "SPRADIAN, Structured Package for Radiation Analysis: Theory and Application," The Institute of Space and Astronautical Science Report No. 669, July 1997.
[44] Smith, A. J., Wood, A., Dubois, J., Fertig, M., Pfeiffer, B.: Plasma Radiation Database PARADE V22 Final Report Issue 3, ESTEC contract 11148/94/NL/FG, FGE TR28/96, Issue 3, Oktober 2006.
[45] http://www.specair-radiation.net (last accessed in Feb 2013)
[46] http://www.sri.com/contact/form/lifbase (last accessed in Feb 2013)
[47] J. Luque and D.R. Crosley, "LIFBASE: Database and spectral simulation (version 1.5)", SRI International Report MP 99-009 (1999)
[48] http://cfp.ist.utl.pt/radiation/SPARTAN/SPARTAN.html (last accessed in April 2013)
[49] Babou, Y., Riviere, P., Perrin, M., and Soufiani, A., "Spectroscopic data for the prediction of radiative transfer in CO2-N2 plasmas". Journal of Quantitative Spectroscopy & Radiative Transfer, 110, pp. 89–108, 2009.
[50] Perrin M.-Y., Rivière P., Soufiani A., Radiation Database for Earth and Mars Entry, RTO-EN-AVT-162 Nonequilibrium Gas Dynamics - From Physical Models to Hypersonic Flights (2009) 8.1,8.40.
[51] Cruden, B., Martinez, R., Grinstead, J. H., Olejniczak, J., "Simultaneous Vacuum Ultraviolet through Near IR Absolute Radiation Measurement with Spatiotemporal Resolution in an Electric Arc Shock Tube," AIAA 2009-4240, 41st AIAA Thermophysics Conference, 22 - 25 June 2009, San Antonio, Texas.
[52] Aaron Brandis, Christopher Johnston, Marco Panesi, Brett Cruden, Dinesh Prabhu, Deepak Bose, "Investigation of Nonequilibrium Radiation for Mars Entry," AIAA 2013-1055, 51st AIAA Aerospace Sciences Meeting including the New Horizons Forum and Aerospace Exposition, 2013.
[53] Golde, M. F., and Thrush, B. A., "Afterglows," Rep. Prog. Phys. 1973, volume 36, pp 1285-1364, 1973.
[54] Harry Partridge, Stephen R. Langhoff, and Charles W. Bauschlicher, Jr., and David W. Schwenke, "Theoretical study of the $A^5\Sigma_g^+$ and C''$^5\Pi_u$ states of N_2: Implications for the N_2 afterglow," J. Chern. Phys. 88 (5), 1 March 1988. Figure 3.11b reproduced with permission from the authors. Copyright 1988, AIP Publishing LLC. DOI: 10.1063/1.453962
[55] Camac, M., "O_2 vibration relaxation in oxygen-argon mixtures," *Journal of Chemical Physics*, Vol. 34, No. 2, pp. 448-, 1961.
[56] Vincenti, W.G., and Kruger, C.H., *Introduction to Physical Gas Dynamics*, Wiley, New York, 1967.
[57] Gauglitz, G., and Vo-Dinh, T., *Handbook of Spectroscopy*, Wiley-VCH Verlag GmbH & Co. KGaA, Weinheim, 2003.
[58] Thorne, A.P., *Spectrophysics*, 2nd Edition, Chapman and Hall, 1988.
[59] Palma, P.C, "Laser-Induced Fluorescence Imaging in Free-Piston Shock Tunnels" PhD Thesis, Australian National University, 1999.
[60] Webster, C.R., Menzies, R.T. and Hinkley, E.D., "Infrared Laser Absorption: Theory and Applications" *in Laser Remote Chemical Analysis, Chemical Analysis Vol. 94.* Ed. Measures, R.M., John Wiley and Sons, 1988.
[61] Demtroder, Wolfgang. "Atoms, molecules and photons." Heidelberg, Springer-Verlag Berlin Heidelberg, 2006. 571 (2006).
[62] Di Rosa, M. D., "Collision-broadening and –shift of NO γ(0,0) absorption lines by H2O, O2, and NO at 295 K", *Journal of Molecular Spectroscopy*, Vol. 164, pp. 97-117, 1994
[63] Rothman, L.S., Gordon, I.E., Barbe, A., Benner D.C., Bernath, P.F., Birk, M., et al., "The HITRAN 2008 molecular spectroscopic database," *Journal of Quantitative Spectroscopy and Radiative Transfer*, Vol. 110, pp. 533-572, 2009.

[64] Humlicek, J., "Optimized computation of the Voigt and complex probability functions," *Journal of Quantitative Spectroscopic Radiative Transfer*, Vol. 27, No. 4, pp. 437-444, 1982.

[65] Arnold, J. O.; Whiting, E. E.; Lyle, G. C., Line by line calculation of spectra from diatomic molecules and atoms assuming a Voigt line profile, Journal of Quantitative Spectroscopy and Radiative Transfer, vol. 9, issue 6, pp. 775-798, Pergamon Press 1969.

[66] Baer, D.S., and Hanson, R.K., "Tunable diode laser absorption diagnostics for atmospheric pressure plasmas," *Journal of Quantitative Spectroscopic Radiative Transfer*, Vol. 47, No. 6, pp. 455-475, 1992.

[67] Haverlag, M., Stoffels, E., Stoffels, W.W., Kroesen, G.M.W. and De Hoog, F.J. "Measurement of the gas temperature in fluorocarbon radio frequency discharges using infrared absorption spectroscopy." *Journal of Vacuum Science & Technology A: Vacuum, Surfaces and Films* Vol. 14, No. 2 (1996): 380-383.

[68] Haverlag, M., Stoffels, E., Stoffels, W.W., Kroesen, G.M.W. and De Hoog, F.J. "Measurement of the gas temperature in fluorocarbon radio frequency discharges using infrared absorption spectroscopy." *Journal of Vacuum Science & Technology A: Vacuum, Surfaces and Films* Vol. 14, No. 2 (1996): 380-383.

[69] Zhang, F.-Y., Komurasaki, K., Iida, T. and Fujiwara, T. "Diagnostics of an argon arcjet plume with a diode laser," *Applied Optics*, Vol. 38, No. 9, pp. 1814-1822, 1999.

[70] Parker, R.A., Wakeman, T., MacLean, M., and Holden, M., "Measuring nitric oxide freestream concentration using quantum cascade lasers at CUBRC," AIAA Paper 2006-926, *44th AIAA Aerospace Sciences Meeting and Exhibit*, Jan 2006.

[71] Sanders, S.T., Wang, J., Jeffries, J. B., and Hanson, R. K., "Diode-laser absorption sensor for line-of-sight gas temperature distributions," *Applied Optics*, Vol. 40, pp. 4404-4415, 2001.

[72] Silver, J.A., and Kane, D.J., "Diode laser measurements of concentration and temperature in microgravity combustion," *Measurement Science and Technology*, Vol. 10, pp. 845-852, 1999.

[73] Rothman, L.S., Rinsland, C. P., Goldman, A. et al., "The HITRAN molecular spectroscopic database and HAWKS (HITRAN atmospheric workstation): 1996 Edition," *Journal of Quantitative Spectroscopy and Radiative Transfer*, Vol. 60, pp. 665-710, 1998.

[74] Allen, M. G., "Diode laser absorption sensors for gas dynamic and combustion flows, " *Measurement Science and Technology*, Vol. 9, No. 4, pp. 545-562, 1998.

[75] Wehe, S.D., Baer, D.S., and Hanson, R.K., "Tunable diode-laser absorption measurements of temperature, velocity, and H_2O in hypervelocity flows," AIAA Paper 97-3267, *33rd Joint Propulsion Conference and Exhibit*, Seattle, WA, 1997.

[76] Liu, J. T. C., Jeffries, J. B., and Hanson, R. K., "Wavelength modulation absorption spectroscopy with 2 f detection using multiplexed diode lasers for rapid temperature measurements in gaseous flows," *Applied Physics B*, Vol. 78, pp. 503-511, 2004.

[77] Wilson, G.V.H., "Modulation broadening of NMR and ESR line shapes", *Journal of Applied Physics*, Vol. 34, pp.3276-3285, 1963.

[78] Reid, J., and Labrie, D., "Second harmonic detection with tunable diode lasers – comparison of experiment and theory" *Applied Physics B*, Vol. 26, pp. 203-210, 1981.

[79] Silver, J., A., "Frequency-modulation spectroscopy for trace species detection: theory and comparison among experimental methods", *Applied Optics*, Vol. 31, pp. 707-717, 1992.

[80] Cooper, D.E., and Warren, R. E., "Two-tone optical heterodyne spectroscopy with diode lasers: theory of line shapes and experimental results", *Journal of Optical Society America B*, Vol. 4, pp. 470-480, 1987.

[81] Goldstein, C.S., Schultz, I.A., Jeffries, J.B., and Hanson, R.K., "Tunable diode laser absorption sensor for measurements of temperature and water concentration in supersonic flows," AIAA Paper 2011-1094, *49th AIAA Aerospace Sciences Meeting including the New Horizons Forum and Aerospace Exposition*, Orlando FL, Jan 4-7, 2011.

[82] Haller, K. L. and Hobbs, P.C.D. "Double-beam laser absorption spectroscopy: shot noise-limited performance at baseband with a novel electronic noise canceler." In *Optics, Electro-Optics, and Laser Applications in Science and Engineering*, pp. 298-309. International Society for Optics and Photonics, 1991.

[83] Allen, M.G., and Kessler, W.J. "Simultaneous water vapor concentration and temperature measurements using 1.31-micron diode lasers." *AIAA Journal* Vol. 34, No. 3, pp. 483-488, 1996.

[84] Upschulte, B. L., Miller, M.F. and Allen, M.G. "Diode laser sensor for gasdynamic measurements in a model scramjet combustor." *AIAA Journal* Vol. 38, No. 7, pp.1246-1252, 2000.

[85] Griffiths, A.D., and Houwing, A.F.P. "Diode laser absorption spectroscopy of water vapor in a scramjet combustor." *Applied Optics* Vol. 44, No. 31 pp. 6653-6659, 2005.

[86] Pan, F. and Oka, T, "Radial distribution of molecular ions in the positive column of de glow discharges using infrared diode-laser spectroscopy," *Physical Review A*, Vol. 36, pp. 2297-2310, 1987.

[87] Brandt, O. And Roth, P., "Temperature measurements behind shock waves using a rapid scanning IR-diode laser," *Physics of Fluids*, Vol. 30, No. 5, pp. 1294-1298, 1987.

[88] Lin, X., Yu, X.L., Li, F., Zhang, S.H., Xin, J.G., and Chang, X.Y., "CO concentration and temperature measurements in a shock tube for Martian mixtures by coupling OES and TDLAS," *Applied Physics B.* 2012

[89] Farooq, A., Jeffries, J.B., and Hanson, R.K., "CO_2 concentration and temperature sensor for combustion gases using diode-laser absorption near 2.7 μm," *Applied Physics B*, Vol. 90, pp. 619-628, 2008.

[90] Lyle, K. H., Jeffries, J.B. and Hanson, R. K. "Diode-laser sensor for air-mass flux 1: design and wind tunnel validation." *AIAA Journal* Vol. 45, No. 9 pp. 2204-2212, 2007.

[91] Mohamed, A.K., Henry, D., Falni, J. P., Sagnier, P., Soutad, J., Beck, W.H., and Martinez Schramm, J., "Infrared diode laser absorption spectroscopy measurements in the S4MA, F4, and HEG Hypersonic Flows, " *International Symposium on Atmospheric Reentry Vehicles and Systems*, ONERA Paper No. TP 1999-45, March 1999.

[92] Philippe, L. C., and Hanson, R.K. "Laser diode wavelength-modulation spectroscopy for simultaneous measurement of temperature, pressure, and velocity in shock-heated oxygen flows." *Applied Optics* Vol. 32, No. 30 pp. 6090-6103, 1993.

[93] Wittig, S. and O'Byrne, S. "Characterization of supersonic combustor inlet flows using diode laser absorption spectroscopy." *AIAA Paper* 2011-0073, 49th AIAA Aerospace Sciences Meeting , Orlando, Florida, January 4-7, 2011.

[94] Hanson, R.K., "Application of quantitative laser sensors to kinetics, propulsion and practical energy systems," *Proceedings of the Combustion Institute*, Vol. 33, pp. 1-40, 2011.

[95] K. M. Busa, E. N. Ellison, B. J. McGovern, and J. C. McDaniel G. S. Diskin, M. J. DePiro, D. P. Capriotti, and R. L. Gaffney, "Measurements on NASA Langley Durable Combustor Rig by TDLAT: Preliminary Results," 51st AIAA Aerospace Sciences Meeting including the New Horizons Forum and Aerospace Exposition, Paper AIAA 2013-0696, Grapevine TX., 7-10 January 2013.

[96] M. S. Brown, G. C. Herring, K. Cabell, N. Hass, T. F. Barhorst, and M. Gruber, "Optical Measurements at the Combustor Exit of the HIFiRE 2 Ground Test Engine," Paper AIAA 2012-0857, 50th AIAA Aerospace Sciences Meeting including the New Horizons Forum and Aerospace Exposition, Nashville, TN., 9-12 January 2012.

[97] L. Ma, X. Li, S. T. Sanders, A. W. Caswell, S. Roy, D. H. Plemmons, and J. R. Gord, "50-kHz-rate 2D imaging of temperature and H_2O concentration at the exhaust plane of a J85 engine using hyperspectral tomography," Optics Express, Vol. 21, Issue 1, pp. 1152-1162, 2013.

[98] Berden, G., and Engeln, R., *Cavity Ring-Down Spectroscopy: Techniques and Applications*, Wiley, 2009.

[99] Scherer, J.J., Paul, J.B., O'Keefe, A., and Saykally, R.J., "Cavity ringdown laser absorption spectroscopy: history, development, and application to pulsed molecular beams," *Chemical Review*, Vol. 97, pp. 25-51, 1997.

[100] Romanini, D., Dupré, P., and Jost, R., "Non-linear effects by continuous wave cavity ringdown spectroscopy in jet-cooled NO_2" *Vibrational Spectroscopy*, Vol. 19, pp. 93-106, 1999.

[101] Engeln, R., Berden, G., Peeters, R. and Meijer, G. "Cavity enhanced absorption and cavity enhanced magnetic rotation spectroscopy." *Review of Scientific Instruments* Vol. 69, No. 11, pp. 3763-3769, 1998.

[102] O'Keefe, A. "Integrated cavity output analysis of ultra-weak absorption." *Chemical Physics Letters* Vol. 293, No. 5 pp. 331-336, 1998.

[103] Paul, J.B., Lapson, L. and Anderson, J.G. "Ultrasensitive absorption spectroscopy with a high-finesse optical cavity and off-axis alignment." *Applied Optics* Vol. 40, No. 27, pp. 4904-4910, 2001.

[104] Bakowski, B., Hancock, G. Peverall, R., Ritchie, G.A.D. and Thornton, L.J. "Characterization of an inductively coupled N_2 plasma using sensitive diode laser spectroscopy." *Journal of Physics D: Applied Physics*, Vol. 37, No. 15, pp. 2064-2072, 2004.

[105] Fiedler, S. E., Hese, A. and Ruth, A.A. "Incoherent broad-band cavity-enhanced absorption spectroscopy." *Chemical Physics Letters* Vol. 371, No. 3, pp. 284-294, 2003.

[106] Bonnet, J.P., Gresillon, D., and Taran, J.P. "Nonintrusive measurements for high-speed, supersonic, and hypersonic flows," *Annual Review of Fluid Mechanics*, Vol. 30, pp. 231-273, 1998.

[107] Ouyang, X., Varghese, P. L., "Line-of-sight absorption measurements of high temperature gases with thermal and concentration boundary layers," *Applied Optics*, Vol. 28., pp. 3979-3984, 1989.

[108] Schoenung, M., and Hanson, R. K., "CO and temperature measurements in a flat flame by laser absorption spectroscopy and probe techniques," *Combustion Science and Technology*, Vol. 24, pp. 227-237, 1980.

[109] K. Kohse-Höinghaus, and J. B. Jeffries, eds., *Applied Combustion Diagnostics*, Combustion: An International Series, Taylor & Francis, New York, 2002.

[110] P. C. Palma, *Laser-Induced Fluorescence Imaging in Free-Piston Shock Tunnels*, PhD Thesis, Australian National University, submitted May 1998, revised February 1999.

[111] B. A. E. Saleh, and M. C. Teich, *Fundamentals of Photonics 2nd Ed.*, John Wiley & Sons, Inc., Hoboken, New Jersey, 2007.

[112] W. K. Bischel, P. J. Kelly, and C. K. Rhodes, "*High-resolution Doppler-free two-photon spectroscopic studies of molecules. I. The ν_3 bands of $^{12}CH_3F$*," Physical Review A, 13(5), p. 1829, 1976.

[113] T. J. McIlrath, R. Hudson, A. Aikin, and T. D. Wilkerson, "*Two-photon lidar technique for remote sensing of atomic oxygen*," Applied Optics, 18(3), 1979.

[114] W. K. Bischel, B. E. Perry, and D. R. Crosley, "*Detection of fluorescence from O and N atoms induced by two-photon absorption*," Applied Optics, 21(8), p. 1419-1429, 1982.

[115] U. Meier, J. Bittner, K. Kohse-Höinghaus, and Th. Just, "*Discussion of two-photon laser-excited fluorescence as a method for quantitative detection of oxygen atoms in flames*," 22nd Symposium (International) on Combustion, The Combustion Institute, vol. 22, no. 1, pp. 1887-1896. Elsevier, 1989.

[116] D. R. Crosley, "*Rotational and Translational Effects in Collisions of Electronically Excited Diatomic Hydrides*," Journal of Physical Chemistry, 1989, 93, 6273 – 6282.

[117] J. D. Anderson Jr., *Hypersonic and High-Temperature Gas Dynamics 2nd ed.*, AIAA Education Series, AIAA, Reston, VA, 2006.

[118] W. G. Vincenti, and C. H. Kruger Jr., *Introduction to Physical Gas Dynamics*, Reprint of 1967 ed., Wiley, New York, 1975.

[119] P. H. Paul, J. A. Gray, J. L. Durant, J. W. Thoman, "*Collisional Quenching Corrections for Laser-Induced Fluorescence Measurements of NO $A^2\Sigma^+$*," AIAA Journal, 32(8), August 1994.

[120] D. S. Baer, H. A. Chang, and R. K. Hanson, "*Fluorescence diagnostics for atmospheric-pressure plasmas using semiconductor lasers*," Journal of the Optical Society of America B, 9(11), pp. 1968-1978, November, 1992.

[121] J. G. Liebeskind, R. K. Hanson, and M. A. Cappelli, "*Laser-induced fluorescence diagnostic for temperature and velocity measurements in a hydrogen arcjet plume*," Applied Optics, 32(30), pp. 6117-6127, October 20, 1993.

[122] J. A. Inman, B. F. Bathel, C. T. Johansen, P. M. Danehy, S. B. Jones, J. G. Gragg, and S. C. Splinter, "*Nitric Oxide PLIF Measurements in the Hypersonic Materials Environmental Test System (HYMETS)*," 49th AIAA Aerospace Sciences Meeting, AIAA Paper 2011-1090, Orlando, FL, January 4-7, 2011.

[123] P. V. Storm, and M. A. Cappelli, "*LIF Characterization of Arcjet Nozzle Flows*," AIAA, ASME, SAE, and ASEE, Joint Propulsion Conference, AIAA Paper 1996-2987, Lake Buena Vista, FL, July 1 – 3, 1996.

[124] D. G. Fletcher, "*Arcjet flow properties determined from laser-induced fluorescence of atomic nitrogen*," 36th AIAA Aerospace Sciences Meeting, AIAA Paper 1998-0205.

[125] D. G. Fletcher, "*Arcjet flow properties determined from laser-induced fluorescence of atomic nitrogen*," Applied Optics, 38(9), March 20, 1999.

[126] J. H. Grinstead, B. J. Porter, and J. E. Carballo, "*Flow Property Measurement Using Laser-Induced Fluorescence in the NASA Ames Interaction Heating Facility*," 49th AIAA Aerospace Sciences Meeting, AIAA Paper 2011-1091, Orlando, FL., January 4 – 7, 2011.

[127] A. Lutz, J. Meyers, W. Owens, S. Smith, and D. G. Fletcher, "*Experimental Analysis of Carbon Nitridation and Oxidation Efficiency with Laser-Induced Fluorescence*," 51st AIAA Aerospace Sciences Meeting, AIAA Paper 2013-0924, Grapevine, TX., January 7 – 10, 2013.

[128] R. L. McKenzie, and K. P. Gross, "*Two-photon excitation of nitric oxide fluorescence as a temperature indicator in unsteady gasdynamic processes*," Applied Optics, 20(12), June 15, 1981.

[129] B. K. McMillin, J. L. Palmer, and R. K. Hanson, "*Temporally resolved, two-line fluorescence imaging of NO temperature in a transverse jet in a supersonic cross flow*," Applied Optics, 32(36), December, 20, 1993.

[130] J. M. Seitzman, R. K. Hanson, P. A. DeBarber, and C. F. Hess, "*Application of quantitative two-line OH planar laser-induced fluorescence for temporally resolved planar thermometry in reacting flows*," Applied Optics, 33(18), June 20, 1994.

[131] B. K. McMillin, J. M. Seitzman, and R. K. Hanson, "*Comparison of NO and OH Planar Fluorescence Temperature Measurements in Scramjet Model Flowfields*," AIAA Journal, 32(10), October 1994.

[132] P. C. Palma, P. M. Danehy, and A. F. P. Houwing, "*Fluorescence Imaging of Rotational and Vibrational Temperature in Shock-Tunnel Nozzle Flow*," AIAA Journal, 41(9), September 2003.

[133] E. R. Lachney, and N. T. Clemens, "*PLIF imaging of mean temperature and pressure in a supersonic bluff wake*," Experiments in Fluids, 24, pp. 354-363, 1998.

[134] U. Koch, A. Gülhan, and B. Esser, "*Determination of NO-rotational and vibrational temperature profiles in a high enthalpy flow field with nonequilibrium*," 1st Joint French-German Symposium on Simulation of Atmospheric Entries by Means of Ground Test Facilities, Stuttgart, Germany, 1999.

[135] A. Del Vecchio, G. Palumbo, U. Koch, and A. Gülhan, "*Temperature Measurements by Laser-induced Fluorescence Spectroscopy in Nonequilibrium High-Enthalpy Flow*," Journal of Spacecraft and Rockets, 14(2), April-June 2000.

[136] S. Löhle, M. Auweter-Kurtz, G. Herdrich, and T. Laux, "*LIF Measurements of NO in N_2/O_2 and N_2/CO_2 Plasma Flows*," 36th AIAA Thermophysics Conference, AIAA Paper 2003-3487, Orlando, FL., June 23-26, 2003.

[137] E. A. Brinkman, G. A. Raiche, M. S. Brown, and J. B. Jeffries, "*Optical diagnostics for temperature measurement in a DC arcjet reactor used for diamond deposition*," Applied Physics B, 64(6), pp. 689-697, 1997.

[138] W. G. Bessler, and C. Schulz, "*Quantitative multi-line NO-LIF temperature imaging*," Applied Physics B, 78, pp. 519-533, 2004.

[139] J. L. Palmer, and R. K. Hanson, "*Planar laser-induced fluorescence temperature measurements in free jet flows with vibrational nonequilibrium*," 31st AIAA Aerospace Sciences Meeting, AIAA Paper 1993-0046, Reno, NV., January 11-14, 1993.

[140] J.A. Inman, B.F. Bathel, C.T. Johansen, P.M. Danehy, S.B. Jones, J.G. Gragg, and S.C. Splinter, "*Nitric-Oxide Planar Laser-Induced Fluorescence Measurements in the Hypersonic Materials Environmental Test System*," Accepted by AIAA Journal, AIAA Journal 51, no. 10, pp. 2365-2379, 2013.

[141] A.J. Smits and T.T. Lin, eds., *Flow Visualization: Techniques and Examples 2nd Ed.*, Imperial College Press, London, 2012.

[142] H. Katô, and M. Baba, "*Dynamics of Excited Molecules: Predissociation*," Chemical Review, 95, pp. 2311-2349, 1995.

[143] G. Herzberg, "*Molecular Spectra and Molecular Structure: I. Spectra of Diatomic Molecules"*, New York, Van Nostrand Reinhold, 1950.

[144] G. Laufer, T. M. Quagliaroli, R. H. Krauss, R. B. Whitehurst III, J. C. McDaniel, and J. H. Grinstead, "*Planar OH Density and Apparent Temperature Measurements in a Supersonic Combusting Flow*," AIAA Journal, 34(3), March 1996.

[145] J. Zhang, G. B. King, N. M. Laurendeau, and M. W. Renfro, "*Two-point time-series measurements of hydroxyl concentration in a turbulent nonpremixed flame*," Applied Optics, 46(23), August 10, 2007.

[146] T. B. Settersten, B. D. Patterson, and W. H. Humphries, "*Radiative lifetimes of NO $A^2\Sigma^+(v'=0,1,2)$ and the electronic transition moment of the $A^2\Sigma^+$-$X^2\Pi$ system*," Journal of Chemical Physics, 131, 2009.

[147] T. B. Settersten, B. D. Patterson, and J. A. Gray, "*Temperature- and species-dependent quenching of NO $A^2\Sigma^+(v'=0)$ probed by two-photon laser-induced fluorescence using a picosecond laser*," Journal of Chemical Physics, 124, 2006.

[148] T. B. Settersten, B. D. Patterson, and C. D. Carter, "*Collisional quenching of NO $A^2\Sigma^+(v'=0)$ between 125 and 294 K*," Journal of Chemical Physics, 130, 2009.

[149] J. H. Grinstead, D. M. Driver, and G. A. Raiche, "*Radial profiles of arcjet flow properties measured with laser-induced fluorescence of atomic nitrogen*," 41st AIAA Aerospace Sciences Meeting, AIAA 2003-400, Reno, NV., January 6-9, 2003.

[150] D. G. Fletcher, and M. Playez, "*Characterization of supersonic and subsonic plasma flows*," 25th AIAA Aerodynamic Measurement Technology and Ground Testing Conference, AIAA 2006-3294, San Francisco, CA., June 5-8, 2006.

[151] B. J. Lochman, Z. R. Murphree, V. Narayanaswamy, and N. T. Clemens, "*PLIF imaging of naphthalene-ablation products in a Mach 5 turbulent boundary layer*," 27th AIAA Aerodynamic Measurement Technology and Ground Testing Conference, AIAA 2010-4346, Chicago, IL., June 28 – July 1, 2010.

[152] O. R. H. Buxton, B. J. Lochman, M. Sharma, and N. T. Clemens, "*Simultaneous PIV and PLIF Imaging of Low-Temperature Ablation in a Mach 5 Turbulent Boundary Layer*," 50th AIAA Aerospace Sciences Meeting, AIAA 2012-440, Nashville, TN., January 9-12, 2012.

[153] M. Versluis, N. Georgiev, L. Martinsson, M. Aldén, and S. Kröll, "*2-D absolute OH concentration profiles in atmospheric flames using planar LIF in a bi-directional laser beam configuration*," Applied Physics B, 65, pp. 411-417, 1997.

[154] C. D. Carter, and R. S. Barlow, "*Simultaneous measurements of NO, OH, and the major species in turbulent flames*," Optics Letters, 19(4), pp. 299-301, February 15, 1994.

[155] R. S. Barlow, G.-H. Wang, P. Anselmo-Filho, M. S. Sweeney, and S. Hochgreb, "*Application of Raman/Rayleigh/LIF diagnostics in turbulent stratified flames*," Proceedings of the Combustion Institute, 32, pp. 945-953, 2009.

[156] J. C. McDaniel, "*Nonintrusive Pressure Measurement with Laser-Induced Iodine Fluorescence*," 18th AIAA Thermophysics Conference, AIAA 1983-1468, Montreal, Canada, June 1-3, 1983.

[157] F. Lemoine and B. Leporcq, "*An efficient optical pressure measurement in compressible flows: Laser-induced iodine fluorescence*," Experiments in Fluids, 19, pp. 150-158, 1995.

[158] A. Y. Chang, B. E. Battles, and R. K. Hanson, "*Simultaneous measurements of velocity, temperature, and pressure using rapid cw wavelength-modulation laser-induced fluorescence of OH*," Optics Letters, 15(12), June 15, 1990.

[159] S. V. Naik, W. D. Kulatilaka, K. K. Venkatesan, and R. P. Lucht, "*Pressure, Temperature, and Velocity Measurements in Underexpanded Jets Using Laser-Induced Fluorescence Imaging*," AIAA Journal, 47(4), April 2009.

[160] B. Hiller, and R. K. Hanson, "*Simultaneous planar measurements of velocity and pressure fields in gas flows using laser-induced fluorescence*," Applied Optics, 27(1), January 1, 1988.

[161] J. Hartfield Jr., S. D. Hollo, and J. C. McDaniel, "*A unified planar measurement technique for compressible flows using laser-induced iodine fluorescence*," 30th AIAA Aerospace Sciences Meeting, AIAA 1992-0141, Reno, NV, January 6-9, 1992.

[162] D. A. Rothamer and R. K. Hanson, "*Temperature and pressure imaging using infrared planar laser-induced fluorescence*," Applied Optics, 49(33), pp. 6436-6447, November 20, 2010.

[163] W. J. Marinelli, W. J. Kessler, M. G. Allen, S. J. Davis, S. Arepalli, and C. D. Scott, "*Copper atom based measurements of velocity and turbulence in arc jet flows*," 29th Aerospace Sciences Meeting, AIAA 1991-358, Reno, NV., January 7-10, 1991.

[164] J. C. McDaniel, B. Hiller, and R. K. Hanson, "*Simultaneous multiple-point velocity measurements using laser-induced iodine fluorescence*," Optics Letters, 8(1), pp. 51-53, January 1983.

[165] K. G. Klavuhn, G. Gauba, and J. C. McDaniel, "*OH Laser-Induced Fluorescence Velocimetry Technique for Steady, High-Speed, Reacting Flows*," Journal of Propulsion and Power, 10(6), pp. 787-797, 1994.

[166] W. D. Kulatilaka, S. V. Naik, and R. P. Lucht, "*Development of High-Spectral-Resolution Planar Laser-Induced Fluorescence Imaging Diagnostics for High-Speed Gas Flows*," AIAA Journal, 46(1), January 2008.

[167] P. M. Danehy, P. Mere, M. J. Gaston, S. O'Bryne, P. C. Palma, A. F. P. and Houwing, "*Fluorescence velocimetry of the hypersonic, separated flow over a cone,*" AIAA Journal, 39(7), pp. 1320-1328, 2001.

[168] R. Hruschka, S. O'Byrne, and H. Kleine, "*Two-component Doppler-shift fluorescence velocimetry applied to a generic planetary entry probe model*," Experiments in Fluids, 48, pp. 1109-1120, 2010.

[169] D. G. Fletcher, and J. C. McDaniel, "*Laser-Induced Iodine Fluorescence Technique for Quantitative Measurement in a Nonreacting Supersonic Combustor*," AIAA Journal, 27(5), May 1989.

[170] R. J. Hartfield, S. D. Hollo, and J. C. McDaniel, "*Planar Measurement Technique for Compressible Flows Using Laser-Induced Iodine Fluorescence*," AIAA Journal, 31(3), March 1993.

[171] J. M. Donohue, and J. C. McDaniel, "*Computer-Controlled Multiparameter Flowfield Measurements Using Planar Laser-Induced Iodine Fluorescence*," AIAA Journal, 34(8), August 1996.

[172] M. Zimmerman, and R. B. Miles, "*Hypersonic-helium-flow-field measurements with the resonant Doppler velocimeter*," Applied Physics Letters, 37(10), November 15, 1980.

[173] B. F. Bathel, C. Johansen, J. A. Inman, S. B. Jones, and P. M. Danehy, "*Review of Fluorescence-Based Velocimetry Techniques to Study High-Speed Compressible Flows*,"AIAA 2013-0339, 51st AIAA Aerospace Sciences Meeting, Grapevine, TX, January 7-10, 2013.

[174] B. Hiller, and R. K. Hanson, "*Two-frequency laser-induced fluorescence technique for rapid velocity-field measurements in gas flows*," Optics Letters, 10(5), May, 1985.

[175] U. Westblom, and M. Aldén, "*Spatially resolved flow velocity measurements using laser-induced fluorescence from a pulsed laser*," Optics Letters, 14(1), January 1, 1989.

[176] P. H. Paul, M. P. Lee, and R. K. Hanson, "*Molecular velocity imaging of supersonic flows using pulsed planar laser-induced fluorescence of NO*," Optics Letters, 14(9), May 1, 1989.

[177] M. Allen, S. Davis, W. Kessler, H. Legner, K. McManus, P. Mulhall, T. Parker, and D. Sonnenfroh, "*Velocity Field Imaging in Supersonic Reacting Flows near Atmospheric Pressure*," AIAA Journal, 32(8), August 1994.

[178] M. M. Koochesfahani, and D. G. Nocera, *"Molecular Tagging Velocimetry*," *Handbook of Experimental Fluid Dynamics*, Chap. 5.4, edited by J. Foss, C. Tropea, and A. Yarin, Springer-Verlag, Berlin, 2007.

[179] B. Hiller, R. A. Booman, C. Hassa, and R. K. Hanson, "*Velocity Visualization in Gas Flows Using Laser-Induced Phosphorescence of Biacetyle*," Review of Scientific Instruments, 55(12), pp. 1964-1967, December, 1984.

[180] P. M. Danehy, S. O'Byrne, A. F. P. Houwing, J. S. Fox, and D. R. Smith, "*Flow-Tagging Velocimetry for Hypersonic Flows Using Fluorescence of Nitric Oxide*," AIAA Journal, 41(2), February 2003.

[181] B. F. Bathel, P. M. Danehy, J. A. Inman, S. B. Jones, C. B. Ivey, C. P, and Goyne, "*Velocity Profile Measurements in Hypersonic Flows Using Sequentially Imaged Fluorescence-Based Molecular Tagging*," AIAA Journal, 49(9), September 2011.

[182] W. R. Lempert, N. Jiang, S. Sethuram, and M. Samimy, "*Molecular Tagging Velocimetry Measurements in Supersonic Microjets*," AIAA Journal, 40(6), June, 2002.

[183] W. R. Lempert, M. Boehm, N. Jiang, S. Gimelshein, and D. Levin, "*Comparison of molecular tagging velocimetry data and direct simulation Monte Carlo simulations in supersonic micro jet flows*," Experiments in Fluids, 34, pp. 403-411, 2003.

[184] A. G. Hsu, R. Srinivasan, R. D. W. Bowersox, and S. W. North, "*Two-component molecular tagging velocimetry utilizing NO fluorescence lifetime and NO_2 photodissociation techniques in an underexpanded jet flowfield*," Applied Optics, 48(22), August 1, 2009.

[185] J. A. Inman, P. M. Danehy, B. F. Bathel, D. W. Alderfer, and R. J. Nowak, "*Laser-Induced Fluorescence Velocity Measurements in Supersonic Underexpanded Impinging Jets*," 48th AIAA Aerospace Sciences Meeting, AIAA 2010-1438, Orlando, FL., January 4-7, 2010.

[186] C. T. Johansen, P. M. Danehy, S. W. Ashcraft, B. F. Bathel, J. A. Inman, and S. B. Jones, "*PLIF study of Mars Science Laboratory capsule reaction control system jets*," 41st AIAA Fluid Dynamics Conference, AIAA Paper 2011-3890, Honolulu, HI., June 27-30, 2011.

[187] C. T. Johansen, J. Novak, B. Bathel, S. W. Ashcraft, and P. M. Danehy, "*Comparison of MSL RCS jet computations with flow visualization and velocimetry*," 50th AIAA Aerospace Sciences Meeting, AIAA Paper 2012-0594, Nashville, TN., January 4-7, 2012.

[188] R. J. Balla, "Iodine Tagging Velocimetry in a Mach 10 Wake", AIAA Journal, Technical Note, (accepted).

[189] A. F. P. Houwing, D. R. Smith, J. S. Fox, P. M. Danehy, and N. R. Mudford, "*Laminar boundary layer separation at a fin-body junction in a hypersonic flow*," Shock Waves, 11, pp. 31-42, 2001.

[190] B. F. Bathel, P. M. Danehy, J. A. Inman, A. N. Watkins, S. B. Jones, W. E. Lipford, K. Z. Goodman, C. B. Ivey, and C. P. Goyne, "*Hypersonic Laminar Boundary Layer Velocimetry with Discrete Roughness on a Flat Plate*," AIAA Paper 2010-4998, 40th Fluid Dynamics Conference and Exhibit, Chicago, IL, June 28 - July 1, 2010.

[191] J. B. Michael, M. R. Edwards, A. Dogariu, and R. B. Miles, "*Femtosecond laser electronic excitation tagging for quantitative velocity imaging in air*," Applied Optics, 50(26), pp. 5158-5162, September 10, 2011.

[192] J. B. Michael, M. R. Edwards, A. Dogariu, and R. B. Miles, "*Velocimetry by femtosecond laser electronic excitation tagging (FLEET) of air and nitrogen*," 50th AIAA Aerospace Sciences Meeting, AIAA 2012-1053, Nashville, TN., January 9-12, 2012.

[193] M. R. Edwards, A. Dogariu, and R. B. Miles, "*Simultaneous Temperature and Velocity Measurement in Unseeded Air Flows with FLEET*," 51st AIAA Aerospace Sciences Meeting, AIAA 2013-0043, Grapevine, TX., January 7-10, 2013.

[194] P. Barker, A. Bishop, and H. Rubinsztein-Dunlop, "*Supersonic velocimetry in a shock tube using laser enhanced ionization and planar laser induced fluorescence*," Appl. Phys. B, 64 (3), pp. 369-376, 1997.

[195] P. F. Barker, A. M. Thomas, T. J. McIntyre, and H. Dunlop-Rubinsztein, "*Velocimetry and Thermometry of Supersonic Flow Around a Cylindrical Body*," AIAA Journal, 36 (6), pp. 1055-1060, June 1998.

[196] B. N. Littleton, A. I. Bishop, T. J. McIntyre, P. F. Barker, and H. Dunlop-Rubinsztein, "*Flow tagging velocimetry in a superorbital expansion tube*," Shock Waves, 10, pp. 225-228, 2000.

[197] R. Miles, C. Cohen, J. Connors, P. Howard, S. Huang, E. Markovitz, and G. Russell, "*Velocity measurements by vibrational tagging and fluorescent probing of oxygen*," Optics Letters, 12 (11), pp. 861-863, November, 1987.

[198] R. B. Miles, D. Zhou, B. Zhang, W. R. Lempert, and Z-S. She, "*Fundamental Turbulence Measurements by Relief Flow Tagging*," AIAA Journal, 31(3), March, 1993.

[199] R. B. Miles, J. Conners, E. Markovitz, P. Howard, and G. Roth, "*Instantaneous supersonic velocity profiles in an underexpanded sonic air jet by oxygen flow tagging*," Physics of Fluids A, 1(2), pp. 389-393, February, 1989.

[200] R. B. Miles, J. Grinstead, R. H. Kohl, and G. Diskin, "*The RELIEF flow tagging technique and its application in engine testing facilities and for helium-air mixing studies*," Measurement Science and Technology, 11(9), pp. 1272-1281, September, 2000.

[201] L. R. Boedeker, "*Velocity measurement by H_2O photolysis and laser-induced fluorescence of OH*," Optics Letters, 14 (10), pp. 473-475, May 15, 1989.

[202] J. A. Wehrmeyer, L. A. Ribarov, D. A. Oguss, F. Batliwala, R. W. Pitz, and P. A. DeBarber, "*Flow tagging velocimetry for low and high temperature flowfields*," *37th AIAA Aerospace Sciences Meeting*, Reno, NV, 1999.

[203] J. A. Wehrmeyer, L. A. Ribarov, D. A. Oguss, R. W. and Pitz, "*Flame flow tagging velocimetry with 193-nm H_2O photodissociation*," Applied Optics, 38 (33), pp. 6912-6917, November, 20, 1999.

[204] L. A. Ribarov, J. A. Wehrmeyer, S. Hu, and R. W. Pitz, "*Multiline hydroxyl tagging velocimetry measurements in reacting and nonreacting experimental flows*," Experiments in Fluids, 37, pp. 65-74, 2004.

[205] L. A. Ribarov, S. Hu, J. A. Wehrmeyer, R. W. and Pitz, "*Hydroxyl tagging velocimetry method optimization: signal intensity and spectroscopy*," Applied Optics, 44 (31), pp. 6616-6626, November, 1, 2005.

[206] R. W. Pitz, M. D. Lahr, Z. W. Douglas, J. A. Wehrmeyer, S. Hu, C. D. Carter, K-Y. Hsu, C. Lum, and M. M. Koochesfahani, "*Hydroxyl tagging velocimetry in a supersonic flow over a cavity*," Applied Optics, 44(31), pp. 6692-6700, November 1, 2005.

[207] M. D. Lahr, R. W. Pitz, Z. W. Douglas, and C. D. Carter, "*Hydroxyl-Tagging-Velocimetry Measurements of a Supersonic Flow over a Cavity*," Journal of Propulsion and Power, 26 (4), pp. 790-797, July – August 2010.

[208] A. M. ElBaz, and R. W. Pitz, "*N_2O molecular tagging velocimetry*," Applied Physics B, 106, pp. 961-969, 2012.

[209] R. W. Pitz, T. M. Brown, S. P. Nandula, P. A. Skaggs, P. A. DeBarber, M. S. Brown, and J. Segall, "*Unseeded velocity measurement by ozone tagging velocimetry*," Optics Letters, 21 (10), pp. 755-757, 1996.

[210] L. A. Ribarov, J. A. Wehrmeyer, F. Batliwala, R. W. Pitz, and P. A. DeBarber, "*Ozone Tagging Velocimetry Using Narrowband Excimer Lasers*," AIAA Journal, 37(6), June 1999.

[211] N. J. Dam, R. J. H. Klein-Douwel, N. M. Sijtsema, and J. J. ter Meulen, "*Nitric oxide flow tagging in unseeded air*," Optics Letters, 26 (1), pp. 36-38, January 1, 2001.

[212] N. M. Sijtsema, N. J. Dam, R. J. H. Klein-Douwel, and J. J. ter Meulen, "*Air Photolysis and Recombination Tracking: A New Molecular Tagging Velocimetry Scheme*," AIAA Journal, 40 (6), pp. 1061-1064, June 2002.

[213] W. P. N. Van der Lann, R. A. L. Tolboom, N. J. Dam, and J. J. ter Meulen, "*Molecular tagging velocimetry in the wake of an object in supersonic flow*," Experiments in Fluids, 34, pp. 531-534, 2003.

[214] J. Bominaar, M. Pashtrapanska, T. Elenbaas, N. Dam, H. ter Meulen, W. van de Water, "*Writing in turbulent air*," Physical Review E, 77, 2008.

[215] C. Orlemann, C. Schulz, and J. Wolfrum, "*NO-flow tagging by photodissociation of NO_2. A new approach for measuring small-scale flow structures*," Chem. Phys. Lett., 307, pp. 15-20, 1999.

[216] N. Shinji, M. Kasahara, M. Tsue, and M. Kono, "*Velocity Measurements of Reactive and Non-reactive Flows by NO-LIF Method Using NO_2 Photodissociation*," Heat Transfer – Asian Research, 34 (1), pp. 40-52, 2005.

[217] A. G. Hsu, R. Srinivasan, R. D. W. Bowersox, and S. W. North, "*Molecular Tagging Using Vibrationally Excited Nitric Oxide in an Underexpanded Jet Flowfield*," AIAA Journal, 47 (11), pp. 2597-2604, November, 2009.

[218] N. Jiang, M. Nishihara, and W. R. Lempert, "*500 kHz NO_2 Molecular Tagging Velocimetry in a Mach 5 Wind Tunnel*," 27th AIAA Aerodynamic Measurement Technology and Ground Testing Conference, AIAA 2010-4348, Chicago, IL., Jun 28-July 1, 2010.

[219] R. Sánchez-González, R. Srinivasan, R. D. W. Bowersox, and S. W. North, "*Simultaneous velocity and temperature measurements in gaseous flow fields using the VENOM technique*," Optics Letters, 36(2), pp. 196-198, January 15, 2011.

[220] R. Sánchez-González, R. Srinivasan, R. D. W. Bowersox, and S. W. North, "*Simultaneous velocity and temperature measurements in gaseous flowfields using the vibrationally excited nitric oxide monitoring technique: a comprehensive study*," Applied Optics, 51(9), pp. 1216-1228, March 20, 2012.

[221] B. F. Bathel, P. M. Danehy, C. T. Johansen, S. B. Jones, and C. P. Goyne, "*Hypersonic Boundary Layer Measurements with Variable Blowing Rates Using Molecular Tagging Velocimetry*," AIAA Paper 2012-2886, 28th AIAA Aerodynamic Measurement Technology, Ground Testing, and Flight Testing Conference, New Orleans, LA., June 25-28, 2012.

[222] B. F. Bathel, C. T. Johansen, S. B. Jones, P. M. Danehy, and C. P. Goyne, "*Trip-induced Transition Measurements in a Hypersonic Boundary Layer Using Molecular Tagging Velocimetry*," 51st AIAA Aerospace Sciences Meeting, AIAA 2013-0042, Grapevine, TX., January 7-10, 2013.

[223] I. Boxx, M. Stöhr, C. Carter, and W. Meier, "*Sustained multi-kHz flamefront and 3-component velocity-field measurements for the study of turbulent flames*, Applied Physics B, 95(1), pp. 23-29, April, 2009.

[224] N. Jiang, M. Webster, W. R. Lempert, J. D. Miller, T. R. Meyer, C. B. Ivey, and P. M. Danehy, "*MHz-rate nitric oxide planar laser-induced fluorescence imaging in a Mach 10 hypersonic wind tunnel*," Applied Optics, 50(4), February 1, 2011.

[225] N. Jiang, J. Bruzzese, R. Patton, J. Sutton, R. Yentsch, D. V. Gaitonde, W. R. Lempert, K. D. Miller, T. R. Meyer, R. Parker, T. Wadham, M. Holden, and P. M. Danehy, "*NO PLIF imaging in the CUBRC 48-inch shock tunnel*," Experiments in Fluids, 53, pp. 1637-1646, 2012.

[226] B. Yip, R. L. Schmitt, and M. B. Long, "*Instantaneous three-dimensional concentration measurements in turbulent jets and flames*," Optics Letters, 13(2), pp. 96-98, February, 1988.

[227] P. M. Danehy, B. F. Bathel, J. A. Inman, D. W. Alderfer, and S. B. Jones, "*Stereoscopic Imaging in Hypersonic Boundary Layers using Planar Laser-Induced Fluorescence*," 26th AIAA Aerodynamic Measurement Technology and Ground Testing Conference, AIAA 2008-4267, Seattle, WA., June 23-26, 2008.

[228] C. S. Combs, N. T. Clemens, P. M. Danehy, B. F. Bathel, R. Parker, T. Wadhams, M. Holden, and B. Kirk, "*NO PLIF Visualizations of the Orion Capsule in LENS-I*," 51st AIAA Aerospace Sciences Meeting, AIAA 2013-0033, Grapevine, TX., January 7-10, 2013.

[229] R. B. Miles, W. R. Lempert and J. N. Forkey, "Laser Rayleigh Scattering," Meas. Sci. Technol. p. R33-R51, v.12, 2001. doi:10.1088/0957-0233/12/5/201

[230] Springer Handbook of Experimental Fluid Mechanics, Volume 1, edited by Cameron Tropea, Alexander L. Yarin, John F. Foss, ISBN-10: 3540251413 Springer, 1st Ed. 2007.

[231] G. C. Baldwin, "An Introduction Nonlinear Optics," Plenum Press, New York, 1969.

[232] A. Thorne, U. Litzèn, and S. Johansson, Spectrophysics: Principles and Applications, Berlin Heidelberg, 1999.

[233] P. Magre and R. W. Dibble, Finite chemical kinetic effects in a subsonic turbulent hydrogen flame, Combust. Flame 73, 195, 1988.

[234] V. Bergmann, W. Meier, D. Wolff, and W. Stricker, "Application of Spontaneous Raman and Rayleigh Scattering and 2D LIF for the characterization of a Turblent $CH_4/H_2/N_2$ Jet Diffusion Flame," appl. Phys. B, vol. 66, pp. 489-502, 1998.

[235] Q.V. Nguyen, R.W. Dibble, C.D. Carter, G.J. Fiechtner and R.S. Barlow, "Raman-LIF Measurement of Temperature, Major Species, OH and NO in a Methane-Air Bunsen Flame," Combust. Flame, vol. 105, pp. 499-510, 1996.

[236] R. G. Seasholtz and A. E. Buggele, "Improvement in Suppression of Pulsed Nd:YAG Laser Light With Iodine Absorption Cells for Filtered Rayleigh Scattering Measurements," NASA TM–113177.

[237] G. S. Elliott, M. Samimy, S. A. Arnette, "Details of a Molecular Filter-Based Velocimetry Technique," Paper AIAA-94-0490, 32nd Aerospace Sciences Meeting & Exhibit, Reno, NV, January 10-13, 1994.

[238] G. S. Elliott, M. Samimy, S. A. Arnette "A molecular filter based velocimetry technique for high speed flows," Experiments in Fluids, Volume 18, Issue 1-2, pp 107-118, December 1994.

[239] R.G. Seasholtz, A.E. Buggele, and M.F. Reeder, "Flow Measurements Based on Rayleigh Scattering and Fabry-Perot Interferometer," Optics and Lasers in Engineering, Vol. 27, No. 6, 1997, pp. 543-570.

[240] D. Bivolaru, M. V. Otugen, A. Tzes, and G. Papadopoulos, "Image Processing for Interferometric Mie and Rayleigh Scattering Velocity Measurements," AIAA J.Vol. 37, No. 6, June 1999.

[241] D. Bivolaru, P. M. Danehy, R. L. Gaffney, Jr. and A. D. Cutler, "Direct-View Multi-Point Two-Component Interferometric Rayleigh Scattering Velocimeter," 46th AIAA Aerospace Sciences Meeting and Exhibit, Reno, Nevada, AIAA Paper 2008-236, January 7-10, 2008.

[242] A. F. Mielke-Fagan, K. A. Elam, and M. M. Clem, "Multiple-Point Mass Flux Measurement System Using Rayleigh Scattering," AIAA-2009-528, 2009 47th AIAA Aerospace Sciences Meeting Including The New Horizons Forum and Aerospace Exposition, Orlando, Florida, January 5 - 8 2009.

[243] J. Panda, R. G. Seasholtz, and K. A. Elam, "Investigation of noise sources in high-speed jets via correlation measurements," Journal of Fluid Mechanics, Vol. 537, pp.349-385, 2005.

[244] A.F. Mielke, K.A. Elam, C.J. Sung, "Multiproperty Measurements at High Sampling Rates Using Rayleigh Scattering," AIAA Journal, Vol. 47, No. 4, pp. 850-862, 2009.

[245] D. Bivolaru, A. D. Cutler, and P. M. Danehy, "Spatially- and Temporally-resolved Multi-parameter Interferometric Rayleigh Scattering," Paper AIAA-2011-1293, 49th AIAA Aerospace Sciences Meeting including the New Horizons Forum and Aerospace Exposition, Orlando, Florida, January 4-7, 2011.

[246] A. F. Fagan, M. M. Clem, K. A. Elam, "Improvement in Rayleigh Scattering Measurement Accuracy," 50th AIAA Aerospace Sciences Meeting including the New Horizons Forum and Aerospace Exposition, AIAA 2012-1060 Nashville, TN., January 9-12, 2012.

[247] J. Kojima and D. G. Fischer. "Multiscalar Analyses of High-Pressure Swirl-Stabilized Combustion via Single-Shot Dual-SBG Raman Spectroscopy." Combustion Science and Technology 185, no. 12 (2013): 1735-1761.

[248] J. Kojima, D. Fischer, and Q.-V. Nguyen, "Subframe burst gating for Raman spectroscopy in combustion," Optics Letters, Vol. 35, No. 9, p. 1323-1325, May 1, 2010.

[249] J. Kojima and Q.-V. Nguyen, "Single-shot rotational Raman thermometry for turbulent flames using a low-resolution bandwidth technique," Meas. Sci. Technol. 19 (2008). doi:10.1088/0957-0233/19/1/015406

[250] S. M. Schoenung, R. E. Mitchell, Comparison of Raman and Thermocouple Temperature Measurements in Flames, Combust Flame 35 (1979) 207-211.

[251] A.D. Cutler, G. Magnotti, L. M. L. Cantu, E. C. A. Gallo, P.M. Danehy and R. Baurle, R. Rockwell, C. Goyne, and J. McDaniel "Measurement of Vibrational Nonequilibrium in a Supersonic Freestream using Dual-Pump CARS" AIAA-2012-3199, 28th Aerodynamic Measurement Technology, Ground Testing, and Flight Testing Conference, New Orleans, Louisiana, June 25-28, 2012.

[252] J. A. Wehrmeyer, S. Yeralan, and K. S. Tecu, "Linewise Raman-Stokes/anti-Stokes temperature measurements in flames using an unintensified charge-coupled device," Appl. Phys. B. 62, p. 21–27, 1996.

[253] F. Rabenstein, A. Leipertz, Two-Dimensional Temperature Determination in the Exhaust Region of a Laminar Flat-Flame Burner with Linear Raman Scattering, Appl Opt 36 (1997) 6989-6996.

[254] J. Kojima, and Q.-V. Nguyen, "Strategy for Multiscalar Raman Diagnostics in High-Pressure Hydrogen Flames," In: New Developments in Combustion Research (Edited by W. J. Carey), ISBN: 1-59454-826-9, NOVA Science Publishers, New York, (2006), pp. 227-256.

[255] S. P. Sharma, S. M. Ruffin, W. D. Gillespie and S. A. Meyer, "Vibrational Relaxation Measurements in an Expanding Flow Using Spontaneous Raman Scattering," J. of Thermophys. and Heat Trans. Vol. 7, No. 4, Oct.-Dec. 1993.

[256] T. M. Dyer, "Rayleigh scattering measurements of time-resolved concentration in a turbulent propane jet,"AIAA Journal, vol. 17, Aug. 1979, p. 912-914.

[257] R. W. Boyd, Nonlinear Optics, 3rd Ed., Academic Press, 2008.

[258] R. P. Lucht, "Three-laser coherent anti-Stokes Raman scattering measurements of two species," *Optics Letters*, Vol. 12, No. 2, Feb. 1987, pp. 78-80.

[259] S. O'Byrne, P. M. Danehy, S. A. Tedder, A. D. Cutler, "Dual-Pump Coherent Anti-Stokes Raman Scattering Measurements in a Supersonic Combustor," *AIAA Journal*, Vol. 45, No. 4, p. 922-933, April 2007.

[260] R. E. Palmer, The CARSFT Computer Code for Calculating Coherent Anti-Stokes Raman Spectra: User and Programmer Information, Sandia report SAND89-8206, Feb. 1989.

[261] A. D. Cutler, G. Magnotti, "CARS Spectral Fitting with Multiple Resonant Species Using Sparse Libraries," *J. Raman Spectroscopy*, Vol. 42, Issue 11, 2011, pp. 1949-1957.

[262] K. M. Bultitude, P.M. Danehy, E. Fraval, J.S. Fox, A.F.P. Houwing "Broadband coherent anti-Stokes Raman spectroscopy (BB-CARS) in flames and hypersonic flows," 2nd Australian Conference on Laser Diagnostics in Fluid Mechanics and Combustion, Monash University, Melbourne Australia, 1999.

[263] W. D. Kulatilaka, N. Chai, S. V. Naik, N. M. Laurendeau, R. P. Lucht, J. P. Kuehner, S. Roy, J. R. Gord, "Measurement of nitric oxide concentrations in flames by using electronic-resonance-enhanced coherent anti-Stokes Raman scattering," *Optics Letters*, Vol. 31, Issue 22, pp. 3357-3359, http://dx.doi.org/10.1364/OL.31.003357, 2006.

[264] S. Roy, J. R. Gord, A. K. Patnaik, "Recent advances in coherent anti-Stokes Raman scattering spectroscopy: Fundamental developments and applications in reacting flows," *Progress in Energy and Combustion Science*, Vol. 36, Issue 2, pp. 280-306, ISSN 0360-1285, 10.1016/j.pecs.2009.11.001, April 2010.

[265] R. P. Lucht, P. J. Kinnius, S. Roy, J. R. Gord, "Theory of femtosecond coherent anti-Stokes Raman scattering spectroscopy of gas-phase transitions," *J. Chem. Phys*. 127, 044316, http://dx.doi.org/10.1063/1.2751184, 2007.

[266] R. P. Lucht, S. Roy, T. R. Meyer, J. R. Gord, "Femtosecond coherent anti-Stokes Raman scattering measurement of gas temperatures from frequency-spread dephasing of the Raman coherence," *Appl. Phys. Lett*. 89, 251112, http://dx.doi.org/10.1063/1.2410237, 2006.

[267] T. R. Meyer, S. Roy, J. R. Gord, "Improving Signal-to-Interference Ratio in Rich Hydrocarbon–Air Flames Using Picosecond Coherent Anti-Stokes Raman Scattering," *Applied Spectroscopy*, Vol. 61, Issue 11, pp. 1135-1140, 2007.

[268] P. S. Hsu, A. K. Patnaik, J. R. Gord, T. R. Meyer, W. D. Kulatilaka, S. Roy, "Investigation of optical fibers for coherent anti-Stokes Raman scattering (CARS) spectroscopy in reacting flows," Experiments in Fluids, Volume 49, Issue 4, pp 969-984, October 2010.

[269] M. A. Woodmansee, J. C. Dutton, R. P. Lucht, "Experimental Measurements of Pressure, Temperature, and Density Measurements in an Underexpanded Sonic Jet Flowfield," Paper No. AIAA

99-3600, presented at the 30th AIAA Fluid Dynamics Conference, Norfolk, VA., June 28-July 1, 1999.

[270] J. Zheng, J. B. J. B. Snow, D. V. Murphy, A. Leipertz, R. K. Chang, R. L. Farrow, "Experimental comparison of broadband rotational coherent anti-Stokes Raman scattering (CARS) and broadband vibrational CARS in a flame," *Optics Letters*, Vol. 9, No. 8, pp. 341-343, August 1984.

[271] A. Bohlin, B. D. Patterson, and C. J. Kliewer. "Simplified two-beam rotational CARS signal generation demonstrated in 1D." The Journal of chemical physics 138 (2013): 081102.

[272] A. Bohlin, and C. J. Kliewer. "Two-dimensional gas-phase coherent anti-Stokes Raman spectroscopy (2D-CARS): Simultaneous planar imaging and multiplex spectroscopy in a single laser shot." The Journal of Chemical Physics 138 (2013): 221101.

[273] A. D. Cutler, G. Magnotti, L. M. L. Cantu, E. C. A. Gallo, P. M. Danehy, R. D. Rockwell, C. P. Goyne, J. C. McDaniel, "Dual-Pump CARS Measurements in the University of Virginia's Dual-Mode Scramjet: Configuration "C"," AIAA-2013-0335, 51st Aerospace Sciences Meeting, Grapevine, TX, 7-10 Jan, 2013.

[274] G. Magnotti, A.D. Cutler and P.M. Danehy, "Development of a Dual-Pump CARS System for Measurements in a Supersonic Combusting Free Jet", Paper AIAA-2012-1193, presented at the 50th AIAA Aerospace Sciences Meeting, Nashville TN., January 9-12, 2012.

[275] A.D. Cutler, G. Magnotti, L.M.L. Cantu, E.C.A. Gallo, P.M. Danehy, R. Baurle, R.D., Rockwell, C.P. Goyne, J.C. McDaniel, "Measurement of Vibrational Nonequilibrium in a Supersonic Freestream using Dual-Pump CARS," AIAA Paper 2012-3199, 28th AIAA Aerodynamic Measurement Technology, Ground Testing, and Flight Testing Conference, New Orleans, 25-28 June 2012.

[276] Vincenti, W.G., Kruger, C.H., *Introduction to Gas Dynamics*, Robert Krieger Pub. Co., New York, 1977.

[277] Center, R.E., Newton, J.F., "Vibrational Relaxation of N_2 by H_2O," *J. Chem Phys.*, Vol. 68, No. 8, April 1978.

[278] A. Montello, Z. Yin, D. Burnette, I.V. Adamovich, and W.R Lempert, "Picosecond CARS measurements of nitrogen vibrational loading and rotational/translational temperature in nonequilibrium discharges." Journal of Physics D: Applied Physics 46, no. 46 (2013): 464002. doi:10.1088/0022-3727/46/46/464002

[279] Hornung, H. G. "Nonequilibrium dissociating nitrogen flow over spheres and circular cylinders." Journal of Fluid Mechanics 53, no. 01 (1972): 149-176

[280] T. J. McIntyre, M. J. Wegener, A. I. Bishop, and H. Rubinsztein-Dunlop. "Simultaneous two-wavelength holographic interferometry in a superorbital expansion tube facility." Applied optics 36, no. 31 (1997): 8128-8134.

[281] G. E. A. Meier, "Hintergrund schlierenmessverfahren." Deutsche Patentanmeldung DE 199, no. 42 (1999): 856.

[282] H. Richard, and M. Raffel. "Principle and applications of the background oriented schlieren (BOS) method." Measurement Science and Technology 12, no. 9, p. 1576-1585, 2001.

[283] M. J. Hargather, and G. S. Settles. "Natural-background-oriented schlieren imaging." Experiments in fluids 48, no. 1, 59-68, 2010.

[284] T. Mizukaki, H. Tsukada, K. Wakabayashi, T. Matsumura, and Y. Nakayama, "Quantitative visualization of open-air explosions by using background-oriented schlieren with natural background," in: K. Kontis (ed) 28th International Symposium on Shock Waves 2:465–470, 2012.

[285] E. Goldhahn, and J. Seume. "The background oriented schlieren technique: sensitivity, accuracy, resolution and application to a three-dimensional density field." Experiments in Fluids 43, no. 2-3, p. 241-249, 2007.

[286] M. J Hargather and G. S. Settles. "A comparison of three quantitative schlieren techniques." Optics and Lasers in Engineering 50, no. 1 p. 8-17, 2012.

[287] L. Venkatakrishnan, and G. E. A. Meier. "Density measurements using the background oriented schlieren technique." Experiments in Fluids 37, no. 2, p. 237-247, 2004.

[288] Mohamed, A. K., J. Bonnet, S. Larigaldie, T. Pot, J. Soutadé, and B. Diop. "Electron beam fluorescence in hypersonic facilities." Aerospace Lab, the ONERA Journal 1 (2009).

[289] Smith, Jerome A., and James F. Driscoll. "The electron-beam fluorescence technique for measurements in hypersonic turbulent flows." Journal of Fluid Mechanics 72 (1975): 695-719.

[290] Cattolica, R. J., R. L. Schmitt, and R. E. Palmer. "Feasibility of non-intrusive optical diagnostic measurements in hypersonic boundary layers for flight experiments." In AIAA, Aerospace Sciences Meeting, vol. 1. 1990.

[291] P. M. Danehy, E. J. Friedman-Hill, R. P. Lucht and R. L. Farrow, "The effects of collisional quenching on degenerate four-wave mixing", App. Phys. B, Vol. B57, pp. 243-248, 1993.

[292] G. M. Lloyd, I.G. Hughes, R. Bratfalean, P. Ewart, "Broadband degenerate four-wave mixing of OH for flame thermometry," Appl Phys B, 67, pp. 107–113, 1998.

[293] E. B. Cummings, "Laser-induced thermal acoustics: simple accurate gas measurements," Opt. Lett. 19, 1361–1363, 1994.

[294] R. C. Hart, R. J. Balla, and G. C. Herring "Simultaneous velocimetry and thermometry of air by use of nonresonant heterodyned laser-induced thermal acoustics," Applied Optics, Vol. 40, Issue 6, pp. 965-968, 2001.

[295] R. C. Hart, G. C. Herring, and R. J. Balla, "Pressure Measurement in Supersonic Air Flow by Differential Absorptive Laser-Induced Thermal Acoustics," Optics Letters, Vol. 32, No. 12, pp. 1689–1691, 2007.

[296] R. C. Hart, G. C. Herring, and R. J. Balla, "Common-Path Heterodyne Laser-Induced Thermal Acoustics for Seedless Laser Velocimetry," Optics Letters, Vol. 27, No. 9, pp. 710–712, 2002.